Design and Testing of the Control Electronics for the Vaporizing Liquid Micro-resistojet

Jordy van der Horst

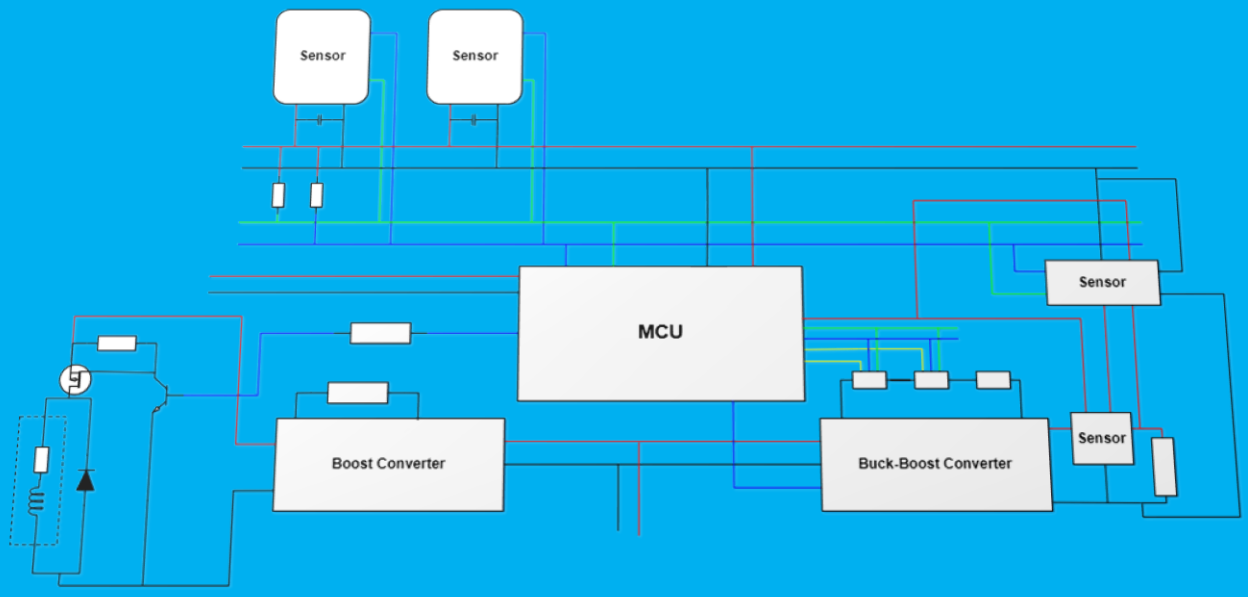

TU Delft

Design and Testing of the Control Electronics for the Vaporizing Liquid Micro-resistojet

by

J. van der Horst

in partial fulfilment of the requirements for the degree of

Master of Science
in Space Engineering

at the Delft University of Technology,
to be defended publicly on Thursday March 2, 2022 at 09:00 AM.

Student number:	4317408	
Project duration:	June 3, 2021 – March 2, 2022	
Supervisors:	Asst. Prof. A. Cervone,	TU Delft
	M. Ş. Uludağ,	TU Delft

TU Delft

Preface

This thesis represents the ultimate effort to earn the Master of Science Degree at the Aerospace Engineering faculty in TU Delft. This project was an ideal opportunity to use my knowledge from my Bachelor Electrical Engineering into the development of a control system for the vaporizing liquid micro-resistojet. The thesis project challenged me to experience the difficulties of conducting research, especially during this strange period with many restrictions. I'm very proud of the final product and I'm looking forward to apply all the gained skills in my professional career.

I would like to thank my supervisor Asst. Prof. Angelo Cervone and M. Şevket Uludağ for their guidance and advice during the entire duration of this project. They were always available when I was in need of help and provided me with the right tools to ensure that this thesis became a success. Special thanks to Vidhya Pallichadath for helping me during her vacation with the right equipment for the experiments. Finally, I would like to thank my friends and family for their support during the demanding period of the thesis project.

J. van der Horst
Amsterdam, February 2022

Abstract

The general idea of interest of this Master thesis project is the increasing demand for micropropulsion systems for miniaturized spacecraft. The developments and deployment of these satellites increased rapidly in the last decade. CubeSats and more recently PocketQubes are an interesting opportunity for lower budget organizations or universities. The ability to control the motion of these satellites becomes more important and hence a propulsion system is required.

This thesis presents the first steps in the development process of a dedicated control system for the vaporizing liquid micro-resistojet (VLM) of the Delft University of Technology. The produced thrust of the micropropulsion system is regulated by two main control parameters: temperature and pressure. The report proposes a different control mechanism for each control parameter and three different operational envelopes. The first two operational envelopes are solely designed for the experimental phase of the project, to examine the behavior of the control system on the separate control parameters. The final operational envelope could be used to control the propulsive operation of the VLM concept. An analysis of the measurement delay is made, to decrease the sampling time of the control loop. Two controllers, namely proportional-integral-derivative (PID) for the temperature and sliding mode control (SMC) for the pressure have been proposed.

The designed hardware is based on the requirements of the operational envelopes and control strategies. The control system can be divided into three main parts: microcontroller, temperature controller and pressure controller. The Arduino Uno is selected to be used during this phase of the development process. The temperature controller is combination of an adjustable power supply and a measurement setup. The adjustable power supply is a buck-boost converter that is controlled with two digital potentiometers connected to its feedback pin. The digital potentiometer combination has 2806 different output steps, resulting in an output resolution of 0.89 mV. The chamber temperature is determined with resistance measurements of the heater chip using voltage and current sensors. The current measurement results are unfortunately not sufficient for accurate temperature measurement, the sensor should be replaced in future projects. The chamber pressure is regulated by a ON/OFF valve at the inlet. The controller hardware is based on the requirements of the selected solenoid valve. It contains a boost converter and switching circuit to create the desired spike voltage at the solenoid valve. The energy requirements of the solenoid valve exceed the energy level of the propulsion subsystem.

The designed control system did not meet all the expectations. The temperature measurement system needs to be improved and an additional storage devices should be added to fulfil the requirements of the propulsion system. The biggest challenge that followed from this thesis project is the complex trade-off between sampling time, measurement accuracy, system dynamics and power usage. An optimal balance between these parameters is essential to make it suitable for missions in miniaturized spacecraft like the Delfi-PQ.

Contents

List of Figures

List of Tables

Symbols & Abbreviations

List of Symbols

α	Resistance temperature coefficient
Γ	Vandenkerckhove
γ	Specific heat ratio [J/(kg*K)]
$\eta_{conversion}$	Conversion efficiency buck-boost converter [%]
η_{DCDC}	Conversion efficiency boost converter [%]
μ	Dynamic viscosity [Pa s]
ω	Stefan-Boltzmann constant [W/(M^2K^4)]
ω_{SMC}	Sliding surface of SMC control [-]
A_{av}	Effective area for conduction [m^2]
A_e	Nozzle exit area [m^2]
A_out	Exit area solenoid valve [m^2]
A_t	Nozzle throat area [m^2]
A_{st}	Effective surface area [m^2]
c	Viscous coefficient
c_{pG}	Constant pressure specific heat Gass [J/K]
c_{pL}	Constant pressure specific heat Liquid [J/K]
d_b	Thickness [m]
$E_{components}$	Energy usage electronic components [Wh]
E_{peak}	Available energy during one sample [Wh]
$E_{quiescent}$	Energy losses due to quiescent current [Wh]
E_{spike}	Spike energy [Wh]
E_{temp}	Maximum supplied energy to buck-boost converter [Wh]
e	Error signal controller [-]
$F_{f,pl}$	Fluid force on plunger [N]
F_{mag}	Magnetic force [N]
F_T	Thrust [N]
g_0	Gravitational acceleration [m/s^2]
H_c	Average convective heat transfer [W/(m^2K)]
I_{sp}	Specific Impulse [s]
K_d	Derivative coefficient PID control [-]
K_i	Integral coefficient PID control [-]
Kn	Knudsen number
K_p	Proportional coefficient PID control [-]
K_{Si}	Thermal conductivity of Silicon [W/(M*K)]

k	Elastic constant of a spring [N/m]
L	Inductance [H]
L_h	Latent heat of vaporization [J/mol]
L_p	Length of the section [m]
$\dot{m}$	Mass flow rate [g/s]
M_W	Molecular Mass [u]
P	Power [W]
$P_{components}$	Power usage electronic components [W]
$P_{electronics}$	Electronics power usage [W]
P_{heater}	Available heater chip power [W]
$P_{in,boost}$	Input power boost converter [W]
P_{peak}	Peak Power [W]
$P_{quiescent}$	Power losses due to quiescent current [W]
P_{spike}	Spike power [W]
P_{temp}	Maximum supplied power to buck-boost converter [W]
$P_{solenoidvalve}$	Solenoid valve power usage [W]
P_{spike}	Spike Power [W]
p	Momentum [N·s]
p_1	Pressure of 1 atm [Pa]
p_c	Chamber pressure [Pa]
p_e	Nozzle exit pressure [Pa]
p_{ref}	Reference pressure [Pa]
p_t	Storage tank pressure [Pa]
q_{cond}	Conductive heat losses [W]
q_{conv}	Convective heat losses [W]
q_{loss}	Total heat losses [W]
q_{rad}	Radiative heat losses [W]
R	Gas constant [J/(K*g)]
R	Resistance [Ω]
R_0	Resistance at reference temperature [Ω]
R_A	Universal gas constant [J/(K*mol)]
R_{AB}	Total resistance of digital potentiometer [Ω]
R_c	Equivalent resistance solenoid valve [Ω]
R_{valve}	Valve resistance [Ω
R_W	Wiper resistance [Ω]
R_{WB}	Resistive output digital potentiometer [Ω]
T	Temperature [K]
T_0	Reference temperature [K]
T_1	Boiling temperature at pressure p_1 [K]
T_b	Boiling temperature [K]

T_c	Chamber Temperature [K]
T_i	Initial temperature [K]
T_{ref}	Reference temperature [K]
T_{sb}	Bottom substrate temperature [K]
T_{smooth}	Exponential filter temperature [K]
T_{st}	Effective surface temperature [K]
T_{vap}	Vaporization Temperature [K]
T_w	Wall temperature [K]
t	Time [s]
t_{min}	Minimum spike time [s]
t_s	Sensor sampling time [s]
u	Control signal SMC control [-]
V	Voltage [V]
V_e	Exit velocity [m/s]
V_FB	Feedback voltage [V]
V_h	Heater chip voltage [V]
V_{out}	Output voltage [V]
V_{spike}	Spike voltage [V]
V_v	Solenoid valve voltage [V]
w	Smoothing factor exponential filter [-]

List of Abbreviations

ADC	Analog-to-Digital Converter
CFD	Computational Fluid Dynamics
COTS	Commercial off-the-shelf
CV	Control Variable
DC	Direct Current
DR	Data Rate
DSMC	Direct Simulation Monte Carlo
DVT	Delta-V Thruster
EPS	Electrical Power Subsystem
HTC	Heat Transfer Coefficient
IDE	Integrated Development Environment
IRT	Ideal Rocket Theory
I^2C	Integrated Circuit
LPM	Low Pressure Micro-resistojet
MCU	Microcontroller Unit
MEMS	Microelectromechanical Systems
OBC	On-Board Computer
OSR	Oversampling Ratio

PID	Proportional-Integral-Derivative
PV	Process Variable
PWM	Pulse Width Modulation
RCT	Reaction Control System
RTD	Resistance Temperature Detectors
SMC	Sliding Mode Control
SNR	Signal-to-Noise Ratio
SP	Set Point
SPI	Serial Peripheral Interface
SPS	Samples Per Second
TU	Technical University
UART	Universal Asynchronous Receiver-Transmitter
VFS	Void Fraction Sensor
VLEO	Very Low Earth Orbit
VLM	Vaporizing Liquid Micro-resistojet

1

Introduction

The general idea of interest in this Master thesis project is the increasing demand for micropropulsion systems for miniaturized spacecraft. The developments and deployment of these satellites increased rapidly in the last decade. CubeSats and more recently PocketQubes are an interesting opportunity for lower budget organizations or universities. Their modular design and small dimensions reduce their development and launch costs. Recent technology developments created a completely new range of applications for CubeSats and PocketQubes. Applications in which the ability to control the motion of a satellite is essential and hence a propulsion system is required.

The launch costs of this class of spacecraft are reduced significantly due to 'Piggy-Back Launching' [16]. Small satellites are launched as a secondary payload and a single rocket is able to put multiple satellites into orbit. There are however a few limitations bounded to piggy-back launching, imposed for the safety of the primary payload. These limitations depend on the launch system and the primary payload. For CubeSat launches in past it was for example not not allowed to store propellant at a pressure above 1.2 bar, use explosive materials and the maximum stored energy in a small satellite was 100 Wh [16].

These restrictions limit the available propulsion possibilities, which are reduced even further due to limited amount of available power. Micro-resistojets are one of the few options able to operate within these limitations. The concept is based on the expansion of a gaseous propellant into space. The propellant is accelerated by a resistive heating element. It could therefore be non-explosive, non-hazardous and does not have to contain much chemical energy.

The vaporizing liquid micro-resistojet (VLM) stores its propellant in the fluid state, vaporizes the liquid in the chamber and accelerates the gaseous molecules in a convergent-divergent nozzle. The VLM concept still faces a number of challenges and is not widely tested in-orbit. The current development level of the VLM system developed by the Aerospace faculty of the Delft University of technology will be examined in this chapter and compared with other VLM propulsion systems. The focus of this examination will be on the ability to control the propulsive performance of the VLM concept. It will asses relevant literature of applied control theory to comparable micropropulsion systems and summarizes the basic component level requirements of a control system for the subsystems of PocketQubes. The setup for the research proposal together with the thesis outline will be given in sections 1.2 and 1.3, respectively.

1.1. Literature Study

This section presents an excerpt of an extensive literature study conducted to prepare for this thesis project. It will go through the various important aspects relevant to the design of a control system for the VLM concept. The section starts with a short assessment of the dedicated satellite, the PockeQube, and the selection process for the ideal propellant. After that, it will continue with the comparison of different thruster designs and control strategies from different organizations. The final part will shortly explain the requirements of the electronic components for the design of the VLM control system.

1.1.1. PocketQube

The development of the first PocketQube started in 2009 [13]. It is derived from another small, modular spacecraft: The CubeSat. Both concepts reduced the threshold for universities and smaller organizations to become active in space. The size of the PocketQube limits the possible applications, because it is simply not possible to miniaturize each subsystem. Therefore it is currently mostly used for training and/or educational applications and for technology demonstrations. Research is currently conducted to find other applications for PocketQubes, such as Earth observation, communications services and space exploration. The first PocketQube developed by the Delft University of Technology is the Delfi-PQ [50], its CAD model is shown in figure 1.1.

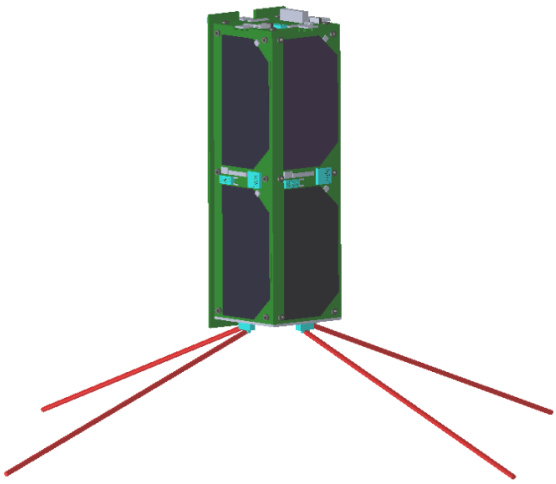

Figure 1.1: CAD model of the Delfi-PQ with deployed antenna [50]

The PocketQube is built from a single or multiple squared units with a size of 50x50x50 mm and a maximum weight of 250 g per unit [13]. They are launched as the secondary payload of larger satellites using a special deployment system. Often used deployment systems are the MRFOD and the AlbaPOD [13], both concepts use a base plate on the PocketQube which slides into a guided rails system. 'Piggy back' launching reduce the launch costs and make it affordable for smaller organizations, but there are a number of restrictions attached to this type of launching [16]. These restrictions should keep the primary, often very expensive payload safe. Due to these restrictions it is not possible to store propellant above 1.2 bar, use explosive materials and the maximum amount of stored chemical energy is limited to 100 Wh.

The launch restrictions are not the only limitations of a miniaturized spacecraft. The size limits the space for the electronic subsystem and the attached solar panels. The PocketQube is, depending on the size and arrangement of the solar panels, able to generate power in the range of a few hundred milliwatt up to 10 watt. This limits the communication possibilities and the available power for the propulsion subsystem. It is also mostly not possible to use active thermal control on PocketQubes due to limited available power. Temperature management is therefore a challenging objective, especially for the propulsion subsystem [50]. High temperatures could cause the propellant to boil in the storage tank, especially at the end of the mission when less propellant is left in the tank. Lower pressures will reduce the boiling temperature of water. Low temperatures could cause the propellants to freeze. Micro-resistojets usually operate below 200° Celsius, because the temperature should not exceed the component specifications (especially maximum valve temperatures) and the interface between the propulsion system and the spacecraft should stay between 5° Celsius and 85°

Celsius [50].

Another major advantage of micro-satellites is the possibility to create a cost effective constellation of PocketQubes. A constellation will make it possible to cover large surface for earth observation or measure the space weather at different locations simultaneously. Recent plans proposed for example a communication network with 7518 PocketQubes in Very Low Earth Orbit (VLEO, 340 km) [13]. This and other plans will increase the amount of satellites in an Earth orbit and therefore the chance on collisions rapidly. The lifetime of PocketQubes is hence an important aspect that should be taken into account during the design phase. The mission time of educational and technology demonstration satellites ranges from 3 months up to 2 years and the mission time for scientific and commercial ranges from 1 up to 7 years. Ideally, they should de-orbit after the end of their mission, but system failures make it sometimes difficult to control the spacecraft in the final stage of its lifetime. An ideal altitude for circular orbits is therefore between 300 and 400 km [13]. This orbital regime is currently not densely populated and the natural lifetime of satellites in this regime is appropriate to restrain space debris.

The observability by radar facilities as well as the communication possibilities for ground stations are also two important factors for the determination of the right orbital regime. "*The reflected radar signal is linearly proportional to the effective radar cross-section of the object and inversely proportional to the 4th power of the distance (which would be altitude in zenith direction)*" (Bouwmeester et al., [13]). A very small spacecraft at a large altitude is hence difficult to detect by radar facilities. These facilities determine not only the position of the PocketQube, but also calculate the risk on collisions with other spacecraft. The limitation in altitude and thereby the observability is essential for the completion of the mission, especially for large constellations of PocketQubes. The above mentioned communication constraints due to the small amount of available power also limit the preferable orbital altitude. The altitude for the Delfi-PQ is currently 529 km with an inclination of 97.5° [1].

The performance of a propulsion system for a PocketQube is not only limited to the launch restrictions and the size of the spacecraft. It is also limited by the performance of the attitude actuators. The amount of possible actuators is still relatively low compared to the possibilities for larger spacecraft. Mainly because of the short development time and the financial space of PocketQube users, but also due to technical limitations [13]. Magnetorquers are currently the only feasible option to compensate for the misalignment of the thrust-vector with the center of mass [13]. This results in a maximum allowable thrust for a 3p PocketQube of 3 mN [50].

1.1.2. Propellant Selection

The selection of the right propellant is a bit more restricted compared the propellant selection for a propulsion system for a larger spacecraft. The launch and design limitations for a micropropulsion system are already explained in section 1.1.1. The propellant shall not be pressurized, should be non-explosive and shall not be hazardous for other satellite subsystems or the operators. Ref. [25] investigated the characteristics 95 potential propellants. The best-scoring nine fluids have been selected for additional in-dept analysis for their performance parameters, thermal characteristics and safety concerns. Figure 1.2 shows the performance parameters specific impulse versus power and Delta-V versus power for these nine best-scoring fluids. Ammonia is superior in terms of specific impulse versus heating power and performs reasonably well in delta-V versus heating power for the VLM concept. Only water is able to achieve a higher delta-V per volume of fluid, but requires more heating power to achieve it. These results only consider the heating power used in the vaporization chamber, the power used to achieve the appropriate storage conditions is neglected. The nine selected propellants are then investigated on three safety characteristics: Flammability, health hazards and instability. Seven out of nine propellants have a high or extreme score on flammability, only ammonia and water have respectively a low and negligible flammability risk. The health hazard and instability score for each of the nine propellants is low or negligible except ammonia, which has a high level of health hazard. These results combined show that water is the most suitable propellant out of the 95 fluids with good performance parameters and perfect safety characteristics. Water is cheap, easily storable and has a relatively high density. The molecular mass of water (18 g/mol) represents a good trade-off between the required low molecular mass for a high specific impulse and high molecular mass for a small storage volume [16]. Using water as the main propellant has one major drawback: It has very high power consumption due to the high specific heat and high latent heat of vaporization [16].

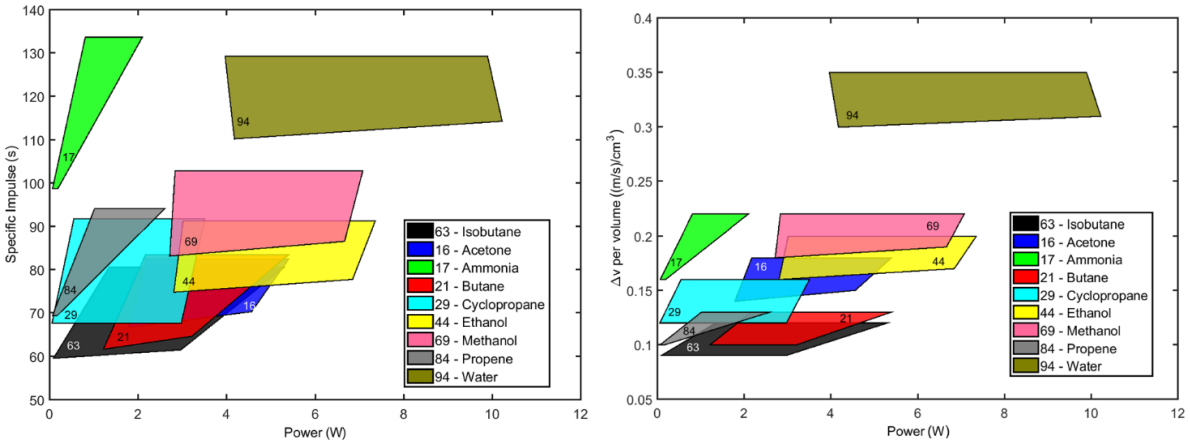

(a) Specific impulse versus power

(b) Delta-V versus Power

Figure 1.2: Performance parameters of best scoring nine fluids of Ref. [25]

1.1.3. Vaporizing Liquid Micro-resistojet

The first research into VLM's started since the mid-1960's [32]. This resulted in a short period of popularity for high power systems in the beginning of the eighties, in which commercial flights used resistojet's for attitude control and station keeping. The first steps in the miniaturization of the concept were made just before turn of the century and were initiated by the new microelectromechanical Systems (MEMS) fabrication techniques. The developments made since then only resulted in two orbit demonstrations, the first one was in 2003 (90-kg class UK-DMC satellite) and the second one in 2017 (1.5U CubeSat AeroCubes-OCSD7B&-7C) [47]. The orbit demonstration in 2003 was successful and showed a greater decrease in temperature and higher thrust compared to ground tests. The second one failed to produce any thrust due to a frozen nozzle. The results from both test will be analyzed in one of the next paragraph's of this section.

The concept of a VLM is based on the adiabatic expansion of a vaporized gas in a convergent-divergent nozzle [53]. The propellant, stored in the liquid state, flows via the inlet section, through the vaporization chamber to the nozzle. The liquid propellant is vaporized in the chamber by an internal or external heater element. The phase change from liquid to gas increases the specific volume of the propellant in the chamber rapidly [32]. The momentum of flow out of the nozzle results from the rise of total pressure in the chamber. The flow can be modeled in the continuum flow range, because of the low Knudsen number ($Kn <= 0.1$) [25].

Performance

The performance of VLM's is limited by the design and safety restrictions of micro-and pico-satellites. Research in various VLM designs is currently conducted to develop a thruster with a vacuum thrust level of 0.5-10mN with a specific impulse in the range of 50-200s for CubeSats [16]. The peak power of a 3U CubeSat propulsion system should be lower than 10W and its total wet mass should be lower than 450g [16]. The requirements for pico-satellites are even smaller, they require vacuum thrust levels in the range of 0.1-3mN with a specific impulse of 50-100s. This must be achieved by a propulsion system with a wet mass lower than 75g and a peak power consumption lower than 4W [50]. Table 1.1 shows that there are a number of designs able to operate within the demands of CubeSats and PocketQubes. The last design of table 1.1 is COTS from a Finnish company called Aurora Propulsion Technologies [10]. Thrust and specific impulse requirements are mostly within range, but the peak-power requirements are not always met. This is especially the case for maximum thrust operations, due to the large amount of required heat for vaporization.

Design

This section will explain the design choices made in literature. The first paragraph goes through the different liquid storage and feed systems. The design and operational processes of the vaporization chamber are

Ref.	P [W]	$\dot{m}$ [mg/s]	F_T [uN]	I_{sp} [s]	Propellant	Measurement
[36]	2.82-9.31 (VA)	0.83-5.30	186.05-970.98	N/A	Water	Indirect
[32]	7.70-7.94	3.06-5.99	997-2004	25.9-51.1	Water	Direct
[47] (DVT)	2.66-14.44	5.86-6.30	3710-4470	63.03-73.97	Water	Direct
[47] (RCT)	0.19-6.65	1.23-1.48	550-730	54.28-65.32	Water	Direct
[52] (5)	7.29	0.55	670	124.02	Water	Simulated
[10]	2.0-20.0	N/A	600-4000	100 (estimate)	Water	N/A

Table 1.1: Propulsion performance overview of different VLM systems

analyzed in the second paragraph. The final paragraph will explain the choices made for the convergent-divergent nozzles.

Liquid Feed & **Storage System** The liquid feed & storage system should be able to supply the thruster sufficient propellant for the entire operation. It should be able to control the pressure in the vaporization chamber and therefore the mass flow through the nozzle. Launch restrictions of micro-and picosatellites prohibit the system to store the propellant at high pressures. The maximum internal pressure in a CubeSat or PocketQube is equal to 10 bar [16, 49]. Water is, as mentioned before, often chosen as the ideal propellant for VLM propulsion systems, because it offers a good combination of mass and volumetric specific impulse and is safe to handle. The requirements of the Delfi-PQ PocketQube demand that the thermal interface between the propulsion system and the satellite stays between 5° Celsius and 85° Celsius [49] during all mission phases. The phase diagram of water shows that water will be in the liquid state considering the pressure and temperature requirements [71]. The system should also be able to operate using gaseous nitrogen. Nitrogen will always be in the gaseous state considering the pressure and temperature requirements [22].

The development of VLM systems is currently still in an early phase. Most systems are only opposed to a number of ground tests and the model is often not ready to be tested in space [32, 35, 36, 52]. These ground tests are conducted using a syringe pump which operates as the liquid propellant storage & feed system. It is used to control the flow rates of the propellant to vaporization chamber. It is preferred above a regular blow-down system, because it is able to keep the flow rate constant and makes it possible to examine the effect of varying flow rates on the performance. Available literature that describes the design of a designated feed & storage system for a VLM is therefore limited. The Delft University of Technology developed a blow-down system for an in-orbit demonstrator for pico-satellite applications [49]. It is a dual micropropulsion system able to demonstrate two different micro-resistojet concepts: VLM and LPM. The systems uses the capillarity properties of water in a small flexible tube to use the same storage system for both concepts. The propellant is pressurized by gaseous nitrogen. It is stored in a Teflon tube with a diameter of 1.57mm and a length of 300 mm. The system uses a normally closed solenoid valve (2-way, high-speed valve: INKX0511400A). The valve is electrically connected to the microcontroller by two pins and is actuated using a spike and hold circuit. The micro-valve system records the control voltage, inlet pressure and outlet pressure.

Vaporization Process The vaporization chamber is the crucial part of a VLM system as it has a very large influence on the performance. Liquid water is vaporized by a heating element and transported to the nozzle. The performance of the vaporization chamber depends on the flow and boiling process of the propellant. These properties are influenced by the chamber pressure, chamber temperature and by the size and shape of the chamber. This paragraph will analyze the vaporization chamber of TU Delft and compare it similar designs from other organizations.

The design of the TU Delft was planned to be integrated in an in-orbit demonstrator for the micropropulsion system of the Delfi-PQ [16, 49, 52]. Two different shaped vaporization chambers are designed and tested in combination with integrated molybdenum heaters. Molybdenum is a metal with a high melting point of 2693° Celsius. Its resistivity is linearly proportional to the temperature (<700° Celsius), which makes it suitable for precise temperature measurements. The heaters are tested in two configurations, one with 21 lines with a total resistance of 3.40 Ω and the other one with 30 lines with a total resistance of 2.38 Ω. The thrusters are small and made out of silicon (good thermal conductor), it is therefore estimated that the temperature of the complete thruster equal is to the temperature of the heaters. There are two designs for the vaporization

chamber: One with serpentine channels and one with diamond pillars. Both concepts are tested in large and small surface configurations and are shown in figure 1.3. The tests were conducted with a syringe pump at room temperature without proper thermal isolation. The syringe pump causes low frequency pressure fluctuations in the propellant flow, this could cause some instabilities in the two-phase flow. It could result in the ejection of liquid droplets out of the nozzle. This effect was only visible in the pressure measurements, no instability was spotted visibly in the behavior of the flow during operation. The concept with small diamond pillars seemed to be the most efficient due to its large surface.

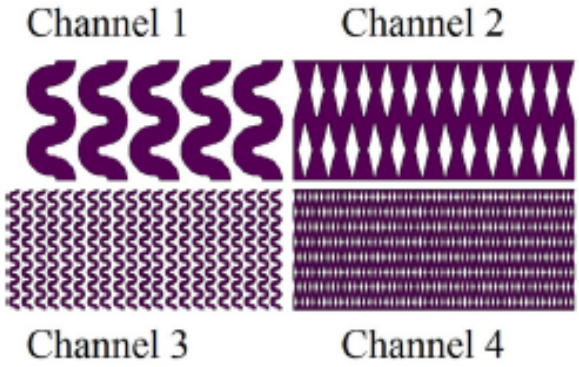

Figure 1.3: Schematic overview of the channels configurations of [52]

Other organizations also developed comparable vaporization chambers based on the same concept.

- The concept of figure 1.4a is developed by the University of Tokyo and is based on a pulsating operation of two phases, a thrust generating period and a draining period [6, 31, 47]. The liquid propellant is vaporized at room temperature under saturated vapor pressure. Water vapor then leaves the vaporization chamber and is heated in the labyrinth shaped path to the nozzle. It is designed to minimize the amount of liquid droplets that are expelled through the nozzle to prevent the nozzle from freezing.

- The concept of figure 1.4b based on a vaporization chamber with a straight flow path and internal molybdenum heaters [32]. It is developed by the Hong Kong University of Science and Technology and the Peking University. The developers chose to use a straight microchannel configuration in this concept, to decrease the pressure loss in the chamber. The heaters should be able to let the thruster operate in the film boiling regime, this regime prevents the liquid water propellant to reach the chamber walls using rapid vaporization with higher temperatures. This high excess temperature initiates the Leidenfrost effect, high vaporization rates produces sufficient pressure to bounce the droplets away from the chamber wall. Droplets attached to the chamber wall would hinder the flow and would therefore decrease the efficiency of the thruster.

- A schematic overview of the third concept is given in figure 1.4c [20]. This design is developed by the Italian National Research Council - Institute of Microelectronics and Microsystems. The vaporization chamber consists of two heater sections. An external platinum resistive heater is used to increase the propellant temperature in the microchannels. The secondary heating section performs a localized heating operation for flow instability control and is powered by low-power on-channel heaters.

- A schematic overview of the final concept is shown in figure 1.4d. The concept is developed by the College of Mechanical Engineering and Applied Electronics Technology of the Beijing University of Technology. It is based on planar induction heating the vaporization chamber [36]. An internal plate generates heat due to the eddy current induced by an external excitation coil. This concepts simplifies the fabrication of the chamber because of the wireless transportation of energy to the internal heating plate. A high frequency AC current is applied to the excitation coil to generate the eddy current. Figure 1.4d shows rectangular holes in the heating plate. These holes distribute the eddy current as it can not flow through the holes. This increases the current density in the sections between the holes. A higher current density results in a higher power density and therefore increase in temperature. The holes or surface cavities affect the dynamic behavior of the flow inside the chamber. Non-condensable

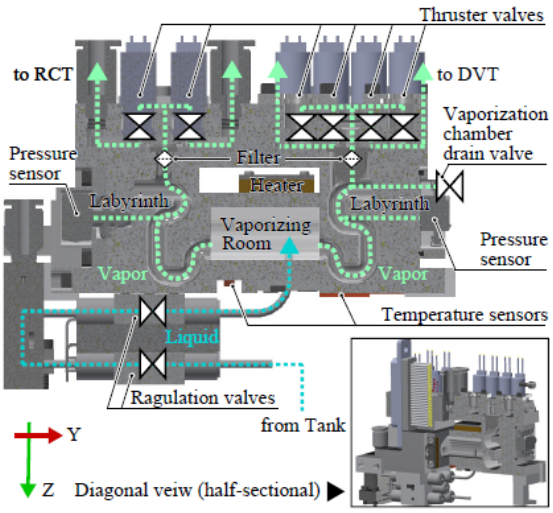

(a) Schematic half-sectional view of the thruster from [47]

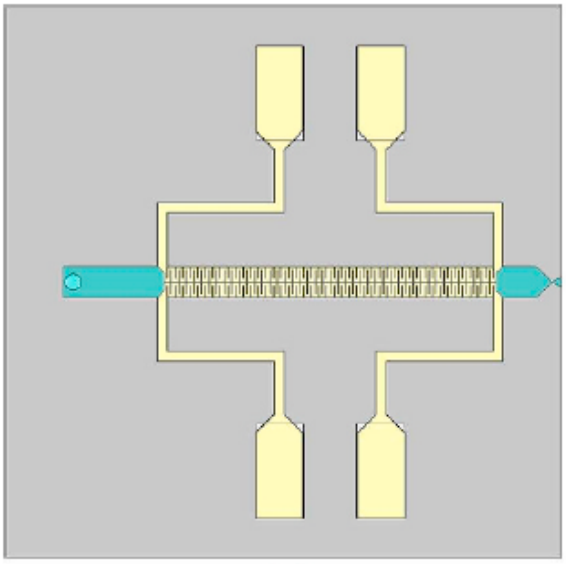

(b) Schematic overview of the MEMS VLM concept [32]

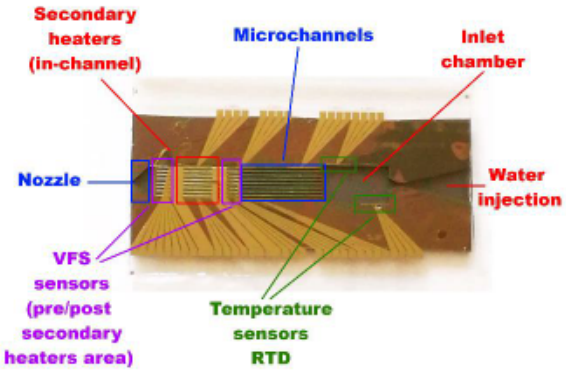

(c) Schematic overview of the MEMS microthruster with two heater sections [20]

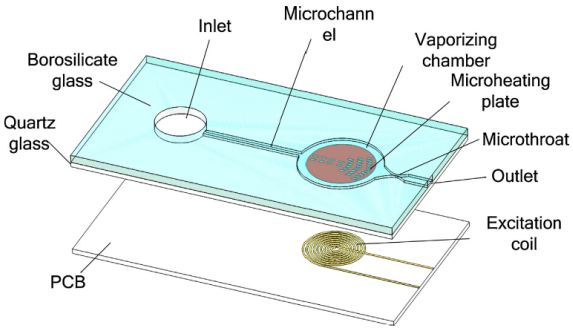

(d) Schematic overview of the VLM concept with planar induction heating [36]

Figure 1.4: The vaporization chamber design of different VLM concepts

gas could be trapped in the cavities and produce bubbles when heating, which could affect the flow in the chamber.

This paragraph explained the various design choices made in the different concepts. It became clear that a trade-off should be made between a large heating surface, in for example serpentine channels, and a low pressure drop in a straight flow path. The type of heating is also important for the efficiency. An internal heater is a bit more complex, but has a better heating efficiency due to direct contact with the propellant. The final concept showed that the complexity of an internal heater can be simplified using planar induction heating. Most concepts operate in temperature ranges around or above the boiling temperature of water, except for one. This model vaporizes the liquid propellant in the chamber at room temperature and increase the vapor temperature on its path to the nozzle of the thruster.

Nozzle Design The vaporization chamber is the core of the concept, it explains the working principle of a VLM system. It also has a large influence on the performance of the system, but its not the only part that affects the thruster performance. The convergent-divergent nozzle accelerates the water vapor into the environment. The size of the designed nozzles is adjusted to the size of the thruster and the produced thrust of approximately 0.1-10 mN. It is therefore not possible to accurately simulate the performance of a micronozzle using Ideal Rocket Theory (IRT) only, Computational Fluid Dynamic (CFD) simulations need to be used instead [16]. The difference between the effective throat area and the nominal throat are can be large,

this could result in a big difference between the ideal and actual performance of the nozzle. The boundary layers and surface roughness of these nozzles reduce the effective throat area significantly. This is expressed by the discharge coefficient of a nozzle. Previous studies showed that there is a significant drop in the discharge coefficient for Reynolds numbers smaller than 1000 [11].

Vapor flow can, unlike gas flow, exist out of two phases simultaneously, the analysis of the flow in a nozzle is therefore complicated. This simplifies when the saturation temperature is reached, the propellant flow will now behave like the flow behavior of a perfect gas [27]. An increasing mass flow rate causes the nozzle exit temperature to decrease. The vapor could condense to the nozzle walls and reduce the thrust when the exit temperature is smaller than the saturation temperature. This is called 'super cooling'. The condensation to the nozzle walls also depends on the residence time of the vapour in the nozzle. When the residence time is too short, it is not possible for the vapour to condense to the nozzle walls. If the temperature decreases even further and the residence time is sufficient, the vapor could form ice at the nozzle exit. The heating power should be increased to put the temperature back at the saturation level, only then it is possible to assume perfect gas behavior. The available heater power in a small satellite is limited, so the maximum allowed mass flow is also limited. Less available heater power has a negative influence on the performance of the thruster as the nozzle is more efficient at higher mass flow rates. This can be explained by the effect of the boundary layer on the efficiency, which is more significant at lower mass flow rates.

An increase in the area ratio of the thruster has a positive influence on the thrust force due to the increase in exit velocity [27]. This is the result of a smaller exit pressure and therefore larger pressure ratio, which follows from a larger nozzle exit area allowing the vapor to expand more. On the other side, increasing the area ratio also decrease the exit temperature and increase the residence time of the vapour in the nozzle, increasing the risk of vapour condensation to the nozzle walls. A balance between both conditions should be found to ensure proper operation. The increasing slope of the thrust force is smaller for lower mass flow rates, due to the boundary layer effect. The vapor expansion will not increase further when the area ratio is increased without increasing the propellant mass flow rates. This limits the area ratio for a certain mass flow rate. Increasing the area ratio is only efficient when the mass flow can be increased, which is only possible when the required heater power is available.

1.1.4. Control Strategy

An optimized control strategy is essential for an efficient operation with good performances. A control strategy could be based on the analytical model of the system. A proper analytical model of a VLM is necessary to estimate its performance with a good accuracy. Analysis of the behavior of the flow is difficult due to the strong link between the boiling process in the vaporization chamber and the flow in the micronozzle [18]. Research is conducted to analyze the different conditions separately, without properly considering the coupling between them. The performance of this micropropulsion system is affected by the boundary layer in the nozzle, flow boiling instabilities in the chamber and the expansion of the two-phase flow in the nozzle [18]. Two different flow regimes could occur in a VLM micronozzle: the transitional flow regime ($0.1 < Kn < 10$) and the slip flow regime ($0.01 < Kn < 0.1$) [18]. Both require a different approach for the analysis of the behavior of the flow. DSMC are required for the transitional flow regime and the Navier-Stokes equations should be used for the slip flow regime. Modeling the boiling process in the chamber opposes a number of challenges, such as for example bubble nucleation, transport and phase change phenomena thermal properties of the chamber and heater [18]. The CFD computations required for these challenges are complex and an accurate comprehensive model is not directly available.

Analytical Model

This paragraph will present a simple analytical model for the behavior and performance of a VLM and will asses its shortcomings. The analytical model is based on the Ideal Rocket Theory (IRT) for the continuous flow regime [25, 52]. It does not give a very reliable estimation of the real situation due to the amount of assumptions made in IRT, but it could be used to predict the effects of certain initial design choices on the performance of the concept. The analytical model starts with the Vandenkerckhove function given in equation 1.1, in which the specific heat ratio is given by γ.

$$\Gamma = \sqrt{\gamma(\frac{1+\gamma}{2})^{\frac{1+\gamma}{1-\gamma}}} \tag{1.1}$$

The Vandenkerckhove value could then be used together with the known area ratio of the nozzle (A_e/A_t) to determine the pressure ratio (p_e/p_c) by means of iteration using equation 1.2.

$$\frac{A_e}{A_t} = \frac{\Gamma}{\sqrt{\frac{2\gamma}{\gamma-1}\left(\frac{p_e}{p_c}\right)^{\frac{2}{\gamma}}\left(1-\left(\frac{p_e}{p_c}\right)^{\frac{\gamma-1}{\gamma}}\right)}} \tag{1.2}$$

The chamber temperature (T_c) and pressure (p_c) should be known to determine the mass flow rate through the nozzle with equation 1.3 and the exit velocity with equation 1.4.

$$\dot{m} = \frac{p_c A_t}{\sqrt{RT_c}}\Gamma \tag{1.3}$$

$$V_e = \sqrt{\frac{2\gamma}{\gamma-1}RT_c\left(1-\left(\frac{p_e}{p_c}\right)^{\frac{\gamma-1}{\gamma}}\right)} \tag{1.4}$$

The results from these equations could then be used to determine the thrust and specific impulse of the system with respectively equations 1.5 and 1.6.

$$F_T = \dot{m}V_e \tag{1.5}$$

$$I_{sp} = \frac{F_T}{\dot{m}g_0} \tag{1.6}$$

With g_0 equal to the gravitational acceleration. A simple equation to show the dependency between the chamber pressure and temperature is given in equation 1.7. It determines the required power to vaporize and heat-up the vapor to the chamber temperature for a given mass flow rate [49].

$$P = \dot{m}\cdot[c_{pL}(T_{vap}-T_0)+L_h+c_{pG}(T_c-T_{vap})] \tag{1.7}$$

Where the average constant specific heat of liquid and vapor are respectively given by c_{pL} and c_{pG}. The latent heat of vaporization is given by L_h. This equation only determines the amount of power required by the propellant, without considering any thermal losses to the environment and the effects of boiling phenomena on the performance. The vaporization temperature varies with the chamber pressure and could be calculated using the Clausius-Clapeyron relation [69], given in equation 1.8.

$$T_{vap} = \frac{T_1 L_h M_W}{T_1 R_A ln(\frac{p_1}{p_c}) + L_h M_W} \tag{1.8}$$

T_1 is equal to the boiling temperature at a pressure p_1 of 1 atm. Ref. [69] showed that a higher mass flow rate could be achieved by minimizing the difference between the chamber temperature and the vaporization temperature i.e. varying the chamber temperature for different chamber pressures. Equation 1.7 could then be simplified by assuming that the chamber temperature is equal to the vaporization temperature, resulting in equation 1.9.

$$P = \dot{m}\cdot[c_{pL}(T_{vap}-T_0)+L_h)] \tag{1.9}$$

Equation 1.3 could be combined with equation 1.9 into equation 1.10. This equation shows that the amount of power required by the propellant, for complete vaporization, only depends on one variable, the pressure in the chamber. Ref. [38] also explained that increasing the heater power will not directly result in a higher chamber temperature, the added energy will be first consumed by the boiling process. This lead to a higher evaporation rate, resulting in a higher vapor pressure and rising thrust. The chamber temperature and therefore the chamber pressure will increase after the liquid is fully vaporized.

$$P = \frac{p_c A_t}{\sqrt{RT_{vap}}}\Gamma\cdot[c_{pL}(T_{vap}-T_0)+L_h)] \tag{1.10}$$

The losses in the vaporization chamber are, unfortunately, not equal to zero. Ref. [23] compared the ideal power versus pressure curve, obtained with equation 1.10, with actual experimental results of three thruster models. Figure 1.5 shows the differences between the ideal and real power demands over a given pressure range.

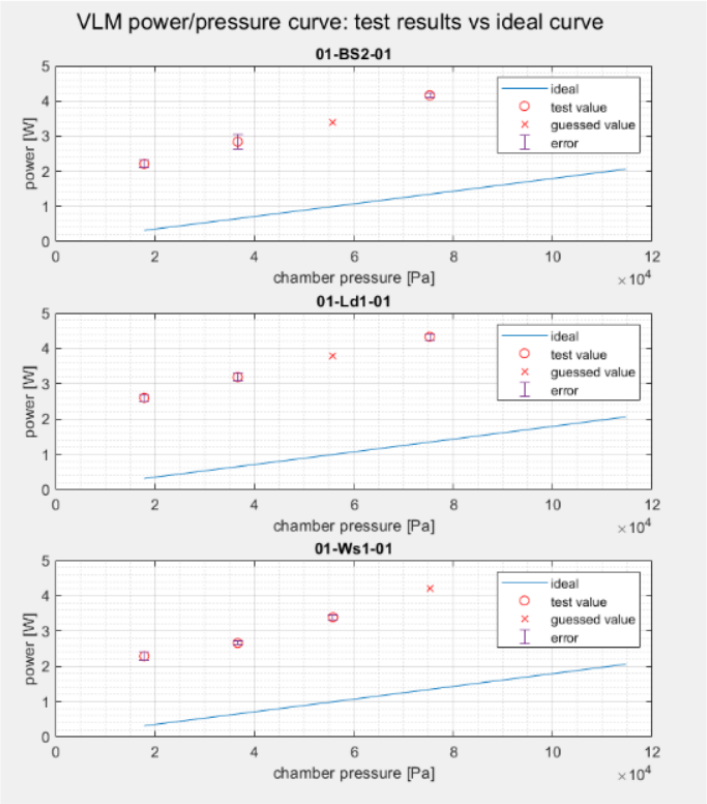

Figure 1.5: Ideal power versus pressure curve plotted against experimental results [23]

The real power versus pressure curve of all three of the tested models could be characterized by the linear equation 1.11, with a [W/Pa] and b [W]. These experimental results show that the maximum chamber pressure is approximately 0.7 bar for the peak power requirements of PocketQubes (4 W). Which is also without considering the power demands of the solenoid valve and additional control electronics. This will further decrease the available power for the vaporization process.

$$P = a \cdot p_c + b \tag{1.11}$$

Energy from the heater chip is lost by radiation, convection and conduction. Ref. [38] suggests that there are conductive heat losses through the insulated bottom side of the chamber and convective and radiative heat losses through the top side of the chamber. These losses are given in equation 1.12.

$$q_{loss} = q_{conv} + q_{rad} + q_{cond} = H_c A_{st}(T_{st} - T_i) + \sigma A_{st}(T_{st}^4 - T_0^4) + \frac{K_{Si} A_{Av}}{d_b}(T_c - T_{sb}) \tag{1.12}$$

With H_c equal to the average convective heat transfer, A_{st} equal to the effective surface area, σ equal to the Stefan-Boltzmann constant, A_{av} equal to the effective area for conduction, K_{Si} equal to the thermal conductivity of silicon and d equal to the thickness. These losses should added to the energy consumption in the chamber to determine the total required heater power.

The experimental results from Ref. [23] show the differences in power demands between the ideal and real situations. More or less the same is true for the IRT equations. The IRT model is based on a number of assumptions. These assumptions hold, in general, for regular sized thrusters. Nozzle and thrust efficiency explain the difference between the ideal and real performance of those systems. The assumptions do not

have significant effects on the accuracy of the IRT results. This is, unfortunately, different for micropropulsion systems, mainly due to the size of the system. In IRT they assume adiabatic flow in the nozzle, they neglect friction and assume uniform distribution [54]. There is no adiabatic flow in the nozzle, because the nozzle also transfers thermal energy to the propellant. Which is mainly due to the small size of the thruster. This also affects the surface friction and boundary layers, both are not negligible in micropropulsion systems. Which, in turn, rejects the assumption of a uniform distribution of the gas temperature, density, pressure and velocity. Two comparable approaches include the effect of IRT assumptions on the performance of micropropulsion systems.

Ref. [54] assumes that there are three different mass flow rates in the thruster. The first one is the liquid flow rate into the inlet section ($\dot{m}_1$), the second one is the vaporization rate ($\dot{m}_2$) and the third one is the mass flow rate of the nozzle ($\dot{m}_3$). The unbalance between these three rates is the first factor that governs the dynamics of the system. The other one is the applied power to the heaters, which affects the vaporization process. Ref. [18] proposed an analytical model which couples the boiling process with the behavior of the flow inside the micro-nozzle, using IRT and semi-empirical relations. The discharge coefficient is used to estimate the losses of the boundary layer to the exit velocity and mass flow rate. These losses are subtracted from the ideal performance determined by the IRT.

Ref. [54] and Ref. [18] have one major approach in common. Both of them use experimental results to derive the input parameters for their equations empirically. Ref. [54] used a digital microscope to assess the behavior of the two-phase flow in the chamber. Ref. [18] took a slightly different approach and used an extensive collection of literature to create the model empirically and used the design and results from Ref. [14] to verify their results. The similarities between both references can be found in the division between the boiling process in the vaporization chamber and the acceleration of the vapor in the convergent-divergent nozzle. Ref. [54] used the linear regression function of the volumetric behavior of the two-phase flow in the chamber to determine the vaporization rate, used the Antoine equation to calculate the temperature of the vapor and followed the IRT assumptions to determine the performance of the thruster. In addition, they provided a state-space model of the proportional solenoid valve to couple a certain input voltage to the mass flow rate to the inlet section. Simply using the IRT assumption is insufficient for the thrusters within these size ranges. Ref. [18] presented therefore the possibility to determine the discharge coefficient and the specific impulse efficiency, modeling the effects of the boundary layer in the nozzle. This increased the accuracy of the estimated performance. In addition, they presented a possibility to assess the two-phase flow in the chamber by determining the heat transfer coefficient before and after the establishment of the dry-out condition. This is done using the estimated value of the local Nusselt number, resulting in a faster evaporation process in the chamber. The performance estimations of the model approached the experimental thrust and specific impulse with errors smaller than 7.3%. This is an improvement compared to the 2D CFD computations, probably because of the 3D real flow effects. These effects are neglected in the 2D CFD computations. The vaporization chamber and nozzle models from Ref. [18] could be combined with the solenoid valve model from Ref. [54] to create a broader picture of the behavior of the complete system. The formulation of a accurate comprehensive model for a certain VLM system could be a project on its own and is out of the scope of this thesis project. This section presented therefore only the analytical model based on the IRT assumptions and evaluated its shortcomings using relevant models from literature.

Control Mechanisms

The performance of a VLM does not only depend solely on the geometry and propellant choice, but also on the ability to control the thrust and specific impulse with maximum efficiency. The model proposed in the previous section of this chapter could be used to calculate the performance given the adjustable input parameters. These input parameters are the heater chip power and chamber pressure. The simple equation to show the dependency between both parameters is already given in equation 1.10. The vaporization temperature depends on the pressure in the chamber, resulting in a relation between the chamber pressure and required heater chip power. The power-pressure relation only determines the amount of power required by the propellant, without considering any thermal losses to the environment and the effects of boiling phenomena on the performance. The boiling process of a two-phase flow is almost always unstable [15]. The produced thrust depends strongly on the pressure in the chamber. The pressure tends to fluctuate, resulting in a fluctuating thrust. The pressure fluctuation could be caused by explosive boiling, which occurs at the inlet and in the

channels periodically [15]. The explosive pushed a little bit of the fluid forward in the direction of the nozzle, but most of the incoming fluid is pushed back to the inlet. The liquid propellant in the channels accumulate together and form droplets due to the surface tension. The size of the channels is very small, so the droplets block the channels. The heater chip increases the temperature of the droplets and they slowly evaporate en become smaller until they are pushed out by the pressure of the vapor. The heat transfer rate decreases due to the deviation of the thermodynamic equilibrium, mainly caused by the small channel size and high flow speed. The boiling mode in micro-scale thrusters is not continuous, but it occurs instead at random time intervals.

The determination of the Heat Transfer Coefficient (HTC) in micro-scale systems is difficult due to the presence of nucleation boiling activity and active convective mechanisms [68]. The type of boiling is determined by the boiling state which is coupled to the pattern of the flow in the microchannel. Five flow patterns are distinguished for the two-phase flow in a VLM: bubble flow, slug flow, churn flow, annular flow and dry-out regions. The flow pattern is defined by the vapor quality, which is the ratio of vapor mass flow to the total mass flow. Bubble flow has the lowest vapor quality and dry-out regions are indicated by a high vapor quality. The HTC reaches its maximum close to the inlet in bubble or slug flow, at the start of boiling with the dominating nucleation boiling mechanism [57]. The convective boiling mechanism becomes the important heat transfer mechanism with a higher vapor quality and annular flow pattern. The HTC starts decreasing significantly when the first dry-out regions start to form, this occurs when the vapor quality approaches '1'. There is no thin film layer of liquid on the chamber wall in the dry-out regions, reducing the heat transfer coefficient in that area.

Higher thrust levels are achieved by increasing the chamber pressure and heater chip power. Both input parameters are limited by the given requirements of QubeSats and PocketQubes. The mass flow is limited by the maximum allowed internal pressure of 10 bar for both satellites and will also reduce during operation. The available peak power in QubeSats is limited to 10W [16] and in PocketQubes to 4W [49]. The actual power transferred to the propellant is, taking the heating efficiency into account, even smaller. The heating efficiency depends on the geometry of the chamber and heating mechanism and is therefore difficult to estimate, but will probably be in the range of 50-60% [21]. Reducing the transferred power in a VLM system in a PocketQube below 2W.

Higher chamber pressures increase the mass flow rates through the chamber and therefore increase the produced thrust. High mass flow rates also reduce the residence time in the chamber and hence decrease the heat transfer from the heater chip to the propellant. This increases the chance of expelling liquid droplets through the throat. Liquid droplets at the exit could possible freeze, blocking the nozzle, and consist of less thermal energy, reducing the produced thrust. An incomplete boiling process will also decrease the mass flow rate through the chamber, as the vapor pressure increases after vaporization of the liquid propellant. It is therefore important to couple the chamber pressure with the heater power to produce thrust efficiently, also considering the effect of both parameters on the boiling instabilities.

The following two paragraphs will explain and asses the current control mechanisms available in literature for both parameters. The proportional valve and heater chip are often controlled using a dedicated micro-controller, which is activated by the on-board computer of the satellite. It transforms the desired production of thrust to the ideal valve opening time and heater chip temperature. The micro-controller uses information of pressure and temperature sensors to adjust the input parameters if necessary, this closed-loop control improves the accuracy of the system. Ref. [49] explained the functional flow diagram of a closed-loop configuration, the diagram is shown in figure 1.6. The storage pressure is used to determine the required power for the vaporization and acceleration process. The heater is then pre-heated, before the valve is opened. The micro-controller (MSP432) reads the temperature and pressure sensors every 10 ms, to monitor the process.

Proportional Valve The proportional valve is able to control the pressure of the flow in the chamber and is therefore able to regulate the mass flow rate through the chamber. It uses a coil and a spring to control the position of the plunger, a schematic overview is given in figure 1.7. The position of the plunger determines the size of the fluid outlet. A magnetic field generated by the current flowing through the coil opposes the force of the spring and opens the valve. The orifice equation cannot be used to describe the flow through the

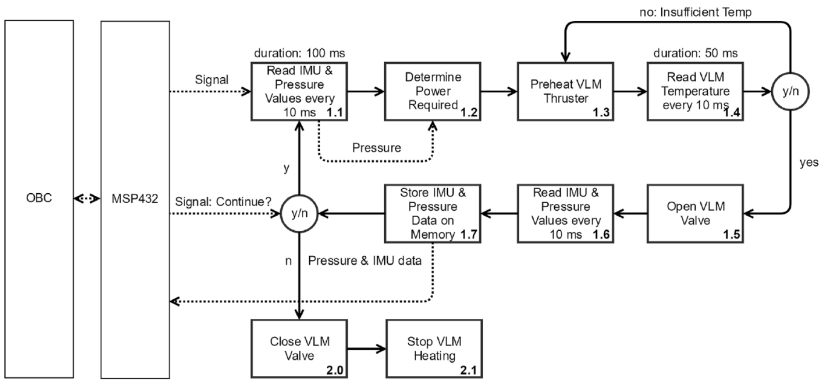

Figure 1.6: Functional flow diagram of the operational mode from Ref. [49]

nozzle, due to the rapidly occurring transient behavior during actuation. Instead, Navier-Stokes equations could be adjusted and used. The flow inside the valve is unidirectional, isothermal and in-compressible. The pressure in the tank exerts a force on the plunger in the exact opposite direction of the spring.

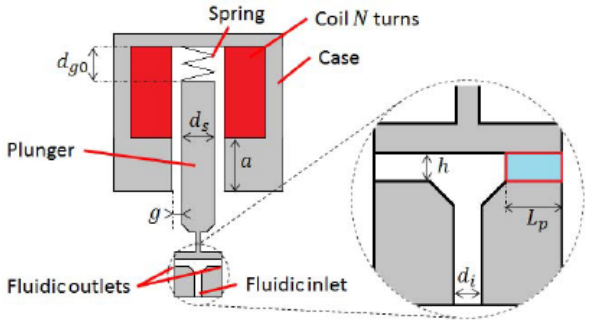

Figure 1.7: Schematic overview of the solenoid valve [54]

The state-space model of the solenoid valve from Ref. [54] is given in equation 1.13. The position of the plunger is given by $x = x_1$, the plunger velocity by $v = x_2$, the electric current by $i = x_3$ and the fluid outlet velocity by $u = x_4$. The mass flow rate through the valve and into the chamber could then be calculated using equation 1.14 using $\dot{m}_1 = y$.

$$\dot{x} = \begin{cases} x_2 \\ \frac{1}{M}(-cx_2 - k(x_1 - x_0) + F_{mag} + F_{f,pl} - p_{out}A_{in}) \\ \frac{1}{L(x_1)}(v - x_3(R_c + x_2\dot{L}(x_1))) \\ -\frac{12\mu}{\rho x_1^2}x_4 + \frac{\Delta p}{\rho L_p} \end{cases} \tag{1.13}$$

$$y = \rho x_4 A_{out}(x_1) \tag{1.14}$$

With c equal to the viscous coefficient, k equal to the elastic constant of the spring, F_{mag} equal to the magnetic force, $F_{f,pl}$ equal to the fluid force on the plunger, L equal to the inductance, R_c equal to the equivalent resistance, μ equal to the dynamic viscosity and L_p equal to the length of the section. The current through the coil generates a magnetic field, the force generated by this field opposes the force of a spring. A larger magnetic force will be able to increase the open area of the valve. It is sometimes difficult to find a proportional valve that fits within the given requirements. In that case, it is also possible to use an ON/OFF valve with a PWM signal faster than the systems dynamics [56]. The duty cycle of the PWM signal then determines the mass flow rate into the chamber. The maximum switching frequency is determined by the physical limitations of the valve.

Proportional-Integral-Derivative (PID) Control Proportional-Integral-Derivative control is a control mechanism that operates in the closed-loop configuration. The control function of a PID controller is given in equation 1.15 [55].

$$u(t) = K_p e(t) + K_i \int_0^t e(t')\,dt' + K_d \frac{de(t)}{dt} \tag{1.15}$$

$e(t)$ is the error of the system in time. K_p, K_i and K_d are the coefficients for the proportional, integral and derivative terms. A PID controller can be transformed into a PI controller by changing the derivative term (K_d) to zero. A PI controller has an advantage over a PID controller in fast processes such as pressure or flow loops. The settling time is larger, but the output is more stable and there is no overshoot visible [17]. Ref. [51] and Ref. [54] both used a PI controller for the proportional valve. Ref. [55] implemented PWM-PID control to continuously control the mass flow rate through a ON/OFF valve.

Sliding Mode Control (SMC) The Sliding Mode Control (SMC) strategy is simple in its design. The design only consists of two parts: sliding surface design and selection of the appropriate control law to keep the system close to the sliding surface [55]. The equation for a typical sliding surface should tend to zero and is given in

$$\sigma_{SMC} = (\frac{d}{dt} + p)^k \cdot e \tag{1.16}$$

Where e is equal to the output error, p could be chosen arbitrarily and $k = r-1$, with r equal to the relative degree between input-output. k is equal to 2 for a relative-degree of 3 for the state-space model of the valve, given in equation 1.13. Two different approaches are available to design the appropriate control law: first-order and high-order. First-order control is the simplest design, but the sampling time is too large for this implementation, it is not able to prevent the fully open-closed condition. The high-order control law is able to solve the shortcomings of the first-order model and is given in equation 1.17.

$$\begin{aligned} &\text{if } sign(\sigma_{SMC}) < 0 \quad \begin{cases} u = 1, 0 < t < t_{min} \\ u = 0, t_{min} < t < t_s \end{cases} \\ &\text{if } sign(\sigma_{SMC}) > 0 \quad u = 0 \end{aligned} \tag{1.17}$$

With t_{min} equal to the minimum spike time and t_s equal to the sampling rate of the sensors. This returns the control variable as a binary value for the actuation or de-actuation.

Pulsating Operation A completely different approach in proposed in Ref. [47]. The operating principle of this VLM concept is based on a pulsating operation. A single cycle consist of a thrusting period and a draining period. The thrusting period starts with the injection of liquid and ends when the valve is closed. The draining periods removes the vapor still left in the chamber and increases the chamber temperature to the desired level for the thrusting period. The opening time of the valve depends only on the storage tank pressure, because the pressure in the chamber after draining is approximately zero. They use a regulation valve to control the pressure. The length of the draining period depends on the pressure in the chamber, it ends when the pressure drops below a certain threshold.

The latter control method is especially developed for a specific design, with a larger chamber compared to the smaller MEMS devices. The pulsating operation in a MEMS vaporization chamber will probably create a lot of instabilities in the boiling process. It will also affect the efficiency of the system negatively or decrease the maximum produced thrust. The thrust during the thrusting period should be high to produce the required average thrust, because of the minimum thrust production during the draining period. This would also require a higher peak power and this is often not available. The chamber of a MEMS device with microchannels is also short and ends directly at the nozzle. The chance of expelling liquid droplets increases when there is no sufficient available heater power. More interesting are the PID (or PI) and SMC control methods. Ref. [55] compared the continuous PWM-PID control method with the discontinuous SMC control method. The accuracy of both methods are acceptable, but PWM-PID control has a better possible resolution due to a smoother response. However, a major drawback of the PWM-PID method are the higher demands for the hardware. The valve must be able to handle the high frequencies for the low mass flow rates of the system.

Heater chip The heater chip initiates the vaporization process and increases the thermal velocity of vapor before it is accelerated in the convergent-divergent nozzle. The efficiency of the VLM concept depends strongly on the thermal efficiency for the transfer of heat from the chip to the propellant. This depends on the geometry of the device, but also on the shape and position of the heater. Most recent research is currently conducted in the ability of controlling the liquid flow through the valve and vapor flow through the nozzle. The possible effect of the control of heater chip on the vaporization process still has to be investigated. Most literature provide a constant voltage to the heater chip and adjust it manually to improve the vaporization rate. A relevant control mechanism is still unavailable. The flowing paragraph will explain a simple method to keep the temperature of the heater chip within range.

Bang-Bang Control The Bang-Bang control method is proposed in Ref. [47] and is a very basic method to control the temperature of the vaporization chamber. Sensors in the chamber measure the temperature. The heater is activated when the temperature drops below the lower threshold. It stays activated until the temperature rises above the upper threshold. This reference assumes a constant heater power and uses the ON/OFF time to control temperature in the chamber.

PID Control A PID control method is also a possibility to keep the temperature of the heater within range. Ref. [29] used a PID controller to keep the temperature of the thruster a 160° Celsius. The same method is also implemented in a LPM design from Ref. [26]. They used the ability of the heater to be used as a sensor to complete the closed-loop configuration for the PID control method. The stability of a PID controller without the derivative term (PI) is less relevant compared to the control of the mass flow rate. The temperature should rise as soon as possible to the necessary temperature for complete vaporization, the overshoot will only increase the vaporization rate above the desired level.

1.1.5. Electrical Components

This section will present the available electrical implementations of the VLM propulsion system. A detailed description of the electronic subsystem of this concept is unfortunately not broadly available in literature. Most ground tests were conducted using a regular PC and a power supply. Only a few presented the design of a complete prototype for ground tests or in-orbit demonstrations. Ref. [49] presented an in-orbit demonstrator for a VLM and LPM with a single storage tank and control module. They used the requirements of the Delfi-PQ, a PocketQube from the Technical University Delft, to design the propulsion subsystem.

Micro-controller

A dedicated microcontroller is used to control the behavior of the micropropulsion system and is connected to the OBC via the electrical interface. It uses the data from the pressure and temperature sensors in combination with the commands from the OBC to control the performance using the heater chip and the proportional valve. The microcontroller is programmable and is therefore used for various applications in miniaturized spacecraft, most subsystems have their own microcontroller. A preferable programming language for microcontrollers is Arduino, which is an open source simplified language with a wide community support and a standard set of microcontrollers [12]. Ref. [49] used the MSP432 microcontroller for their in-orbit demonstrator. This is a ultra-low-power microcontroller from Texas Instruments based on a 32-bit ARM Cortex-M4F CPU [67]. Ref. [21] used the ATMega 2560 for the acquisition of the sensor values. The ATMega 2560 is a high performance, low power 8-bit microcontroller from Atmel [7]. The core features of both microcontrollers together with the Atmel SAM3X8C [8] are given in table 1.2. The biggest differences between the microcontrollers are the type of processor, maximum operating frequency and the size of the internal storage. The selection of the ideal microcontroller depends completely on the demands of the micropropulsion system.

Additional Components

The microcontroller is the core of the electronics of the propulsion system. It is not able to control the thruster without any support, additional components like sensors and analog-to-digital converters are necessary to monitor the performance. The following paragraphs will present the possible sensor configurations and present the implementations found in literature.

	MSP432	ATMega 2560	ATSAM3X8C
Processor	32-bit	8-bit	32-bit
Frequency	48 MHz	2 MHz	84 MHz
Flash Memory	up to 256 kB	256 kB	512 kB
SRAM	up to 64 kB	8 kB	96 Kb
ROM	32 kB	4 kB (EEPROM)	16 Kb
Temperature Range	-40 - 85 °C	-40 - 85 °C	-40 - 85 °C
Supply Voltage Range	1.62 - 3.7 V	1.8 - 5.5 V	1.62 - 3.6 V
Communication Modules	UART, lrDA, SPI and I^2C	USART, SPI and 2-wire	USART, UART and SPI

Table 1.2: Core features of the MSP432 [67], ATMega 2560 [7] and the ATSAM3X8C [8]

Temperature Temperature is the first important parameter for the performance of the propulsion system. The vaporization chamber of a VLM system is very small and is frequently made out of silicon (a good thermal conductor). This results in zero gradient of temperature. The temperature of the complete device is equal to the temperature of the heater chip [52]. This assumption enables the possibility to use the heater chip as an actuator and as a sensor at the same time. The temperature could be determined using equation 1.18 and is called the chamber temperature (T_c) or the wall temperature (T_w). This is also the maximum achievable temperature of the gaseous propellant before the nozzle inlet. The actual temperature of the propellant depends on the heating efficiency of the system and the pressure in the chamber. The minimum temperature is equal to the storage temperature (T_0). The boiling temperature (T_b) lies between those two, it is the maximum liquid temperature and minimum gas temperature. The size of the device and the zero gradient assumption make it very difficult, if not impossible, to determine the temperature of the propellant at different positions within the chamber and nozzle. The propellant temperature at the end of the vaporization chamber, after complete vaporization, is assumed to be equal to the chamber temperature.

$$\alpha = \frac{R - R_0}{R_0(T - T_0)} \tag{1.18}$$

Ref. [21] used a slightly different approach. They installed seven resistance temperature detectors (RTD) at different positions near the inlet section and vaporization chamber. The positions of the RTD's are shown in figure 1.8. A single device temperature assumption does not hold in this double chamber configuration. The power applied to the secondary heater is different compared to the power applied to the primary heater, resulting in temperature difference. The temperature measurements of RTD6 and RTD7 tell something about the maximum achievable propellant temperature. The implemented RTD's four wired and are made out of platinum. The analog signal from the sensors is converted to the digital domain by the MAX31865 resistance-to-digital converter [39]. This converter is able to communicate with the microcontroller using SPI, has a nominal temperature resolution of 0.03125°C and a total minimum accuracy of 0.5°C.

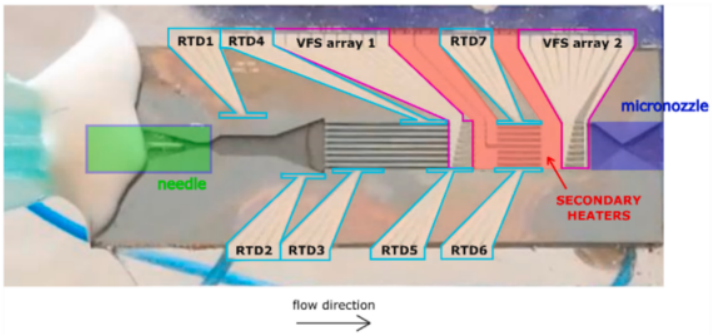

Figure 1.8: Schematic overview of the installed sensors near the MEMS microthruster [21]

Thermo-couples are in some cases an alternative for RTD's. Ref. [55] used two thermo-couples close to the nozzle to determine the actual temperature gradient between the heater chip and the nozzle area. They used

the NI 9211 thermo-couples input module for the analog-to-digital conversion of the measured temperature [46]. The module has a maximum accuracy of 2.11°C and uses a maximum of 170 mW in active mode.

Pressure Pressure is the second important parameter for the performance of the propulsion system. It is related to the propellant temperature by the Antoine equation (1.19).

$$T = \frac{B}{A - log_{10} p} + C \tag{1.19}$$

The input parameters A, B and C follow from the unit of pressure (Pa) and the temperature range (372.15-647.15 K). This results in $A = 10.27$, $B = 1810.94$ and $C = 28.67$. Four different pressures are commonly distinguished within in the propulsion system: the storage pressure, the inlet pressure, the chamber pressure and the exit pressure. The storage and inlet pressure can be determined using pressure sensors before and after the proportional valve. Ref. [21] used a commercial pressure transducer to determine the inlet pressure. The used pressure transducer has an accuracy of ±2% and could be used in the pressure range of 0-6.89 bar. The sensor could be connected to the microcontroller directly, extra drivers or converters are not necessary. Ref. [55] used the 5 bar pressure sensor MS5803-05BA before the valve to measure the storage pressure [58], which is also able to measure the temperature. It provides a 24-bit digital value and has an I^2C and SPI interface. The pressure sensor has a ±0.1 bar accuracy. They used the 30 bar pressure sensor MS5837-30BA after the valve to measure the inlet pressure [62]. This sensor also has an internal analog-to-digital converter to provide a 24-bit digital pressure and temperature value. It has an I^2C interface and an accuracy of at least ±0.4 bar depending on the pressure range. Two different sensors are selected to prevent any communication problems due to I^2C addressing conflicts.

These measurements are a bit more complicated for the chamber and exit pressures, the size and geometry of the system make it difficult to implement the appropriate pressure sensors. These two pressures depend on the boiling process in the chamber and the geometry of the chamber and nozzle. It is possible to determine the ratio between the exit pressure and the chamber pressure using the area ratio and propellant properties with equation 1.2. When the inlet pressure is measured close to the chamber, it is sometimes possible to assume that it is equal to the chamber pressure to simplify the calculations [52, 54]. This depends on the pressure drop in the chamber, a large pressure drop results in a non-uniform pressure in the chamber. The inlet pressure is only equal to the chamber pressure with a uniform pressure in the chamber. The pressure drop is affected by the geometry of the channels and configuration of the heater chip.

Evaporation Degree The boiling process in the chamber could be monitored using void fraction sensors (VFSs) to determine the evaporation degree. A pair of VFSs are placed in each microchannel, one before and one after the secondary heaters in Ref. [21]. This is also visible in figure 1.8. The VFS sensors are placed on the glass substrate and are directly in contact with the propellant. They consist out of two, 10 μm spaced, coplanar interdigitated Pt finger electrodes. The capacitance of each electrode depends on the capacitance of the finger, the capacitance of the glass substrate and the capacitance of the water layer. The latter one fluctuates due to vaporization. The AD7152 capacitance-to-digital converter is required for the sensor read-out [4]. This converter has an I^2C compatible 2-wire interface and has an resolution of 0.25 fF. This configuration needs an evaluation board to compensate for the cables parasitic capacitance.

1.2. Problem, Objective & Method

The vaporizing liquid micro-resistojet design of the Delft University of Technology is ready for the next phase of its development process. It is currently being integrated in a dual in-orbit propulsion demonstrator together with the Low Pressure Micro-resistojet (LPM). This dual demonstrator design consist of two thrusters with a single storage system, the mechanical interface and electrical components to monitor and control the performance, but the control electronics still have to be developed. The design of a single control system for both systems is out of the scope of a Master thesis research project. The focus of this project will be therefore on the control system for the VLM concept.

This research project is practice oriented and should contribute to the development process of a Vaporizing Liquid Micro-resistojet for a PocketQube. The research questions and objectives will be therefore mainly focused on the selection of a control strategy, design of the control electronics and the examination of the

potential challenges. Which results in the following main objective for this Master thesis project:

The general objective of this Master thesis project is to control a ground prototype of the Vaporizing Liquid Micro-resistojet by selecting an efficient control strategy and by designing the additional control electronics, considering the limitations based on the requirements of PocketQubes.

The first objective is the selection of the optimal control strategy to regulate pressure versus power. The selection of the required sensors, actuators and additional electrical components together with their placement, connection and usage will follow from the chosen control strategy. Both steps depend on each other, lack of required components or their integration could be the cause of changing the selected control strategy. Once all components are selected and tested in for example a basic breadboard configuration, it is possible to implement the configuration into an electronic subsystem that fits within the requirements of miniaturized spacecraft. The final objective, which will also follow the progress in parallel, is the verification and validation of the different components and the configuration of the entire system. Three important research questions, with a couple of sub-questions each, should be answered during this research project to achieve these objectives:

1. What is an efficient control strategy to regulate pressure versus power in the Vaporizing Liquid Microthruster designed for the Delfi PocketQube?
    - Which model could be used for the pressure versus power relationship?
    - What is the optimal functional flow diagram for the VLM testing mode?
    - Which control method could be used to accurately guide the proportional valve and heater chip of this propulsion system?
2. What is the ideal configuration of sensors, actuators and additional electrical components to support the selected control strategy?
    - Which sensors and actuators are necessary to meet the requirements of the selected control strategy?
    - What are the requirements of a dedicated microcontroller for this propulsion system?
    - Which additional power converters are necessary to fulfill the power demands of the microcontroller and the actuators?
3. What are the potential challenges in meeting the requirements of the propulsion system for a PocketQube?
    - What are the potential power losses of the control electronics for this propulsion system?
    - What is the impact of the selected control strategy and electronics on the performance of the VLM thruster?

1.3. Thesis Outline

This report is divided into three main chapters. The first chapter, chapter 2, presents a model to determine the optimal combination of control parameters, the operational envelopes and the control mechanisms. Three different operational envelopes are proposed in this chapter. Two for the experimental phase, to examine the behavior of the temperature and pressure control systems separately. An a final one that could be used to control the propulsive performance of the thruster. The temperature and pressure control mechanisms are given in the final section of chapter 2. Chapter 2 also discusses the measurement delays of the sensors with their potential impact on the performance. Chapter 3 covers the entire preliminary design of the hardware. The proposed hardware design is based on the control strategy from chapter 2. A complete schematic of the final design is given in the last section of the chapter, this includes some basic estimations about the power demands of the selected components. Finally, chapter 4 presents an extensive experimental phase for the chosen hardware from section 3. These experiments cover the complete temperature control system and solenoid valve control system. This chapter also considers the effect of smaller measurement delays on the quality of the measurements.

2

Operational Envelope and Control

Figure 2.1 shows a complete system diagram of the VLM control system including the important data paths. This chapter starts with the operational envelopes of both controllers, first temperature control and then pressure control. The final part of this section combines both controllers in a total operational envelope of this control system. The total operational envelope will approach the final design of the controller for this micropropulsion system. The temperature and pressure controllers are solely separated for the experimental phase of this project. Mainly to investigate and improve the behavior of the combination of hardware and software without being affected by each other.

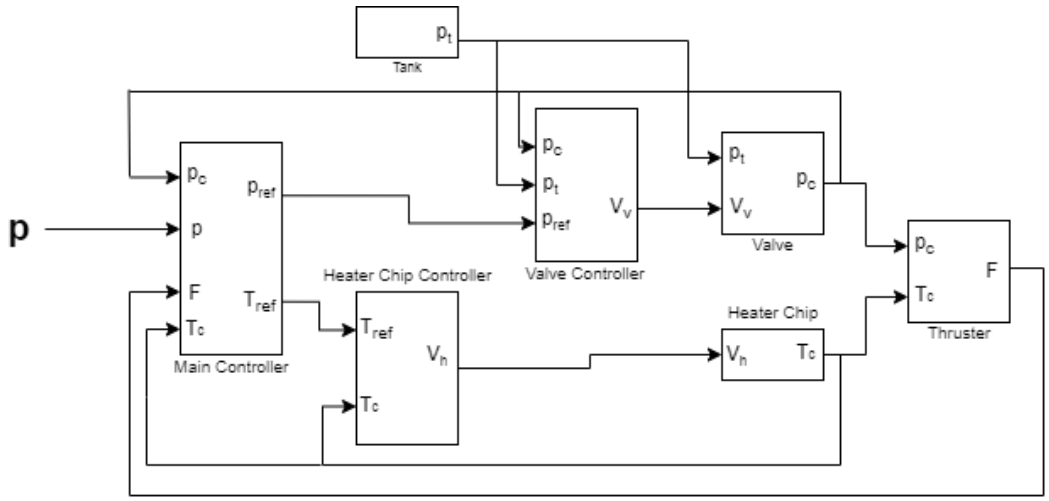

Figure 2.1: Complete system diagram with data paths and both controllers

Section 2.1 shortly explains the steps taken by the MCU to determine the optimal combination of power and pressure from the needed momentum of the OBC. Section 2.2 will present the operational envelopes of the temperature controller, pressure controller and total system controller. The control mechanisms selected to be implemented in the operational envelopes will be described in section 2.3. Finally, section 2.4 summarizes the presented control strategy.

2.1. Thrusting Performance

Power and pressure are the two main limitations for the propulsive performance. The power is of course limited by the maximum peak power of the satellite, the conversion efficiency of the buck-boost converter and power usage of additional components like the microcontroller, valve controller and various sensors. The amount of power used or lost in the complete propulsion system is estimated in section 3.4.1. This section will propose a very basic model for the MCU to translate the propulsive requirements from the OBC into an optimal chamber temperature and pressure combination. These steps are based on the model of section 1.1.4 and neglect the thermal losses, nozzle performance and boiling instabilities. These losses could have a large effect on the performance of the thruster, but their analysis is out of the scope of this thesis project. The basic model based on IRT will estimate a very optimistic thrust level when the mentioned losses are neglected in the calculations. They are therefore not essential for the operation of the control system, but will definitely improve the accuracy of the predicted total change in momentum due to the micropropulsion system.

The OBC will demand a change in momentum (thrust over time) from the micropropulsion system. The estimation of produced thrust is made using the simple model from IRT with the chosen combination of power and pressure. This estimation of thrust can be used to determine the thrusting period out of the demand of change in momentum from the OBC. It is an important control parameter for the control system, as it sets for how long the controller should be operational. The calculated thrusting period will be too small when the losses in the system are neglected, because the estimated thrust will be higher than the actual produced thrust. These deviations could be corrected using empirical relations based on experiments or by a complex model of the behavior of the flow inside the system. The deviations also depend on the performance of the designed control system and are therefore a good starting point for a future project.

The MCU should then take the power and pressure limitations into account to determine the optimal combination of chamber temperature and pressure. This is a iterative process, it first determines the maximum values and then adds the safety margins. The EPS ensures that the pre-arranged amount of peak power (4 W) can be used by the propulsion system for the entire duration of the thrusting period. The amount of available heating power could be determined with equation 2.1

$$P_{heater} = (P_{peak} - P_{electronics} - P_{solenoidvalve}) \cdot \eta_{conversion} \tag{2.1}$$

P_{heater} is the amount of power that could be supplied to the heater chip. A part of the thermal energy will not be absorbed by the vaporization process, but will be lost into the environment as heat. The empirical relation of Ref. [23] (equation 1.11) is based on the power supplied to the heater, so it combines the energy for the vaporization process with the energy lost into the environment. This relation could be very useful for the experiments on earth, but should be improved to meet the orbital conditions. The very simple model gives in that case a good first estimation of the maximum chamber pressure for a certain amount of available power. A complex thermal model could also determine the percentage of energy that is lost into the environment, but this is out of the scope of this thesis project. Equation 1.11 is sufficient to explain the basic calculation steps of this section.

The pressure determined with equation 1.11 is a maximum value for a given amount of available heating power. The risk of a total system failure due to incomplete vaporization of the propellant is too large to operate close to the boundaries. Small pressure fluctuations in the chamber might cause some minor overshoot in pressure and therefore mass flow rate. The temperature controller will not be able to increase the heating power for a higher mass flow rate when it is already operating at its maximum. An incomplete vaporization process will affect the thrusting performance and might even lead to a frozen nozzle. A safety margin has to be taken into account for the heating power, pressure or both. The size of the margin depends on the performance of the control system and can be determined with experiments.

Chamber pressure is the first main control parameter, directly measured with a sensor at the chamber inlet and controlled with the solenoid valve. Although the heating power is mentioned to be the second limitation to the propulsion system, it can not be used to control the thrusting performance. The amount of heating power transferred to the propellant fluctuates due to its environment. The heater temperature is therefore selected to be the second main control parameter. The chamber temperature is assumed to be equal to the heater temperature due to the used material and its size. The chamber temperature should be

equal to or higher than the vaporization temperature of the propellant.

The maximum chamber pressure is not only limited by the heating power, but also by the storage pressure. The liquid feed and storage system is simple in its design, so it is not able to increase the chamber pressure above the storage pressure. The actual maximum follows from the storage pressure minus the pressure drop of the feed system and solenoid valve. This will not be a limiting factor at the start of a mission, but could certainly affect the thrusting performance at the end of the mission. The storage pressure is always checked before the thrusting operation to verify whether the maximum chamber pressure could be achieved. The safety margins will be included in the calculations once the maximum achievable chamber pressure is known.

Figure 2.2 shows the calculation steps to the final controller inputs. The heater chip power is used to determine the maximum chamber pressure. A safety margin is then distracted from the maxim pressure, a safety margin of 20% is used in this example. The determined pressure is then used to determine the vaporization temperature with equation 1.8. A temperature safety margin is then added into the positive direction, 10% in this example. These final pressure and temperature parameters are used as the reference input for both controllers. The size of both margins depend on the performance of the control systems. Large fluctuations or slow responses to changes require larger safety margins. They have to ensure that the top level of the pressure never requires a vaporization temperature that exceeds the bottom level of the controlled chamber temperature. The other way around is less risky, but should be minimized to improve the thrusting performance.

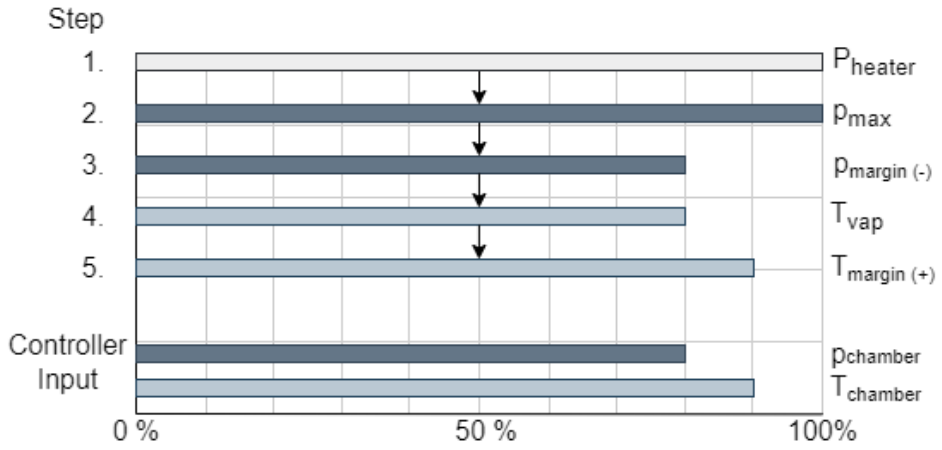

Figure 2.2: Calculation steps to determine the optimal control parameters

The only parameter that still has to be determined is the thrusting period. The thrusting period follows from the demanded momentum and the produced thrust. A starting point for the thrust is the ideal rocket theory (IRT). These equations provide a thrust level without considering any losses due to the nozzle performance and the vaporization process. A comprehensive model has to be generated to take these losses into account. Various models are proposed in previous work that use semi-empirical relations to improve the performance estimations of a VLM micropropulsion system. This literature is shortly mentioned in section 1.1.4. Additional research should be conducted to create an accurate model for the final prototype of this propulsion system, but that is out of the scope of this thesis project.

2.2. Operational Envelope

This section will explain the different functions necessary to perform a successful propulsive operation. First a short introduction will be given using the top level functional flow diagram. The top level flow diagram is given in figure 2.3.

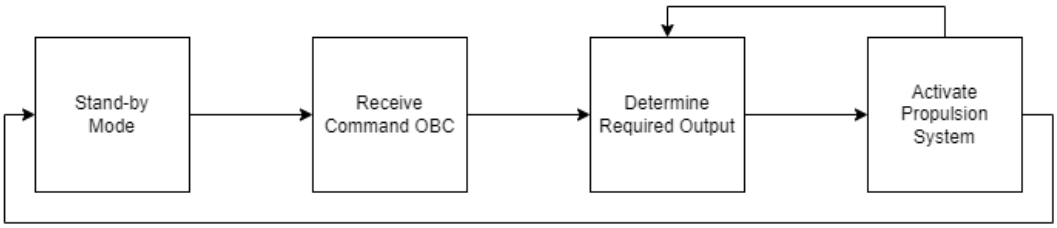

Figure 2.3: Top level functional flow diagram of VLM control system

Each propulsive operation always starts and ends in the stand-by mode with minimum activity to safe power. The system remains in stand-by mode until it is activated by a command from the OBC with the propulsive requirement, the momentum [N·s] or in case of the temperature and control testing loops a temperature or pressure requirement. The MCU translates the commanded data into an optimal power/pressure relation and a certain thrusting period. The system always starts with a first round of measurements to determine the current temperature and pressure conditions of the thruster. These results will be used by the controllers to calculate the necessary output of the actuators. The actuators are then activated for the propulsive operation. That control loop of measuring and actuating is repeated until the thrusting period is finished or until a new signal from the OBC is received.

2.2.1. Temperature Control

A functional flow diagram to control the temperature of the heater chip is given in figure 2.4. The temperature control system receives two possible input signals from the OBC or the top level control loop of the microcontroller, the reference temperature (T_{ref}) and a stop signal ($Stop$). The temperature reference signal is also the signal to initiate the temperature control loop and could be used to change the reference temperature during operation. The starting point ($T_{x-1} == 0$) checks if the system is already in operation to see whether the system could go back into the control loop or first needs to go through the start-up sequence. The start-up sequence is necessary to collect the first temperature data, which is only possible after applying power to the heater chip. The lowest possible voltage value (V_{min}) is applied to decrease the dissipation of power and prevent the heaters from overheating.

The two temperature data reading blocks are separated on purpose. Collecting data from the sensors is a time consuming task and the main control loop on the bottom of figure 2.4 should be fast to increase the ability of the system to react to abrupt temperature differences. The temperature measurements are, on the other hand, not very stable. An average value of 10 measurements or more, when the start-up sequence could be extended, will increase the accuracy of the measurement, but take too much time to be implemented in the main control loop. Exponential smoothing is used to remove minor deviations due to noise or the instability of the buck-boost converter, the first order exponential filter is given in equation 2.2. The smoothing factor w determines weight difference between the measured value and the previous result from the filter (or average from previous block in starting sequence). It depends on the stability of the system and rate of temperature variations. The factor should be determined with experiments during propulsive tests and probably needs some iteration steps to find the optimal value.

$$T_{smooth} = w \cdot T_x + (1 - w) \cdot T_{smooth-1} \tag{2.2}$$

The other three blocks in the main control loop apply PID control to the error signal, control the digital potentiometers and check if there is a new input signal available. The PID controller for the temperature control loop will be explained in section 2.3.

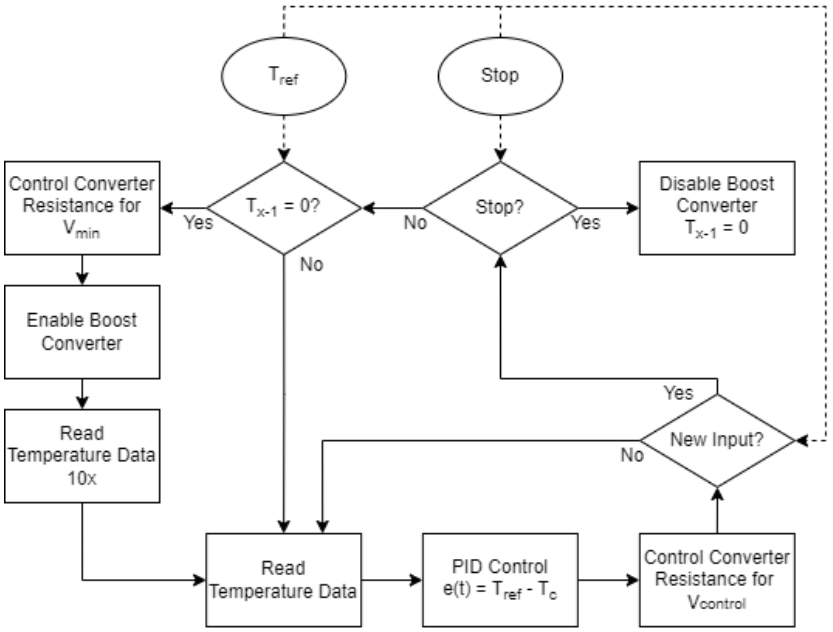

Figure 2.4: Functional flow diagram to control the temperature of the VLM propulsion system

Temperature Measurement Delay

The temperature is determined with the heater chip voltage and current measurements, collected by a combination of an ADC (ADS1115 [65]) and a hall effect current sensor (ACS712 [3]). The ADC directly converts the analog heater chip voltage signal and converts the continuous analog signal from the current sensor. The digital measurement data is then transferred to the microcontroller using I2C. Both steps, analog to digital conversion and data transfer, require a certain amount of processing time. The processing time is only affected by the ADC and the microcontroller, because of the continuous operation of the current sensor.

An initial speed test with the ADC connected to the microcontroller showed that it takes approximately 18.61 ms for the temperature measurement function to run with the sensor in the default setup. A more extensive examination of the processing steps in the function made clear that most of that time is lost due to the conversion time of the ADC. It operates in a single shot mode and therefore starts the conversion once it is asked by the microcontroller, a single conversion with data transfer of either the voltage or the current takes approximately 9.14 ms. Continuous operation mode could reduce the processing time, because the ADC continuously converts one of its differential inputs and places that result in the conversion register. The MCU can easily read that register, but it is unknown which converted input is placed into the register and the conversion time between a voltage and current measurement stays the same. These disadvantages could be partly solved using interrupts, these interrupts will however increase the complexity of the system.

The ADC also offers the functionality to reduce the conversion time. The conversion time is equal to 1/DR. DR is the data rate of the converter and ranges from 8 samples per second (SPS) to 860 SPS [65]. The default value is 128 SPS, which results in a conversion time of 7.81 ms. The conversion can be reduced to 1.16 ms for the data rate of 860 SPS. The total processing time to determine the temperature of the heater chip is thus reduced to 5.47 ms. Increasing the data rate does, unfortunately, not only have a positive influence on the performance. Minimizing the output data rate of analog-to-digital converters reduces the noise on the measurements, because more samples are averaged [65]. This concept is called oversampling and the oversampling ratio (OSR) is the ratio between the frequency of the modulator and the output date rate. The datasheet of the ADS1115 [65] considers two possible important effects of a higher output data rate, the input-referred noise and effective resolution. The input-referred noise increases and effective resolution decreases for larger SPS rates.

At this stage in the development process, it is difficult to predict what the negative impact on the accuracy

of the temperature measurements will be. Experiments in chapter 4 should provide the ability to assess the influence of an increased data rate. It is important to notice that this modification to the data rate almost reduces the measurement time with a factor of 4. Meaning that at least three measurements (and control cycles) could be conducted in the same period of time. This will let the temperature control system react faster on sudden changes in heater chip temperature, reducing the chance of incomplete vaporization during a thrusting period.

2.2.2. Pressure control

A functional flow diagram to control the pressure in the chamber is given in figure 2.5. The pressure control system could receive two possible input signals from the OBC or the top level control loop of the microcontroller, the reference pressure (p_{ref}) and a stop signal ($Stop$). The pressure reference signal is also the signal to initiate the pressure control loop and could be used to change the reference pressure during operation. The main difference between the temperature and pressure functional flow diagram is the necessity for a start-up sequence. The start-up sequence is important for the first measurement of the temperature in figure 2.4, due to the voltage and current sensors. They require a certain voltage over and a current flowing through the heater chip to measure its resistance, which needs to be applied during the start-up sequence before the first measurement. In addition, they need a accurate starting value for the exponential filter, obtained by taking the average of ten measurements during that start-up sequence. The pressure sensor does not need any kind of flow to measure the pressure in the chamber. The fast dynamics of the pressure in the chamber remove the possibility to use an exponential filter for the pressure measurements, so an initial accurate pressure value does not have to be determined. There are also no signs that the pressure measurements are very unstable at this phase of the development process. A combination of these assumptions removes the necessity of a start-up sequence in the pressure control loop. The pressure in the chamber will be measured using pressure sensor at the inlet in the 'Read Pressure Data' control block. The measurement delay of this control block will be examined in the next section.

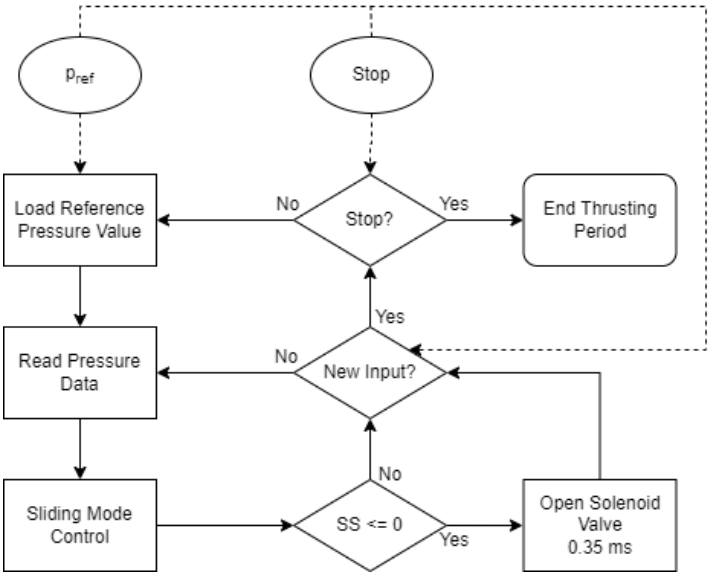

Figure 2.5: Functional flow diagram to control the pressure of the VLM propulsion system

The main control loop of figure 2.5 starts once the reference pressure is stored in the buffer. The MCU will then collect the measurement data. The Sliding Mode Control (SMC) block can start with its computations when the reference and measured pressure are available, these computations will result in the Sliding Surface (SS). A SS smaller than or equal to zero will activate the solenoid valve control sequence, which opens the solenoid valve for the minimum spike time of 350 μs. The system then checks whether a signal from the OBC or top level control loop of the MCU is received, before it could continue in the pressure control loop.

Pressure Measurement Delay

The pressure is determined by two sensors, one at the inlet of the chamber and one in (or near) the storage tank. Both sensors are from the TE Connectivity series MS5837. The trade-off between the different models will be extensively described in section 3.2.3. The sensor with the smallest pressure range and therefore highest resolution is selected for the application at the inlet of the chamber. This is the MS5837-02BA digital pressure and temperature sensor [60]. The selection of the ideal sensor for the storage pressure depends on the initial storage pressure during the launch. The MS5837-07BA will be selected when the initial storage pressure is smaller than 7 bar, mainly because of its better resolution [61]. The MS5837-30BA is only necessary when the initial storage pressure exceeds the pressure level of 7 bar.

An initial speed test with one of the sensors from the MS5837 series showed that it takes approximately 42.00 ms to collect the pressure and temperature data with the sensor in the default setup. The working principle of the pressure and temperature sensors of the MS5837 series is similar. They communicate with the MCU using I2C and can be controlled using an available Arduino library. The library simplifies the commands of the main Arduino program into only a few basic commands to set up and control the sensors. The sensor has two data registers, D1 (pressure) and D2 (temperature). The basic 'read' command of the library initiates a function that starts the communication with the sensor and requests a conversion for one of these registers (e.g. D1). The function then waits for a safety conversion delay of 20 ms, before the data of that same register could be collected. The same steps are repeated for the second data register (D2). The data bits from both register are then converted into pressure and temperature values. These steps combined explain the 42.00 ms measurement delay of the MS5837 series.

The safety conversion delay of the library is based on the maximum conversion time of 17.2 ms (MS5837-02BA) or 18.08 ms (MS5837-07BA/MS5837-30BA) for the default over sampling rate (OSR) of 8192. The OSR improves the resolution and signal-to-noise ratio (SNR) by sampling at a sampling rate 'N' times higher than the Nyquist rate [24]. A smaller OSR will decrease the resolution and SNR, but will also increase the conversion time. The optimal configuration depends on the dynamics of the system. The solenoid valve will open for a minimum spike time of 350 μs (or something in the same order) and needs to be closed for a much longer period of time according to the experiments conducted in Ref. [55]. But it seems to be illogical to assume that does not have to let any propellant pass for the next 42.00 ms or even 84.00 ms when the chamber pressure in the first loop is still too high. That would make the pressure rise time at least 120 times larger than the pressure decay time. It seems to be reasonable to assume that the measurement delay of the pressure sensors should be reduced.

The sensors require two different internal conversion steps in its default configuration. First the conversion of the pressure and then the conversion of the temperature. The temperature measurements of the sensor at the inlet at the chamber will not be used in the main control loop. The inlet pressure is less important for the power vs. pressure relation compared to the exit temperature. Measurements with the heater chip will give a better approximation of the propellant exit temperature. It is unfortunately not possible to remove the internal conversion of the temperature from the sensor operation. The temperature data is necessary in the conversion step on the MCU to transform the incoming pressure bit value into an actual pressure value. Both internal conversions of the sensors are necessary for an accurate measurement result.

The second possible path to a shorter measurement delay is to realize a shorter conversion by decreasing the OSR. Table 3.3 gives an overview of the measurement characteristics of the three sensors from the MS5837 series for the possible OSR's [60–62]. Their conversion times per OSR are almost the same. The conversions rates of the MS5837-02BA are slightly faster, but the difference is, especially for a lower OSR, negligible. More or less the same could be said about the temperature resolution, with similar characteristics. The temperature measurements are less important and will probably only be used to monitor the temperature of the storage tank, in which a far poorer resolution is also acceptable. The main difference is presented in the pressure resolutions of the sensors. The worst resolution will be obtained by the MS5837-30BA, its resolution is in a different order compared to the other two. There is still a difference visible between the MS5837-02BA and the MS5837-07BA, but its relatively small compared to the their difference with the MS5837-30BA.

A trade-off should be made between the conversion time and the resolution of the sensor. The conversion

Parameter	Sensor	8192	4096	2048	1024	512	256
Max. Conversion Time [ms]	MS5837-02BA	17.2	8.61	4.32	2.17	1.10	0.56
	MS5837-07BA	18.08	9.04	4.54	2.28	1.17	0.6
	MS5837-30BA	18.08	9.04	4.54	2.28	1.17	0.6
Pressure Resolution [mbar]	MS5837-02BA	0.016	0.021	0.028	0.039	0.062	0.11
	MS5837-07BA	0.031	0.044	0.061	0.089	0.133	0.242
	MS5837-30BA	0.20	0.28	0.38	0.54	0.84	1.57
Temperature Resolution [°C]	MS5837-02BA	0.002	0.003	0.004	0.006	0.009	0.012
	MS5837-07BA	0.002	0.003	0.004	0.006	0.009	0.012
	MS5837-30BA	0.0022	0.0026	0.0033	0.0041	0.0055	0.0086

Table 2.1: Performance characteristics at different over sampling rates (OSR) for the MS5837-02BA [60], MS5837-07BA [61] and MS5837-30BA [62]

time depends on the dynamics of the system. A faster decay of the pressure in the chamber would require faster control loop, to activate the solenoid valve at shorter time intervals. This will also allow the system to react faster on unexpected changes in the chamber pressure. On the other side there is the resolution of sensor, which will affect the power vs. pressure relation. The experiments conducted in Ref. [23] resulted in a linear power vs. pressure relation, presented in figure 1.5. The coefficient of the linear equation from Ref. [23] is presented to be approximately 3.01 - 3.38 $\frac{mW}{mbar}$ for different thruster configurations. An average value of 3.20 $\frac{mW}{mbar}$ will be used to determine the effect of the resolution on the performance.

Equation 2.3 shows the effect of a different pressure resolution on the required accuracy of the heating power. A very high resolution in the pressure measurements is only useful when the heating power can be controlled sufficiently.

$$\begin{aligned} \Delta P_{8192} &= a \cdot R_{8192} = 3.20 \cdot 0.016 = 0.051\, mW \\ \Delta P_{256} &= a \cdot R_{256} = 3.20 \cdot 0.11 = 0.352\, mW \end{aligned} \tag{2.3}$$

It becomes more clear when the power accuracy is translated to the output voltage of the buck-boost converter. A heater chip resistance of 3.40 mΩ will be assumed to determine the required accuracy of the buck-boost converter at different OSR's. These results are given in equation 2.4.

$$\begin{aligned} \Delta V_{8192} &= \sqrt{R \cdot P_{8192}} = \sqrt{3.40 \cdot 0.051 \cdot 10^{-3}} = 13.17\, mV \\ \Delta V_{256} &= \sqrt{R \cdot P_{256}} = \sqrt{3.40 \cdot 0.352 \cdot 10^{-3}} = 34.59\, mV \end{aligned} \tag{2.4}$$

The decision for the final ideal OSR for this setup can be made once the pressure dynamics of the thruster and achieved accuracy of the adjustable power supply are known. It can be noticed that the effect on the output voltage between the highest and lowest OSR is not very large, while the difference in conversion time is large. Therefore it seems to be obvious that smaller OSR's will improve the controllability of the system due to the reduced duration of the pressure control loop. Reducing the OSR will also have a negative impact on the SNR, which could affect the stability of the measurements. The datasheet of the sensors does not provide additional performance parameters for the SNR at different OSR, so experiments should show how large the actual impact of a smaller OSR will be on the quality of the measurements. These experiments are unfortunately out of the scope of this thesis project and will be added to the recommendations in section 6.

2.2.3. Combined Control

A functional flow diagram to control the thrusting period of the this micropropulsion system is given in figure 2.6. The pressure control system could receive two possible input signals from the OBC, the demanded momentum (p) and a stop signal ($Stop$). The demanded momentum is also the signal to initiate the propulsive control loop and could be used to change the propulsive performance during its operation. The functional flow diagram of figure 2.6 combines the individual control loops for the temperature and pressure. Those loops are designed to be used during the experimental phase of the current and upcoming projects. The

combined control loop that is proposed in this section is a preliminary designed control loop that should be optimized in de upcoming projects.

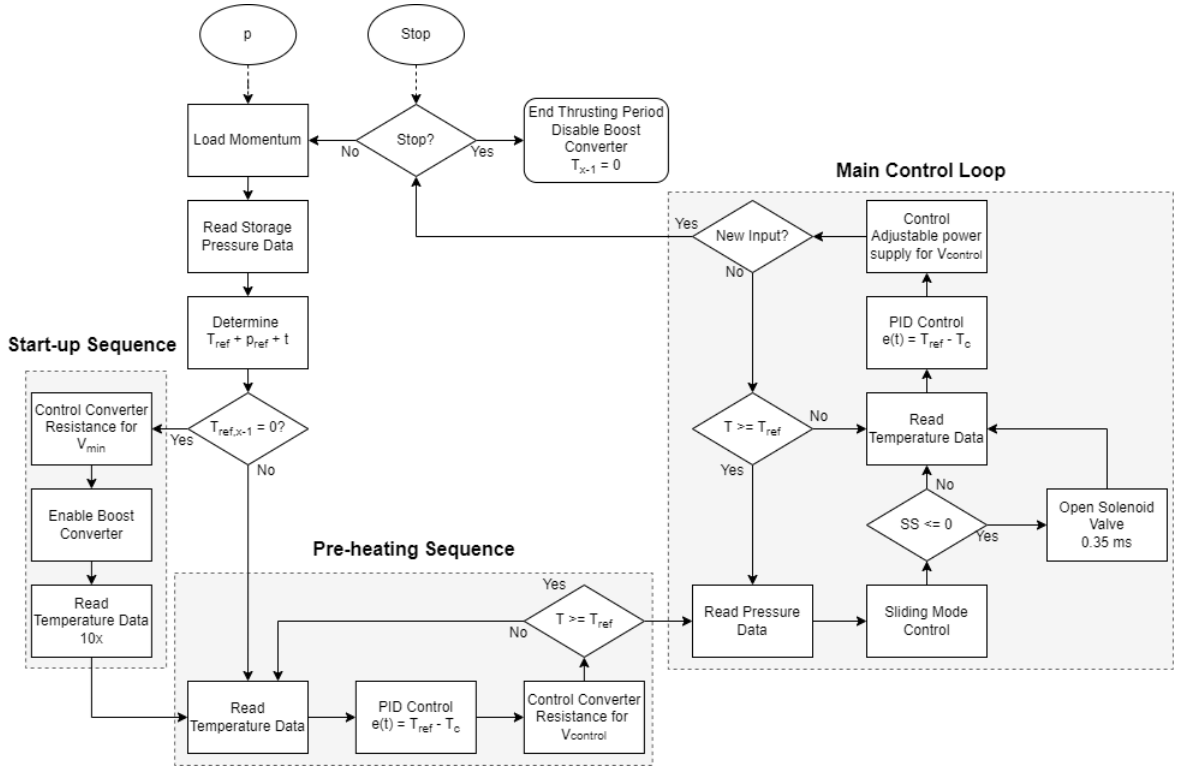

Figure 2.6: Functional flow diagram to control the thrusting of the VLM propulsion system

The control loop receives the momentum from the OBC and combines it with the current storage pressure to determine the optimal chamber temperature and pressure combination. An estimation of the propulsive performance will be made to determine the length of the thrusting period. The first two sequences follow from the temperature control loop. The start-up sequence is important to initiate the temperature measurements of the heater chip. The second sequences ensures that the minimum chamber temperature is reached before the first propellant will enter the chamber for the vaporization process.

The main control loop starts with four blocks from the pressure control loop. These blocks will first determine the current chamber pressure and then perform SMC to determine whether the valve should be activated or not. This first pressure measurement step might be useless when the thruster is activated after a long stand-by period, but could be important when a new signal is received from the OBC. The path back to the main control loop is relatively short and the pressure in the chamber could still be sufficient. Further increasing the chamber pressure could result in a incomplete vaporization process. The temperature is being controlled after the solenoid valve is activated to counteract on the energy lost to the vaporization process. The final check before the system continues to read the pressure data is important for a complete vaporization process. The chamber reference temperature has an operational range with a minimum temperature at the safety margin above the vaporization temperature. The safety margin ensures that chamber temperature will not drop below the vaporization temperature after the propellant enter the chamber. The final check verifies if it is safe to increase the chamber pressure. This is a last call safety measure and should be avoided to keep the main control loop running. A distance between the safety margin and the reference temperature for PID control will ensure that the temperature stays above the safety margin.

The main challenges in the propulsive control of this VLM system are the measurement delays of the temperature and pressure sensors. The considerations about the measurement delays are extensively described in the previous two sections. These sections concluded that additional experiments are necessary to complete the trade-off between the measurement quality and conversion time. The outcome of that study could

affect the functional flow diagram of the control loop. The same applies to the dynamics of the thruster. A relatively stable chamber temperature and large temperature measurement delay could be a reason to take temperature control out of the main control loop. A temperature check once every few pressure cycles could be sufficient in that case. This is a bit more complicated for the pressure because of the vaporization process with boiling instabilities. A good model of the pressure drop in the feed system and behavior of the flow in the chamber could predict rise and decay time of the pressure. This could make it possible to have a few loops without a pressure measurement. These considerations are out of the scope of this thesis project and should be handled during the experimental phase with the final hardware prototype.

2.3. Control Strategy

A control strategy for a single or a set of parameters will help the system to reach and maintain a required level. The strategy's are presented for the two main parameters of the propulsive performance, the chamber temperature and chamber pressure. The temperature and pressure are connected and limit each other. The pressure in the chamber may not exceed a certain value when the chamber temperature is restricted by the available amount of heating power. Exceeding the pressure limit could result in an incomplete vaporization process, which will reduce the propulsive performance and will increase the risk on a frozen nozzle. The temperature is not directly restricted by the pressure. Ref. [69] showed that its less efficient in terms of mass flow rate and power transferred to the propellant when the temperature is constant and far above the vaporization temperature. Both parameters should balanced for the optimal performance. This section presents two different control strategy's, one for each parameter, based on analysis of the current design and literature.

2.3.1. Temperature Control

Temperature is the first main control parameters of the designed VLM micropropulsion system. The minimum chamber temperature for a complete vaporization process is equal to the vaporization temperature. The vaporization temperature depends on the characteristics of the propellant and the chamber pressure. The proposed control strategy for the chamber pressure will be described in the next section. Section 1.1.4 mentioned that an ideal control strategy is still unavailable for the temperature in the chamber. Previous research applied a constant power to the heater chip or changed it manually. Bang-bang control from Ref. [47] activate the heater when its temperature drops below a lower threshold. The heater stays activated until the temperature exceeds the upper threshold. The VLM design of Ref. [47] is incomparable with the VLM design of this project. The half-sectional view of that design is given in figure 1.4a. The design has a vaporization room and different labyrinth shaped channels to the different thrusters. The labyrinth shaped channels are designed to block the liquid droplets from leaving through the nozzles. The path from the vaporization room to the nozzles is large enough to collect the remaining liquid droplets. The vaporization process also continues the labyrinth shaped channels, so there is more time to correct the temperature when it drops below a certain minimum. This unfortunately not the case for the VLM design of this project. The length of the vaporization chamber is small and directly attached to the nozzle. ON/OFF control might work for their design, but is very risky in the design for this project due to the measurement delay's and the reaction time of the actuator.

Ref. [29] used PID control to keep the chamber temperature of the thruster constant. PID control is a closed-loop control mechanism that uses the process measurements as feedback to determine the necessary output. The control function of a PID controller is given in equation 2.5.

$$u(t) = K_p e(t) + K_i \cdot T_s \int_0^t e(t')\,dt' + \frac{K_d}{T_s} K_d \frac{de(t)}{dt} \tag{2.5}$$

$e(t)$ is the error of the system in time. K_p, K_i and K_d are the coefficients for the proportional, integral and derivative terms. These terms affect the response of the control system. The derivative term is sometimes removed to increase the stability of the controller and reduce the overshoot, but that will also increase the settling time of the process [17]. This is especially relevant for the other main control parameter of this section, the chamber pressure. The pressure may not exceed a safety threshold to ensure a complete vaporization process. A large overshoot is therefore unacceptable. On the other side, a large settling time for the pressure does not have a large negative impact on the vaporization process. The settling time is more important when the temperature is too low, which may pose a risk to the vaporization process and the temperature should therefore rise quickly. A bit more overshoot will only increase the temperature a bit too much. Affecting the efficiency of the thruster, but does not increase the risk to a potential failure. PID control is therefore

chosen over PI control to regulate the temperature in the chamber.

The coefficients of a PID controller must be tuned using the dynamics of the feedback control loop of the system. The feedback control loop consists of three main blocks: the PID algorithm, the process and the measurements. The PID algorithm uses the error signal in equation 2.5 to determine a control variable (CV) for the heater chip, a power signal for the control function of the adjustable power supply. The error signal is determined with equation 2.6.

$$e(t) = SP - PV \tag{2.6}$$

The set point (SP) is the reference temperature and the process variable (PV) is the measured temperature of the heater chip. The process is the conversion of electrical energy into thermal energy by the heater chip. Ref. [54] modeled this process as a linear first-order system, the transfer function of this system is given in equation 2.7.

$$\frac{T(s)}{P(s)} = \frac{K}{s + \frac{1}{\tau}} \tag{2.7}$$

With K equal to 28.5 $\mathrm{KW^{-1}s^{-1}}$ and τ equal to 119.5 s. The measurement block is converts the voltage and current of the heater chip into the temperature PV signal. The feedback control loop will be modeled using Simulink, a block diagram environment of Matlab [28]. A block diagram of the temperature control feedback loop is given in equation 2.7.

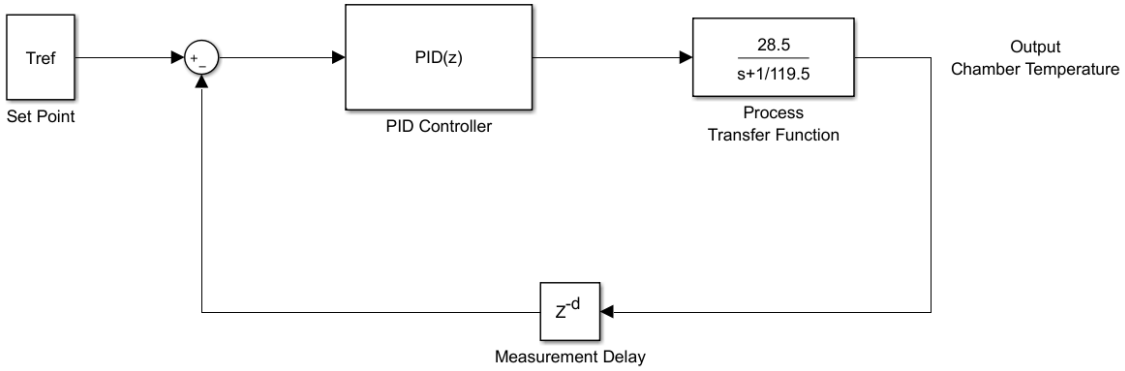

Figure 2.7: Feedback loop of the temperature control process

The measurement block is given by a delay in Simulink. This does not have to be an additional conversion block, because of the temperature output of the process transfer function. The conversion block in the actual design is necessary to convert the current and voltage to the heater chip temperature. The measurement delay depends on the speed of the voltage and current measurements to determine the temperature of the heater chip, as is described in section 2.2.1. The measurement delay at a default value of 128 SPS for the analog-to-digital converter is equal to 18.61 ms. This delay could be reduced to 5.47 ms for a SPS of 860.

The PID coefficients are tuned manually using the PID tuner from Simulink. The upcoming results are only based on the heater chip model and measurement delay. They represent an initial estimation of the final step response of the temperature control loop. These results should be further optimized using measurement results obtained in near operational conditions. Important considerations for the manual tuning method are the rise time, maximum overshoot and stability. The step response for the maximum measurement delay is given in figure 2.8. The coefficients of the PID controller are given in 2.8. The response has a rise time of 3.63 s and a maximum overshoot smaller than 10%. A smaller settling time would have a negative effect on the stability of the response and would increase the maximum overshoot. Previous conducted experiments experienced the vulnerability of the heater chip, which could be damaged by overheating [23]. Additional research should be conducted to determine how large the overshoot may be without damaging heater chip.

$$\begin{aligned} K_p &= 0.024099 \\ K_i &= 0.002738 \\ K_d &= 0.003084 \\ t_s &= 18.61ms \end{aligned} \tag{2.8}$$

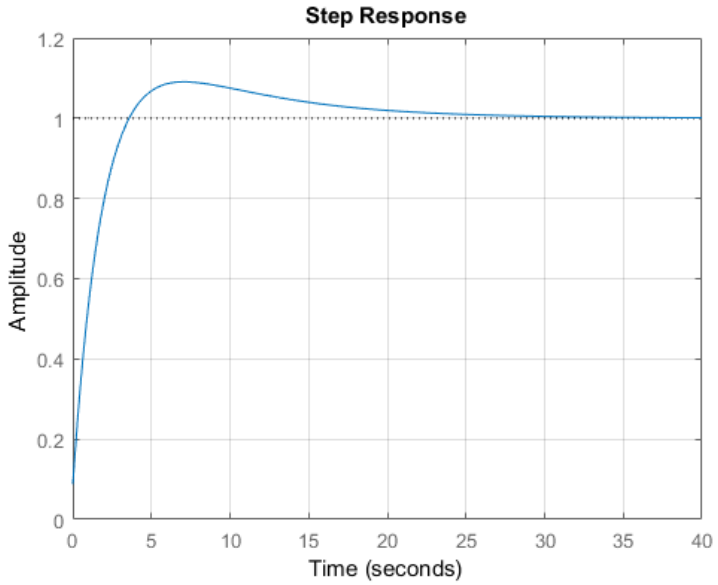

Figure 2.8: Step response of PID control with a maximum measurement delay

The step response for the minimum measurement delay is given in figure 2.9. The coefficients of the PID controller are given in 2.9. The response has a rise time of 1.22 s and a maximum overshoot smaller than 10%. A smaller measurement delay improves the speed of the control system. The rise time decreases with approximately the same factor as the decrease in measurement delay. More or less the same applies to the settling time of the step response. This improves the efficiency of the heating process. The part in both figures below the graph and above 1 represents energy that is not really necessary for the vaporization process. The overshoot time with a large delay is much longer compared to the overshoot time with a shorter delay. This indicates that the system will become more efficient for a reduced measurement delay. It should be noticed that this model only considers the transfer function of the heater chip without considering any disturbances. The system is also affected by its surroundings, the thermal isolation of the thruster and propellant flow in the chamber. These disturbances will have a mostly negative impact on the heating performance and will affect the time and input power to reach the required chamber temperature.

$$\begin{aligned} K_p &= 0.069381 \\ K_i &= 0.023004 \\ K_d &= 0.003058 \\ t_s &= 5.47ms \end{aligned} \tag{2.9}$$

2.3.2. Pressure Control

The chamber pressure is the second important control parameter of the designed VLM micropropulsion system. Ref. [55] proposed PID control and sliding mode control (SMC) to regulate the pressure in the chamber of a VLM micropropulsion system. Results from that work showed that PID-PWM control can not be used in the current design due to the performance of the solenoid valve, which is not able to operate with the low required mass flow rates. A hybrid SMC mechanism is successfully proposed and tested as a simple and reliable method to control the pressure in the chamber. The hybrid control law is given in equation 2.10.

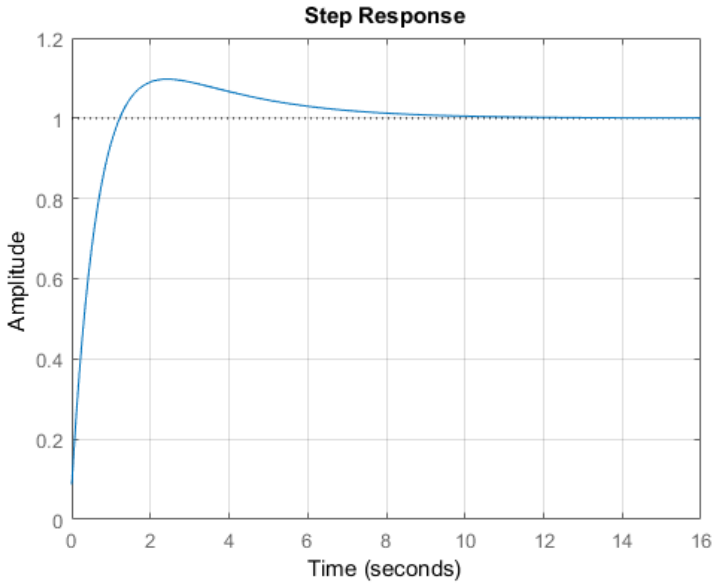

Figure 2.9: Step response of PID control with a minimum measurement delay

$$\begin{aligned} &\text{if } sign(\sigma_{SMC}) < 0 \quad \begin{cases} u = 1, 0 < t < t_{min} \\ u = 0, t_{min} < t < t_s \end{cases} \\ &\text{if } sign(\sigma_{SMC}) > 0 \quad u = 0 \end{aligned} \tag{2.10}$$

With t_{min} equal to the minimum spike time and t_s equal to the sampling rate of the sensors. σ_{SMC} is the sliding surface that is determined by a constant p (chosen arbitrarily) and current, first derivative and second derivative of the error. The error is again the difference between the set point and the process variable. The equation for the sliding surface is given in 2.11. With k is equal to 2 for a relative-degree of 3 for the state-space model of the valve, which is given in equation 1.13.

$$\sigma_{SMC} = (\frac{d}{dt} + p)^k \cdot e \tag{2.11}$$

This equation can be re-written with k equal to 2, this results in equation 2.12 for the sliding surface.

$$\sigma_{SMC} = \frac{d^2 e}{dt^2} + 2 \cdot p \cdot \frac{de}{dt} + p^2 \cdot e \tag{2.12}$$

Figure 2.10 shows the experimental results from Ref. [55] for a step-wise increase and decrease of the pressure using the hybrid SMC model. The right graph shows the operating principle of SMC, with more valve actuation's for higher pressure references. The valve always opens completely, so each activation always reaches 1 (or 100%) for a full (blue) spike. The density of the spikes is lower for smaller demanded pressures at the start and end of the experiment. The density of the spikes in the center of the graph is higher, resulting in a higher average pressure. This is also visible in the left graph of figure 2.10 in the range of 325-350 ms. The minimum period between two activation's of the solenoid valve is limited by sampling time of the system. The maximum period depends on the pressure set point. A very high demanded average chamber pressure would result in a small period between two valve activation's, more spikes in a shorter period of time. The rise time of the pressure is constant and the decay time determines the average pressure in the chamber. The decay time is extended when the pressure should drop to a lower value. This is visible at ±350 s and at ±385 s with a relatively long period without a spike.

The experiments from Ref. [55] resulted in a response time of 1.5 s for a pressure step of 200 mbar, an error smaller than 2% and a resolution of approximately 50 mbar. These results are achieved with a sampling time of 40 ms with the pressure sensor in the default setting. A smaller sampling time would decrease the interval

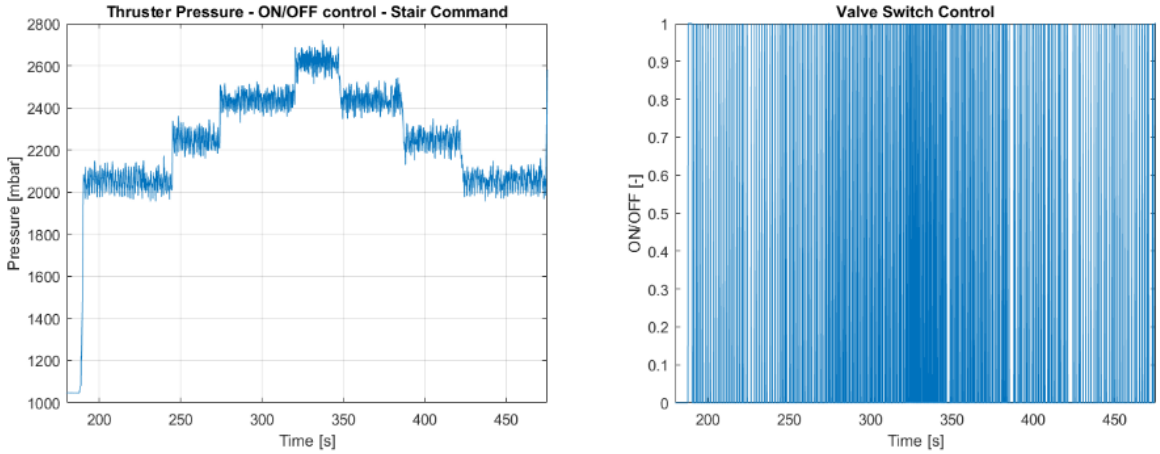

Figure 2.10: Experimental results of a step-wise increase of pressure using SMC [55]

between two measurements and also the interval between two valve activation's. A shorter pressure decay period and more pressure rising periods will decrease the response time for a positive pressure step. Shorter periods between two valve activation's and more flexibility in decay periods will also increase the resolution of the average pressure value and will therefore decrease the deviation to the demanded pressure value. These profits have to be contrasted with the lower measurement quality of the pressure sensors due to a smaller OSR.

2.4. Conclusion

This section will give a summary of the operational envelope and selected control strategy for the VLM micropropulsion system. The control system translates the propulsive demand, the momentum, into an optimal combination of two main control parameters: the chamber temperature and pressure. Two different controller mechanisms ensure that the required conditions are met in the chamber. Both controllers are implemented in the total operational envelope of this propulsion system. In addition there are two different control schemes provided for the experimental phase of this project, to operate the temperature and pressure control systems separately.

The optimal combination of temperature and pressure in the chamber depends on a number of variables. The first important variable is the available power for the heater chip. That power is used in an empirical relation to determine the maximum chamber pressure. The risk of a system failure due to a incomplete vaporization process removes the possibility to operate close to the boundaries. Safety margins are implemented to provide some space for inaccuracies or unexpected behavior. The actual chamber temperature is therefore taken to be smaller than the maximum pressure. That chamber pressure is then used to determine the vaporization temperature of the propellant. Another margin is added above the vaporization temperature to determine the final chamber temperature. The propulsive demand of the OBC is used to determine the thrusting period with IRT and additional empirical relations for the losses in the thruster.

A functional flow diagram of the temperature controller is designed for the experimental phase of the development process. The controller consists of a start-up sequence, main control loop and a data receiving part. The start-up sequence is necessary to initiate the resistance measurements of the heater chip. These measurements need a voltage over and a current flowing through the heater chip. A minimum voltage is applied to determine the temperature of the heater chip. The main control loop reads the data, uses the control mechanism and controls the adjustable power supply. The speed of the main control loop largely depend on the conversion time of the analog-to-digital converter. The measurement function takes 18.61 ms in the default setting to determine the temperature of the heater chip. Faster conversion times are possible with larger SPS rates, but could have a negative impact on the measurement quality. The total processing time could be reduced to 5.47 ms. Section 4 will examine the effect of larger SPS rates on the measurement quality.

A similar functional flow diagram is given for the pressure controller. The advantage of the pressure mea-

surements over the temperature measurements is the necessity of a start-up sequence. The pressure sensor can directly measure the inlet pressure. The main control loop measures the chamber pressure and uses a control mechanism to determine whether the valve should be opened for the minimum spike time of 0.35 ms. It is again the conversion time of the sensor that adds a large measurement delay to the control loop. It takes approximately 42 ms to determine the pressure and temperature at the inlet of the chamber in the default setting. A shorter conversion time could be realized by decreasing the OSR. A smaller OSR has a negative effect on the pressure resolution and decreases the SNR. The decision for the final ideal OSR for this setup can be made once the pressure dynamics of the thruster and achieved accuracy of the adjustable power supply are known. A very high quality of pressure measurements are only valuable when the heating power can be controlled accurately.

The functional flow diagram for the thrusting operation combines the temperature and pressure controllers. The diagram has three main loops: the start-up sequence, the pre-heating sequence and the main control loop. The first two are part of the temperature control loop. The chamber temperature must be sufficient before the pressure can be controlled. The main loop first goes through the pressure steps and activates the solenoid valve. The temperature steps follow once the valve is been activated. The system only steps back to the pressure part when the temperature is still sufficient for a complete vaporization process.

A PID control mechanism is selected to ensure that the chamber temperature approaches the reference temperature. A first order transfer function models the behavior of the heater chip in the control loop. The adjustment of the PID control parameters largely depends on the measurement delay of temperature sensors. Two different implementations of the control parameters have been proposed to examine the difference between the biggest and smallest measurement delay. The rise and settling time of the PID controller is almost proportional with the measurement delay. This shows that a smaller measurement delay will also make the system more efficient, due to the shorter period of overshoot.

The pressure will be controlled using a hybrid design of SMC. The method is successfully tested in a previous project. The control law determines the sliding surface with the current, first derivative and second derivative of the error between the set point and process variable. A negative sign of the sliding surface will open the solenoid valve for its minimum spike time. Experiments showed that the rise time of the pressure is much shorter than the decay time. The valve could therefore open once or less than every loop to reach the demanded pressure levels. The system was able to acquire a resolution of 50 mbar with a measurement delay of 40 ms. A faster control loop will further increase the resolution and performance of this control scheme.

3

Preliminary Design

The design of the control system for the VLM concept of the Delft University of Technology can be divided into two main parts. The first part, about the control strategy, is presented in chapter 2. The second part will be described in this chapter and will explain the development of the hardware for the VLM control system. The hardware consist of a microcontroller (MCU), two adjustable power supplies, a switching circuit and a couple of dedicated sensors.

The MCU translates the propulsive demands of the OBC into an optimal temperature/pressure relation. It uses the solenoid valve and heater chip to control the propulsive performance and the sensor data from the pressure/temperature sensors and the heater chip to monitor the process. A schematic presentation of a VLM micropropulsion system is given in figure 3.1.

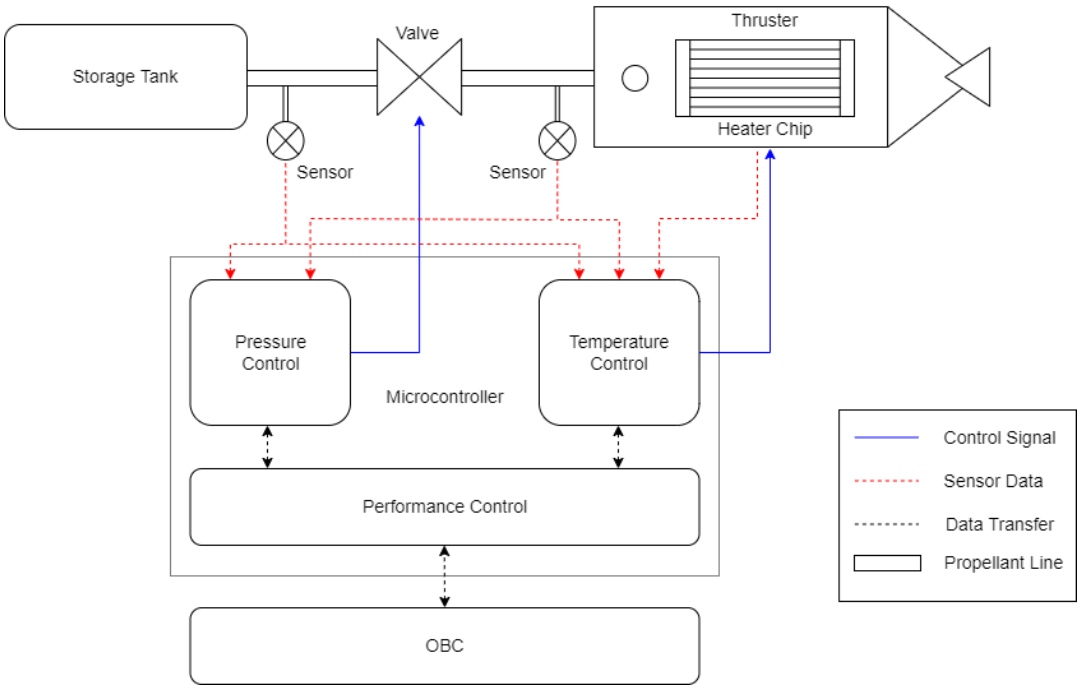

Figure 3.1: Schematic presentation of the VLM propulsion system

The following chapter is dived into four different sections. Section 3.1 presents the design of the temperature control circuit and explains the basic working principle of the heater chip. Section 3.2 presents the solenoid valve and the design of the pressure control circuit. Section 3.3 deals with the selected MCU. The final section of this chapter, section 3.4, will give an overview of the complete system and will shortly examine the power demands of the electronics.

3.1. Temperature Control

The temperature controller hardware consists of three major components: the heater chip, the adjustable power supply and the temperature measurement system. This section will shortly describe the design and operational principle of the heater chip. The heater chip is a result of previous conducted research at the faculty. The amount of power fed to the heater chip regulates the temperature in the chamber. An adjustable power supply converts the input voltage of the EPS to the desired output voltage of the heater chip. That voltage together with the current flowing through the chip should be measured to determine the temperature of the heater chip. The temperature of the heater chip is assumed to be equal to the chamber temperature due to size of the thruster and the used material. These measurements complete the temperature feedback loop.

3.1.1. Heater Chip

The heater chip transforms electrical power into thermal energy for the vaporization process. Two different heater chip designs were developed prior to this project [52]. A schematic presentation of both designs is shown in figure 3.2. Heater 1 contains three sets of 7 lines with a total resistance of 3.40 Ω and heater 2 contains 15 sets of 2 lines with a total resistance of 2.38 Ω. These are the nominal values of the resistances. The actual resistances slightly differ and should be measured for each heater chip.

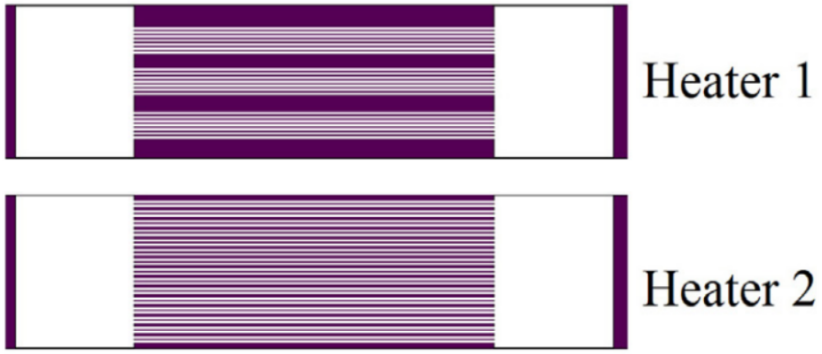

Figure 3.2: Schematic presentation of two different heater chips [52]

Both are made of molybdenum, a metal with a melting point of 2693 °C and a constant resistivity for temperatures up to 700 °C. A constant resistivity together with the zero gradient of temperature assumption enables the possibility to use the heater chip for temperature measurements using equation 3.1.

$$\alpha = \frac{R - R_0}{R_0(T - T_0)} \tag{3.1}$$

Ref. [52] conducted resistance tests to determine the temperature resistance coefficient 'α' of the molybdenum heaters. A thermal camera was used to estimate the temperature of the heater chips over time at different input powers. The temperature coefficient of ten different devices have been determined, resulting in an average value for α of 1.09x10^{-3} °C^{-1}. R_0 is the resistance of the heater chip at a known temperature T_0, R and T are respectively the current resistance and current temperature. Equation 3.1 can be rewritten into equation 3.2 to determine the temperature of the heater chip once the current heater chip resistance is known.

$$T = \frac{R - R_0}{\alpha \cdot R_0} + T_0 \tag{3.2}$$

The graph of equation 3.2 is given in figure 3.3. It is generated assuming the average temperature coefficient of 1.09x10^{-3} °C^{-1}, R_0 equal to 3.4 Ω and T_0 equal to 20 °C. The slope of the graph highlights the sensitivity of the temperature calculations for minor deviations in the resistance measurements. The actual graph for a certain heater chip depends on the starting point (R_0 versus T_0) and its temperature coefficient, this is just an example to show the importance of high quality resistance measurements in the final design. The temperature increases (or decreases) with 0.27 °C per 1 mΩ difference in the heater chip resistance. The temperature measurement system will be described in section 3.1.3, the concept is based on Ohm's law using equation 3.3.

$$R = \frac{V}{I} \tag{3.3}$$

The voltage and current will be measured by the temperature measurement system. The minor temperature difference of 0.27 °C per 1 mΩ seems to be small, but that depends on the accuracy of the measurement system. Ref. [23] showed in figure 1.5 that the maximum chamber pressure is equal to about 0.7 bar for the available peak power. This results in a maximum vaporization temperature of 363.77 K (89.62 °C) using equation 1.8. The actual maximum chamber temperature will be larger, due to the safety margin for the vaporization process and a safety margin for the measurement inaccuracies. A maximum safety margin of 10% is assumed, resulting in a maximum nominal temperature of approximately 400 K. An accuracy of 1.5% seems to be acceptable for this application, which gives a temperature measurement accuracy of ±6 K (or °C). The resistance measurement accuracy is then equal to ±22.22 mΩ.

The final accuracy of the designed temperature measurement system will be examined in the experimental phase of the thesis project. Lets assume that the voltage sensor has an accuracy of ±5 mV and the current sensor has an accuracy of ±5 mA. The actual voltage and current at a certain moment during a propulsive operation are respectively equal to 3.000 V and 0.800 A, which results in a heater chip resistance of 3.750 Ω. The system measures, due to its accuracy, a voltage of 3.005 V and a current of 0.795 A, resulting in a measured resistance of 3.780 Ω. This 30 mΩ difference has a large influence on the determined temperature. The measurement system calculates a temperature that is 8.1 °C higher that the actual temperature of the heater chip. The same is possible for a lower determined temperature, when the voltage is lower and current higher. This example shows that a deviation of ±5 mV and ±5 mA already exceeds the acceptable accuracy of the measurement system. The maximum allowable deviations for the given accuracy of the temperature measurement system are equal to ±3.75 mV and ±3.75 mA. This results in an accuracy of 0.125% for the voltage measurements and an accuracy of 0.47% for the current measurements. The measurement results for both sensors are connected to each other. So if one of the sensors shows better results than mentioned, the other one is allowed to have a poorer measurement accuracy.

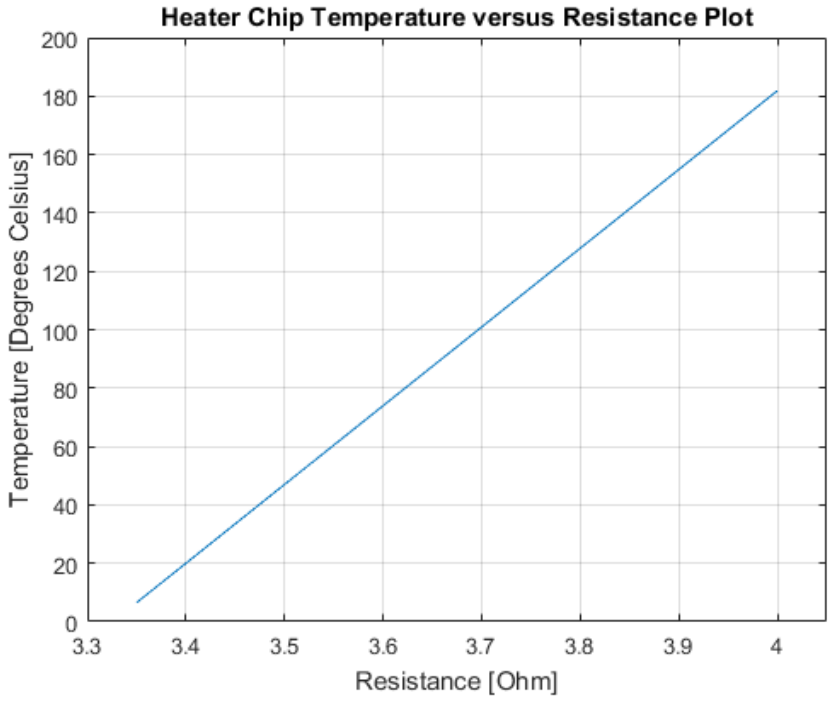

Figure 3.3: Temperature sensitivity for changes in the heater chip resistance measurements

3.1.2. Adjustable Power Supply

An adjustable power supply regulates the temperature of the thruster. The amount of power fed to a resistive heater can be controlled using a DC-DC converter. This could be a buck-, boost- or buck-boost converter, depending on the input and output voltage ranges. The bus DC voltage range of 3-4.1 V of the Delfi-PQ is given by requirement 'PROP-PERF-400' [48]. The output voltage range depend on the required or available amount of power fed to the heater chip. Requirement 'PROP-FUN-100' limits the peak power of the propulsion system to 4 W [48]. The maximum output voltage depends on the resistance value of the heater chip and can be calculated using Ohm's law. This results in a maximum output voltage of 3.69 V for heater 1 (3.4 Ω) and 3.09 V for heater 2 (2.38 Ω). These maximum voltages will be reduced due to the power demands of other parts of the micropropulsion system such as the microcontroller or the solenoid valve. The minimum voltage range depends on the power/pressure relation, lower chamber pressures require less heating power compared to higher chamber pressures. It is difficult to determine the exact minimum output voltage, but it could be lower than the bus voltage. The DC-DC converter should be able to lower the output voltage in relation with the input voltage: Step-Down. In addition, an output voltage above 3 V could be necessary for heater 1 during maximum power operations, the DC-DC converter should also be able to increase the output voltage in relation with the input voltage: Step-Up. A buck-boost configuration of the DC-DC converter is therefore selected for the adjustable power supply of the heater chip.

A buck-boost converter can be designed using some passive components and two switches, but this design process is very time consuming, it is quite difficult to control and possibly hard to reach the desired efficiencies. Another possibility is a COTS converter chip that only requires a small amount of additional components to fine tune its performance. These chips are available different input and output ranges and often reach efficiencies above 90% for their optimal operational range. Important selection parameters for the converter chips are the input and output voltage ranges, the maximum output current, the efficiency versus output current, the efficiency versus input voltage, control interface and the output resolution. The final two are coupled, as the output resolution is limited by the type of communication between the microcontroller and the converter chip. Some devices have integrated an I2C serial interface to communicate with the microcontroller. Their resolution is limited by the amount of reserved bits for their given output voltage range. The MAX77816 [40] high-efficiency buck-boost regulator has, for example, an output range of 2.6-5.14 and reserves 7-bits to select the output value, resulting in an output resolution of 20 mV. This is sufficient for many applications, but limits the ability to control the temperature in the chamber directly in the first design step. The output of other, comparable, converter chips is fixed by a combination of two resistances connected to a feedback pin. Resistance R1 connects the output voltage pin with the feedback pin and resistance R2 connects the feedback pin to the ground. One of these fixed resistances could be replaced by a single or multiple digital potentiometers to regulate the output voltage by changing the resistance. Digital potentiometers can be controlled using I2C or SPI and have a certain amount of taps, depending on the amount of reserved bits. Two or more different digital potentiometers in series increase the number of different resistance values and therefore increase the resolution of the output voltage.

The input voltage range (3-4.1 V) as well as the control interface (resistive) are now clear. The output voltage range should also consist of 3.69V and should have a low minimum. The maximum output current of the system could be calculated using the maximum output voltage and resistance for both heaters, resulting in a maximum output current of 1.30 A. The efficiency depends on the estimated operating range of the adjustable power supply and differs for different input voltages and output currents, with often a maximum value of approximately 90-95%. The selection process is further limited by only considering options that are available on an evaluation board, to simplify the experimental setup.

The EVQ28164-D-00A evaluation board [44] of the MPQ28164 buck-boost converter [43] is selected for this application. Important characteristics of this evaluation board are given in table 3.1. The table shows that it meets the mentioned selection criteria from the previous paragraphs and that is has a good efficiency for the estimated operational range.

The schematic overview of the EVQ28164-D-00A evaluation board from its datasheet [44] is given in figure 3.4. The figure shows an extra advantage of using an evaluation board instead of a single IC. The additional required components and connections are already installed, so the board can be operated directly. There are however two components that should be replaced to add the ability of controlling the output voltage. Resistances R1 (560 kΩ) and/or R2 (100 kΩ) have to be replaced by a new combination of fixed and variable

Parameter	Value	Unit
Input Voltage	1.2 - 5.5	V
Output Voltage	1.5 - 5.0	V
Output Current	0 - 2.0	A
Efficiency (1A, 3.0 V Input)	94	%
Efficiency (1A, 4.1 V Input)	95	%
Control Interface	Resistive	-

Table 3.1: Electrical characteristics of the EVQ28164-D-00A evaluation board [44]

resistances. Equation 3.4 is provided to determine the required combination of both resistances for a given output voltage.

$$R2 = R1 \cdot \frac{V_{FB}}{V_{OUT} - V_{FB}} \tag{3.4}$$

V_{FB} is typically equal to 0.5 V and resistance R1 is recommended to be higher than 300 kΩ and lower than 620 kΩ for an improved efficiency at light loads. The estimated required output voltage is 1.5-3.6 V. This results in a minimum R2/R1 relation of 0.16 (3.6 V) and a maximum R2/R1 relation of 0.5 (1.5 V). Resulting in an operational range of R2 of 48-150 KΩ for R1 equal to 300 kΩ and an operational range of R2 of 99-310 kΩ for R1 equal to 620 kΩ. A bigger range requires larger digital potentiometers or more digital potentiometers in series. Multiple digital potentiometers in series increase the output resolution of the system, but also the complexity in terms of processing time and communication. Through hole potentiometers are available with a maximum of 8-bits and a resistance of 100 kΩ. Two digital potentiometers in series will be potentially able to provide $2^8 \cdot 2^8$ = 65536 different resistive values, which results in a resolution of 0.032 mV for the estimated operational range. This resolution is estimated to be already better than required, but will decrease when the resistive values of the digital potentiometers do not exactly match the required range. Adding a third digital potentiometer will have a minor influence on the performance and will only increase the complexity. R1 equal to 620 kΩ is therefore not possible. The minimum value of R1 of 300 kΩ is selected in combination with a total resistive value of 150 kΩ for R2. R2 will be implemented with a single fixed resistance (40 kΩ) and two digital potentiometers, the MCP4162-103E/P (10 kΩ) [41] and the MCP4261-104E/P (100 kΩ) [42].

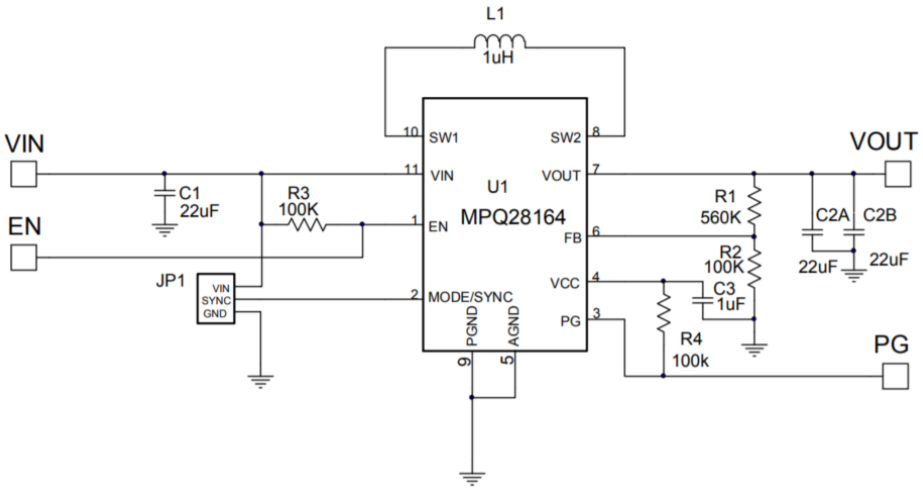

Figure 3.4: Schematic overview of the EVQ28164-D-00A evaluation board [44]

Both digital potentiometers use the SPI interface to communicate with the microcontroller. Equation 3.5 is given in the datasheet of both digital potentiometers [41, 42] and could be used to determine their resistive value for a given tap N.

$$R_{WB} = \frac{R_{AB} N}{256} + R_W \tag{3.5}$$

R_{WB} is the resistive value, R_{AB} is equal to the total resistance and R_W is the wiper resistance, typicaly

equal to 75 Ω. Equation 3.5 gives a step size of 39.06 Ω for the 10 kΩ model and a step size of 390.63 Ω for the 100 kΩ model, giving the combination a theoretical resolution of 39.06 Ω. This results in 2806 different resistive values in the operational range (40-150 kΩ). Small know resistive deviations in one or both of the digital potentiometers could improve the resolution after calibration, but will also increase the complexity in terms of processing time. Calibration could adjust the step size of one of the digital potentiometer. The combination then looses its alignment (e.g. 10 steps 39.06 are equal to a single step of 390.63) and more combined resistive values will be achievable without this alignment, increasing the resolution of the system.

The equation for the output voltage can be derived from equation 3.4 and is given in equation 3.6.

$$V_{out} = V_{FB} \cdot \frac{R_1 + R_2}{R_2} \tag{3.6}$$

With V_{FB} equal to 0.5 V and R_1 equal to 300 kΩ. R_2 is given in equation 3.7 and is determined by the combination of both digital potentiometers with the fixed resistance. The fixed resistance, R_{fixed}, is equal to 40 kΩ.

$$R_2 = R_{step} + R_{Fixed} = 39 \cdot Step + R_{Fixed} \tag{3.7}$$

$Step$ is determined by a combination of tap values N of both digital potentiometers. With N_A equal to the tap of the 10 kΩ digital potentiometer and N_B equal to the tap of the 100 kΩ digital potentiometers. This results in a $Step$ value of:

$$Step = N_A + N_B \cdot 10 \tag{3.8}$$

The final equation for the output voltage follows by inserting equation 3.7 into equation 3.6:

$$V_{out} = 0.5 \cdot \frac{300,000 + 39 \cdot Step + 40,000}{40,000 + 39 \cdot Step} = \frac{170,000 + 19.5 \cdot Step}{40,000 + 39 \cdot Step} \tag{3.9}$$

Figure 3.5 shows the theoretical output voltage of the buck-boost converter for the different combinations of taps for both digital potentiometers, the taps are combined by means of equation 3.8 into the $Step$ variable. The slope of the line is decreasing with an increasing step, meaning that the voltage difference between two steps differs over the operational range. That voltage difference is larger at higher voltages, resulting in a lower resolution when operating in a higher voltage range. The system will have a minimum resolution of 3.65 mV and a maximum resolution of 0.26 mV, with an average resolution of 0.98 mV.

3.1.3. Temperature Measurement System

The chamber temperature is one of the two main control parameters of this micropropulsion system. An optimal relation between the chamber temperature and chamber pressure is essential for an efficient propulsive operation. The nozzle can get clogged when the temperature is too low. This could cause the propellant to leave the chamber through the nozzle before the vaporization process is completed, resulting in a frozen throat. Higher temperatures reduce the mass flow rate and therefore the thrust-to-power ratio [69]. Section 3.1.1 already mentioned that the heater chip could also be used as the temperature sensor for the chamber temperature. The heater chip is not directly in contact with the propellant flow, as the thermal energy is transferred through the silicon structure of the chamber. Silicon is a good thermal conductor and the thrusters are very small, it is possible to assume a zero gradient of temperature [52]. Equation 3.1 needs the current resistance of the heater chip to determine its temperature. The resistance can be derived from the voltage and current using Ohm's law.

The heater chip voltage can be directly measured using the Analog-to-Digital Converter (ADC) of the microcontroller. The ATmega328P microcontroller of the Arduino Uno has a built-in 10-bit ADC to measure voltage between 0 and 5 V [9]. The voltage range suits heater chip voltage range (1.5-3.6 V), but only has 2^{10} (1024) steps from 0 to 5 V. A resolution of 4.88 mV. This resolution is, compared to the resolution of the adjustable power supply (0.80 mV), not sufficient. The resolution is improved by adding an additional low-power ADC, the ADS1115 [65]. This 16-bit, 2^{16} (65536) steps, ADC allows for two differential input measurements with an input range of GND-0.3 V up to VDD+0.3 V (-0.3 - +5.3), resulting in a resolution of 0.085 mV. Measurement data can be collected by the microcontroller using I2C. The same ADC is also used to increase the resolution of the current measurements. The current is measured with the ACS712 (5 A) linear Hall effect sensor. The

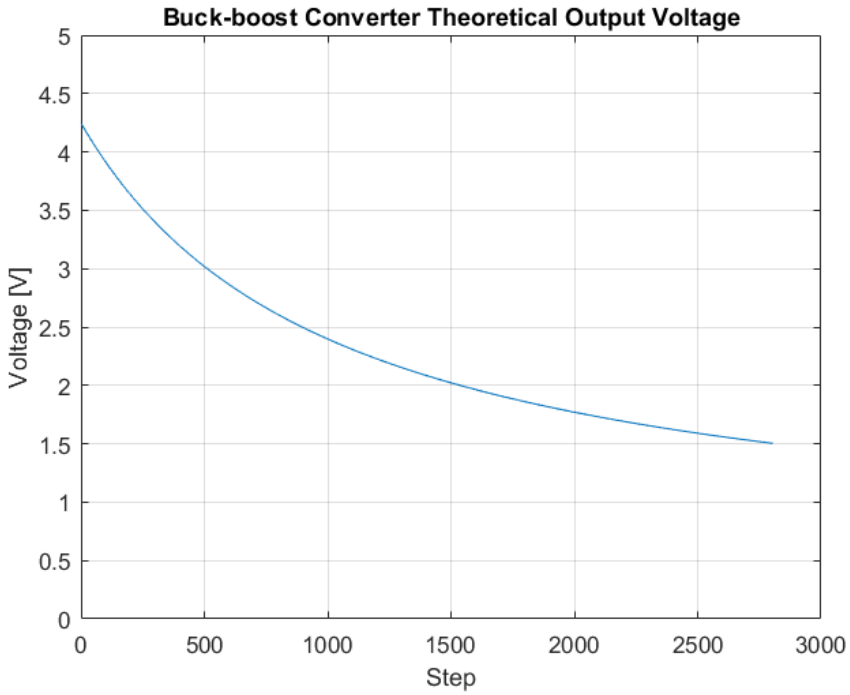

Figure 3.5: Graph of the theoretical output voltage of the buck-boost converter over the input taps of both digital potentiometers

ACS712 converts the current to an analog voltage signal with a sensitivity of 185 mV/A, giving it a combined resolution with the ADC of 0.46 mA. A schematic overview of this measurement system is given in figure 3.6.

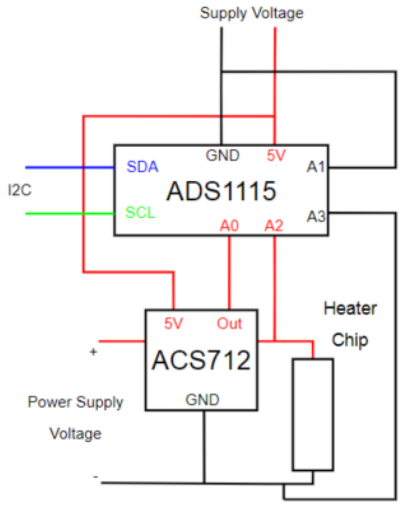

Figure 3.6: Schematic overview of the temperature measurement system with the ADS1115 and the ACS712

A0, A1, A2 and A3 are the analog input signals of the ADS1115. A0 and A1 are used for the differential measurements of the analog signal from the ACS712 and A2 and A3 are used for the differential measurements of the heater chip voltage. This system is theoretically able to sense a minimum resistance value change of 0.085 mΩ due to the resolution of the voltage measurements. Resulting in a temperature resolution of 0.023 °C, using equation 3.1, the 3.4 Ω heater chip and the average value of $1.09\text{x}10^{-3}$ $°C^{-1}$ for α.

The ACS712 Hall effect sensor is placed in series with the heater chip to measure the current through the heater chip. This causes, unlike the parallel voltage sensor, a voltage drop over the heater chip. The size of

the voltage drop depends on the internal conductor of current through Hall effect sensor IC. The internal conductor of the ACS712 has a primary resistance of 1.2 mΩ [3]. The theoretical voltage over the heater chip could be determined with the voltage division equation 3.10. This results in a voltage drop of 1.06 mV, assuming a supply voltage of 3 V and a heater chip resistance of 3.4 Ω. The theoretical losses would then only be 0.93 mW at a supply voltage of 3 V. Negligible compared to its estimated power usage of approximately 50 mW.

$$V_{heater} = \frac{R_{heater}}{R_{heater} + R_{ACS712}} \cdot V_{powersupply} \tag{3.10}$$

3.2. Pressure Control

The chamber pressure is a critical variable for the propulsive operation of the thruster. Propellant is fed by the liquid feed and storage system to the pressure control valve at the inlet of the chamber. The valve allows propellant into the chamber after a signal of the MCU. The MCU controls a switching circuit that connects and disconnects the valve from the adjustable power supply. The adjustable power supply transforms the voltage level of the EPS into the voltage level required by the valve. Two pressure sensors are necessary to fulfil the need of the control system. A pressure sensor with a large measurement range for the storage pressure and a highly accurate sensor to measure the pressure at the inlet of the chamber.

3.2.1. Solenoid Valve

The micro-valve controls the pressure in the chamber. Previous work selected a VHS micro-valve from the Lee Company [49]. Valves from the VHS series are normally closed, high speed, ON/OFF solenoid valves with different operating conditions and sealing materials. The INKX0511400A is selected from the VHS series [33], a schematic overview of the solenoid valve is given in figure 3.7. The selected valve is mentioned in this report because of its important electrical requirements for the design of the control system form this project. Verification of the selected valve is out of the scope of this project, it is therefore adapted from previous work.

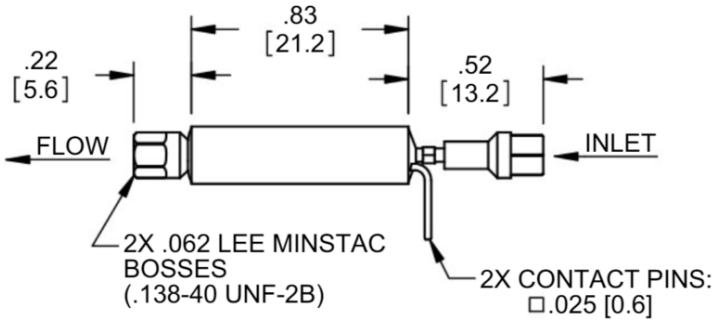

Figure 3.7: Schematic overview of the INKX0511400A solenoid valve [33]

The INKX0511400A requires a spike voltage of 12 V for at least 0.35 ms to open and after that a hold voltage of 1.6-2.3 V to keep the valve open. The implementation of this valve into the pressure control system determines the design of the required power supply. Normal, spike-and-hold, operation requires two DC-DC converters and a set of switches to control the activation and duration of the spike and hold parts. Ref. [55] proposed and tested a modified Sliding Mode Control (SMC) scheme for the VLM thruster of this project. This control scheme only requires an ON/OFF control signal for the minimum opening time of the solenoid valve, removing the hold requirements and simplifying the power supply design. The SMC control approach has been discussed in section 2. The next paragraph will show both power supply designs, to explain their differences and weight in the selection process of the ideal pressure control scheme.

3.2.2. Power Supply

The power supply for the solenoid valve should be able to convert an input voltage of 3-4.1 V into the desired spike and hold voltages. The regular spike-and-hold operation requires a spike voltage of at least 12 V and a hold voltage of at least 1.6 V. A boost converter is necessary to increase the input voltage level and a buck converter is necessary to decrease the input voltage level. A schematic overview of this power supply is given

in figure 3.8.

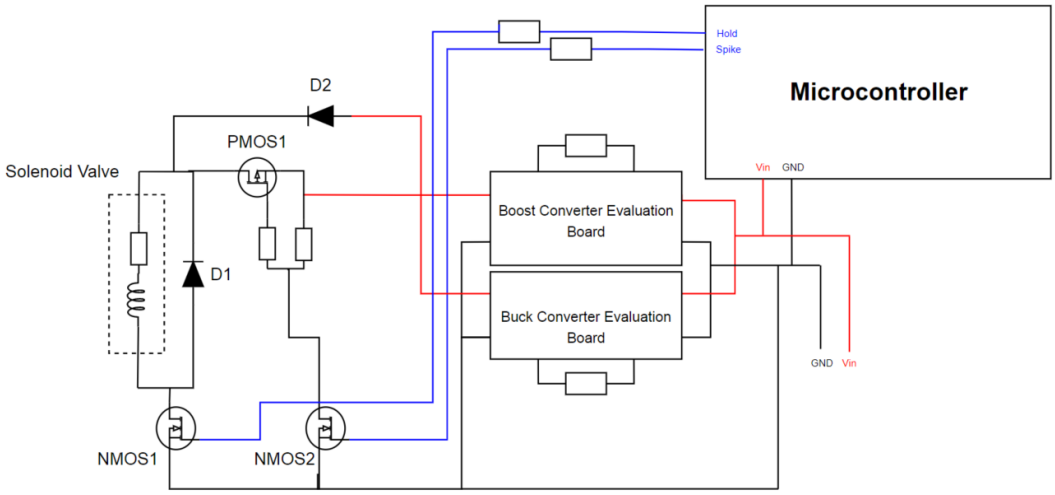

Figure 3.8: Schematic overview of the power supply for the spike-and-hold operation

The operational principle of the switching circuit is based on the ability to connect and disconnect both DC-DC converters from the solenoid valve. A signal diagram for the spike-and-hold control circuit is given in figure 3.9. NMOS1 controls the current flow through the valve and should be activated during the spike and hold periods. NMOS2 activates PMOS1 by pulling the gate voltage of PMOS1 to the ground, connecting the boost converter to the valve. The control signals spike and hold from the microcontroller must be both 'HIGH' to open the valve. The spike signal can be changed into 'LOW' after the minimum spike time of the valve. The valve will not close until the hold signal is also changed into 'LOW'. The diode (D1) parallel to the valve dissipates the coil's magnetic energy, protecting the transistor from an inductive voltage spike [34]. Diode D2 is a reverse protection diode, to ensure that the buck converter is only able to apply a positive voltage to the solenoid valve.

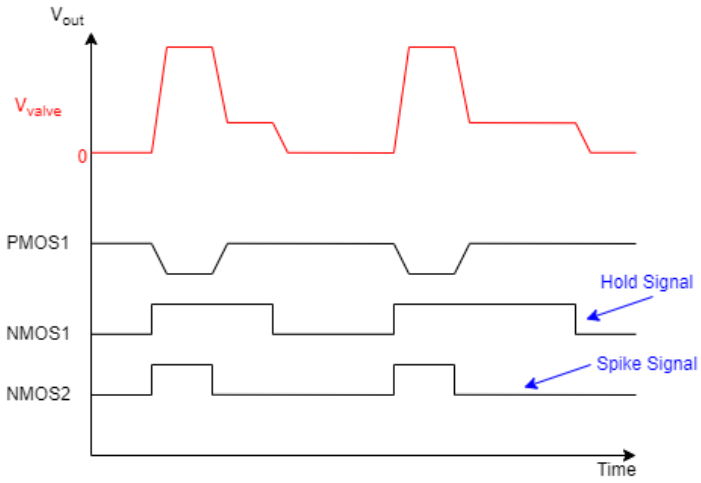

Figure 3.9: Signal diagram of the spike-and-hold operation

Section 3.2.1 already mentioned the possibility to implement a SMC scheme to control the pressure in the chamber, removing the hold requirements and simplifying the power supply design. A schematic overview of this spike circuit is given in figure 3.10. The operational principle of the spike circuit is comparable with the operational principle of the spike-and-hold circuit from figure 3.8. A signal diagram for the spike control circuit is given in figure 3.11. A 'HIGH' spike control signal from the microcontroller activates the NPN

transistor to pull the gate voltage of the PMOS to zero, connecting the boost converter to the valve. This implementation also slightly simplifies the controller program of the microcontroller, because the electronics only require a single control signal. The simplified circuit for the spike operation is selected for the remainder of this project, the SMC scheme and experimental results will be examined in chapters 2 and 4, respectively.

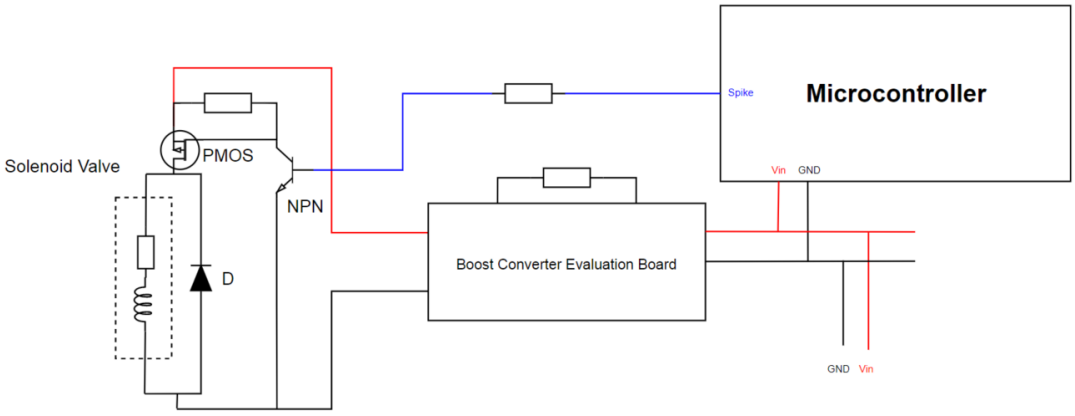

Figure 3.10: Schematic overview of the power supply for the spike operation

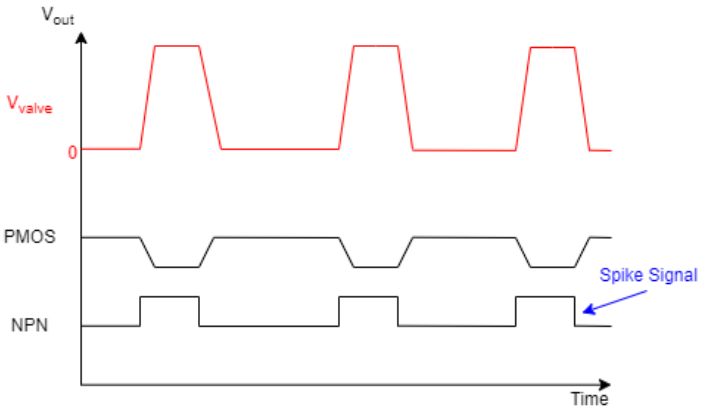

Figure 3.11: Signal diagram of the spike operation

The selection process of the boost converter is comparable with the selection process of the converter for the temperature control part. Important selection criteria are the input voltage range, desired outputs, output current, their efficiency and control interface. In addition, its important that the converter is available on an evaluation board to simplify the design process. The electrical characteristics of the selected converter are given in table 3.2. The output voltage control interface of the converter is resistive and can be regulated by changing the resistive combination connected to the feedback pin. Varying resistances using digital potentiometers are neglected because a constant output voltage is required during operation.

Converter:	**EV3428A-L-00A**	
Parameter	**Value**	**Unit**
Input Voltage	3 - 20	V
Output Voltage	V_{in} - 22	V
Output Current	19	A
Efficiency (1A, 3.3 V Input)	89	%
Control Interface	Resistive	-

Table 3.2: Electrical characteristics of the EVQ3428A-L-00A [45] evaluation board

The output voltage of of the boost converter (EV3428A-L-00A) is determined with equation 3.4, with V_{FB} equal to 1.225 V and resistance R1 equal to 300 kΩ. Figure 3.12 gives a schematic overview of the evaluation board. The output control resistors are connected to the feedback pin 'FB' of the IC. A fixed resistance value of 31 kΩ for R2 will give an output voltage of 13.08 V. A safety margin above 12 V is added to ensure the required voltage level of the solenoid valve after the voltage drop of the MOSFET.

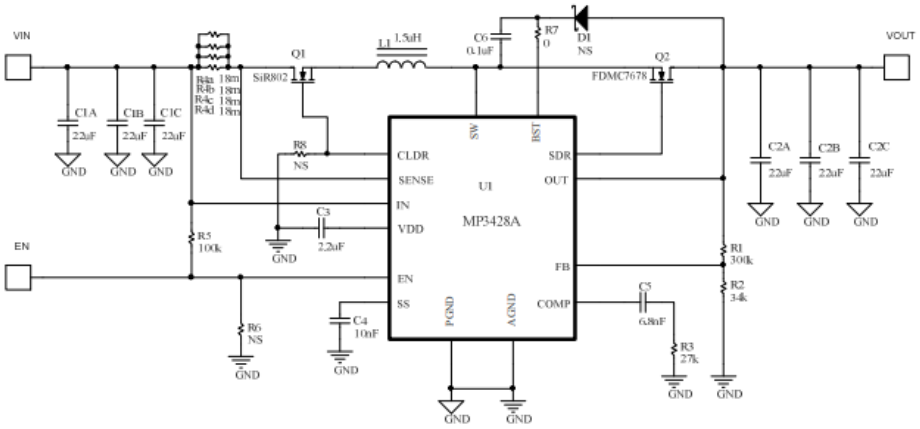

Figure 3.12: Schematic overview of the EV3428A-L-00A evaluation board [45]

3.2.3. Pressure Sensors

Pressure sensors determine the pressure at different positions in this micropropulsion system. The sensors are ideally placed at four different positions to measure the storage pressure, inlet pressure, chamber pressure and exit pressure, but at least the pressure in the chamber is essential to complete the feedback control system. An additional sensor connected to the storage tank is also very useful to monitor the pressure in the tank and to predict next performances of the system. The chamber and exit pressures are very difficult to measure due to the design and size of the system. For pressures measured very close to the chamber it is safe to assume that they are equal to the chamber pressure [52]. The measurements of a pressure sensor at the inlet section of the chamber are therefore used to determine the pressure in the chamber [54]. The exit pressure can thereafter be calculated using chamber pressure and nozzle area ratio with equation 1.2.

Previous projects for the same propulsion system proposed the pressure sensor series from TE Connectivity MS5837 [49, 52] and the TE Connectivity MS5803 [55]. Both series are also able to measure temperature and contain sensors with different operating ranges and resolutions (e.q. MS5837 [60–62] or MS5803 [58, 59]). The final selection procedure between these or other sensor series is out of the scope of this project, mainly due to their different shapes and sizes. There are, however, a number of performance parameters important to consider. The MS5837 series is selected to simplify the trade-off between the different models, the same trade-off is applicable for different sensor series and also to compare the different series with each other.

Table 3.3 shows the performance characteristics of three different sensors from the TE Connectivity MS5837 series. The input power requirements are equal and are therefore removed from the table. Each sensor of this series has an I^2C interface to transfer its measurement data to the microcontroller. The device address of the I^2C interface directly adds an important constraint to the selection process. The I^2C interface requires an unique slave address for each connected device and each model from this series contains the same I^2C slave address. This problem could be solved using an I^2C multiplexer, allowing the same addresses on different channels of the multiplexer [37]. An additional multiplexer is an extra component and increase the complexity of the system. Another possibility is to select two different models, e.g. the MS5837-07BA for the storage pressure and the MS5837-02BA for the inlet pressure. For now it seems to be more obvious to select two different models and accept their differences in performance to keep the design as simple as possible. Additional research should show whether the performance differences are indeed acceptable, selecting two models from different series might also solve the problem.

The main difference between the three models from table 3.3 is their operating pressure range. Section

Sensor: **Parameter**	**MS5837-30BA** **Value**	**MS5837-07BA** **Value**	**MS5837-02BA** **Value**	**Unit**
Operating Pressure Range	0 - 30	0 - 7	0.3 - 1.2	bar
Operating Temperature Range	-20 - +85	-20 - +85	-20 - +85	°C
Resolution RMS (OSR 8192)	0.20	0.031	0.016	mbar
Absolute Accuracy (0 - +45°C, 0 - 20 bar)	-100 - +100	-	-	mbar
Relative Accuracy (0 - +60 °C, 0 - 5 bar)	-	-30 - +30	-	mbar
Relative Accuracy (-20 - +85 °C, 0.3 - 1.1 bar)	-	-15 - +15	-4 - + 4	mbar
Resolution RMS (OSR 8192)	0.0022	0.002	0.002	°C
Absolute Accuracy (-20 - +85°C)	-4 - +4	-4 - +4	-	°C
Relative Accuracy (-20 - +85°C)	-	-	-2 - +2	°C

Table 3.3: Performance characteristics of the MS5837-30BA [62], the MS5837-07BA [61] and the MS5837-02BA [60] pressure sensors

1.1.4 explained that the maximum chamber pressure is limited to 0.7 bar due to the peak power requirement of 4 W. A minimum chamber pressure is not given, but figure 1.5 showed experimental results below 0.3 bar. The system still requires approximately 2.5 W of heating power at a chamber pressure of 0.3 bar. It is likely that sometimes less power is available compared to the mentioned peak power and the system also consumes power with the control electronics, solenoid valve and DC-DC converters. Operating below 0.3 bar is therefore plausible. The exact relative accuracy of the MS5837-02BA for operating pressures smaller than 0.3 bar is not provided by the datasheet and therefore not presented in the table. There is however a graph available in the datasheet that gives an indication of the performance at lower pressures. The graph is given in figure 3.13. The maximum error is visible for a measurement temperature of -20 °C, but that is out of the scope of this application. The temperature at the inlet section should at least be above 0 °C to allow liquid water to enter the chamber. The maximum relative error for temperatures around and above 25 °C is approximately equal to 1 mbar. These results are very good compared to the MS5837-30BA and the MS5837-07BA, and are also within the given performance of table 3.3. The MS5837-02BA is therefore selected to measure the inlet pressure of the chamber.

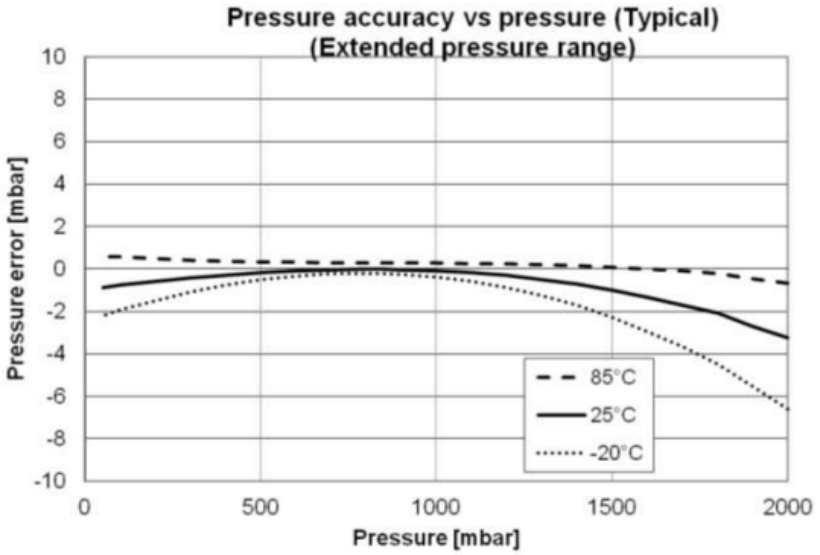

Figure 3.13: Relative pressure error versus pressure and temperature for the MS5837-02BA [60]

The maximum storage pressure of the plastic tube (storage tank of the Delfi-PQ propulsion systems) is 10 bar [48], but miniaturized spacecraft are often limited due to the secondary payload launch restrictions. Ref. [16] mentioned that the internal storage pressure of PocketQubes is sometimes limited to 1.2 bar. In that final case, it would be more preferable to select a pressure sensor with a lower range for both the storage and inlet pressure measurements as the resolution and accuracy decreases with a larger operating pressure

range. At this stage of the development process it is impossible to estimate the final storage pressure of the flight prototype. The MS5837-07BA is always preferred when the storage pressure is within its measurement range. MS5837-30BA should be only selected for storage pressures above 7 bar. A schematic overview of the I^2C and power interface between the pressure sensors and the microcontroller is given in figure 3.14.

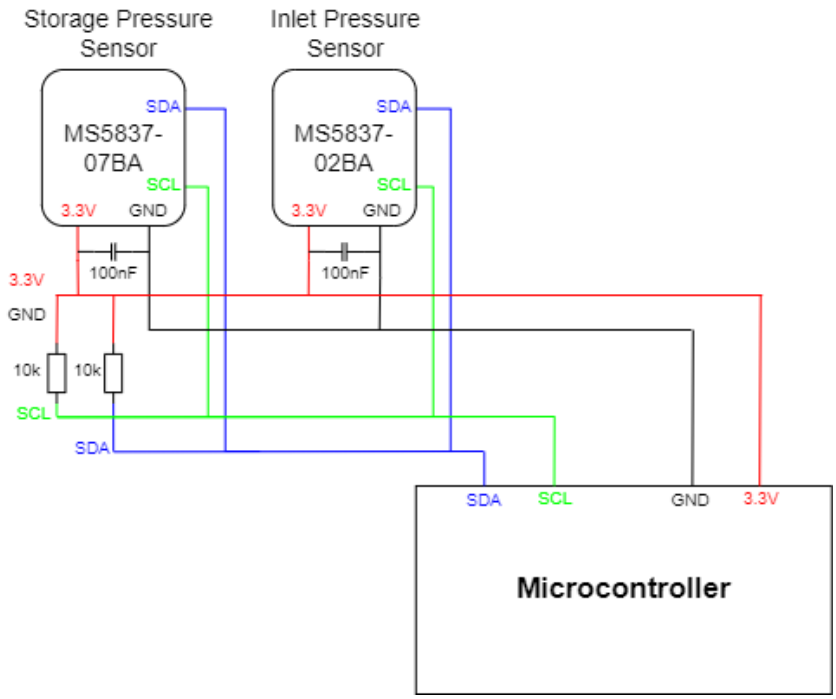

Figure 3.14: Schematic overview of interface between the storage and inlet pressure sensors and the microcontroller

3.3. Microcontroller

The microcontroller is the on-board mini computer of the propulsion system. The quality of the temperature and pressure control electronics also partly depends on the performance of the microcontroller, it is essentially the center of the control electronics for this micropropulsion system. The selection process for the best suited microcontroller is important, but also quite comprehensive. A large amount of different microcontroller units (MCU) is available with different properties for various applications. Important characteristics like power consumption, processing power, operational range, hardware interface and software architecture differ for every project. Another important factor, especially for a breadboard configured experimental system, is accessibility in terms of hardware and software.

The demand for an accessible MCU board is leading in the choice for the Arduino UNO [5]. The Arduino Uno is a widely applicable development board with a clock speed of 16 MHz, 32 KB flash memory, 6 analog input pins and 14 digital I/O pins. The board has three communication protocols: SPI, I2C and UART, and is based on the ATmega328P MCU [9]. The ATmega328P is a low power 8-bit microcontroller. The system operates with programmable Arduino software which supports the 'C' and 'C++' programming languages. The development board is shown in figure 3.15. The Arduino Uno will be powered by a USB connection with a regular computer, the same connection also supports the serial interface between the board and the Arduino Integrated Development Environment (IDE). It also works on a external power supply with a recommended voltage of 7-12 V [5].

Figure 3.15: Top view of the Arduino Uno development board [5]

3.4. Final Design

Figure 3.16 shows a schematic overview of the final control electronics circuit. The right side of the figure is solely used to control the temperature in the chamber with adjustable power supply and voltage and current sensors. The left side consists of the solenoid valve control circuit and both pressure sensors. These pressure sensors are also able to measure the inlet and storage temperature, of which the latter one is especially important to prevent the liquid propellant from freezing. The figure shows the different communication lines between the MCU and the additional components. All sensors operate with the I2C interface, the actuators use a digital I/O pin (solenoid valve) and SPI (digital potentiometers, heater chip).

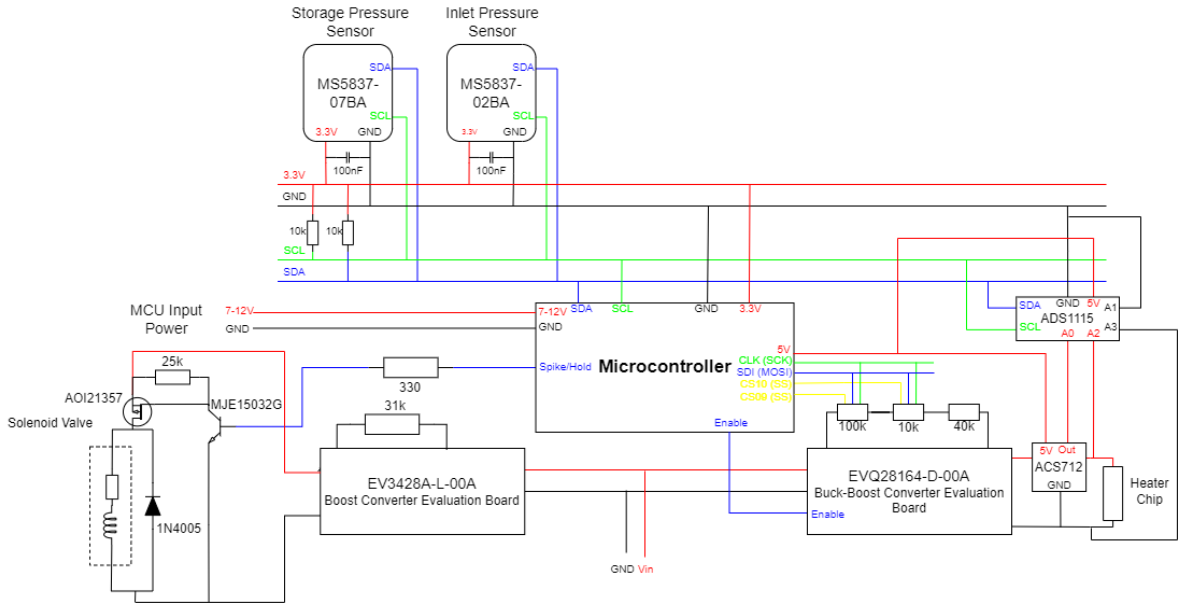

Figure 3.16: Schematic overview of the final control electronics design

The MCU requires a different input voltage level compared to both DC-DC converters. The DC-DC converters are selected to operate with the varying voltage levels of a PocketQube (3-4.1 V), but the selected development board needs at least 7 V [5]. This will not be a major issue during the experimental phase of the project, because of the supplied power through the USB connection. It is also not a direct challenge for the first flight prototype due to the 2.7 - 5.5 V operating voltage range of the ATmega328P [9].

3.4.1. Power Demands

Miniaturized spacecraft like the PocketQube have to be very careful with the dissipation of electric energy. The size of the spacecraft limits the size of the solar panels and therefore the amount of energy produced in orbit. Only 4 W is available for the micropropulsion system in the Delfi-PQ PocketQube. An efficient control system ensures that a large part of that power will be actually used for the vaporization process and to open the solenoid valve. This section will shortly examine the theoretical power usage of the electronic components and the conversion losses of the DC-DC converters. The power demands of the components are summarized in table 3.4.

A relatively small part of the maximum peak power is used to supply the remaining components with the power they need to perform their specific operations. Only the ACS712 requires a bit more power than the other components. The sensor requires additional power for the differential amplifier, for the amplification of the small Hall effect voltage. The table is not complete as the power dissipated in the diode and switching circuit is not been taken into account. Their influence on the final energy balance of the system is estimated to be negligible compared to the demands of the solenoid valve and heater chip. It is not the goal of this work to determine the exact amount of energy that is available for the vaporization process. Only a rough estimation will be sufficient to determine the operational range of the micropropulsion system.

The amount of energy available for the vaporization process depends on the available battery power, en-

Component	Type	Value	Unit
EV3428A-L-00A	Quiescent Current (200 μA, 3.3 V)	0.66	mW
ACS712	Supply Power	50	mW
ADS1115	Supply Power	0.9	mW
MCP4162-103E	Supply Power	2.25	mW
MCP4162-104E	Supply Power	2.25	mW
MS5837-07BA	Supply Power	4.125	mW
MS5837-02BA	Supply Power	4.125	mW
ATmega328P	Supply Power	4.5	mW
	Total Operating Power	**68.81**	**mW**

Table 3.4: Summary of the power usage of the electronic components of this micropropulsion control system

ergy used by the components, energy used by the valve controller and the conversion efficiency of the buck-boost converter. Chapter 2 examined the possibility to decrease the sampling time of both measurement systems in sections 2.2.1 and 2.2.2. This could have a positive effect on the accuracy of the control system, but will also decrease the transient time between two spikes. This affects the available heater chip power negatively. The amount of energy required by the valve in the same period of time increases, because the control system could demand for two spikes in that same period of time. Different sampling times increase the complexity of the energy calculations. A example will be given below. The amount of energy required for a single spike is given in equation 3.11.

$$\begin{aligned} P_{spike} &= \frac{V_{spike}^2}{R_{valve}} = \frac{13.08^2}{10.6} = 16.14\,W \\ P_{in,boost} &= \frac{P_{spike}}{\eta_{DCDC}} = \frac{16.14}{0.85} = 18.99\,W \\ E_{spike} &= \frac{P_{in,boost} \cdot t_{min}}{3600} = \frac{18.99 \cdot 350 * 10^{-6}}{3600} = 1.85\,\mu Wh \end{aligned} \tag{3.11}$$

Ref. [55] performed its experiments for the ideal control mechanism with a sampling time of 40 ms. Equation 3.12 determines the available heater power using the sampling time of Ref. [55].

$$\begin{aligned} E_{peak} &= \frac{P_{peak} \cdot t_s}{3600} = \frac{4 \cdot 0.04}{3600} = 44.44\,\mu Wh \\ E_{components} &= \frac{P_{components} \cdot t_s}{3600} = \frac{0.068 \cdot 0.04}{3600} = 0.76\,\mu Wh \\ E_{quiescent} &= \frac{P_{quiescent} \cdot (t_s - t_{spike})}{3600} = \frac{0.66 * 10^{-3} \cdot 0.04}{3600} = 0.0073\,\mu Wh \\ E_{temp} &= E_{peak} - E_{spike} - E_{components} - E_{quiescent} = 41.83\,\mu Wh \\ P_{temp} &= \frac{E_{temp} \cdot 3600}{t_s} = \frac{41.83 \cdot 3600}{0.04} = 3.77\,W \\ P_{heater} &= P_{temp} \cdot \eta_{DCDC} = 3.77 \cdot 0.94 = 3.54\,W \end{aligned} \tag{3.12}$$

The sampling time could be reduced to approximately 10 ms for a control loop with temperature and pressure measurements. The available heater chip power is determined in equation 3.13.

$$\begin{aligned} E_{peak} &= \frac{P_{peak} \cdot t_s}{3600} = \frac{4 \cdot 0.01}{3600} = 11.11\,\mu Wh \\ E_{components} &= \frac{P_{components} \cdot t_s}{3600} = \frac{0.068 \cdot 0.01}{3600} = 0.19\,\mu Wh \\ E_{quiescent} &= \frac{P_{quiescent} \cdot (t_s - t_{spike})}{3600} = \frac{0.66 * 10^{-3} \cdot 0.01}{3600} = 0.0017\,\mu Wh \\ E_{temp} &= E_{peak} - E_{spike} - E_{components} - E_{quiescent} = 9.07\,\mu Wh \\ P_{temp} &= \frac{E_{temp} \cdot 3600}{t_s} = \frac{41.83 \cdot 3600}{0.01} = 3.27\,W \\ P_{heater} &= P_{temp} \cdot \eta_{DCDC} = 3.27 \cdot 0.94 = 3.07\,W \end{aligned} \tag{3.13}$$

These results show a decrease of almost 20% in heater chip power for a shorter sampling time, but that is only in the extreme case when the valve have to be activated in two successive control loops. Ref. [55] showed that the transient time between two spikes depend on the demanded chamber pressure and could be much larger than the sampling time of 10 ms. These energy limitations have to be considered in the trade-off between the ideal sampling time, measurement quality and performance of the micropropulsion system. A shorter transient time between two spikes decreases the available heater power. Less heating power limits the maximum chamber pressure, shown in figure 1.5, and a smaller chamber pressure increases the transient time between two consecutive spikes. This circle of consequences have to be examined in future projects and will be included in the recommendation chapter (6) of this thesis.

4

Experimental Characterization

This chapter will describe the experimental setup, procedure and results to examine the performance of the proposed system and strategy. Section 4.1 explains the experimental setup with the equipment that is generally used in every experiment. Section 4.2 presents the experimental procedure and the results of the measurements conducted to assess the quality of the adjustable power supply and the resistance measurements. The experiments conducted to assess the quality of the solenoid valve control circuit are given in section 4.3. Finally, section 4.4 summarizes the results and present the conclusions on the experimental part of this project.

4.1. Experimental Setup

The setup for the experiments conducted in this chapter will be described in this section. A list of the equipment and components is given in table 4.1. An image of the electronics of the designed control system that is used for the experiments of this chapter is given in figure 4.1.

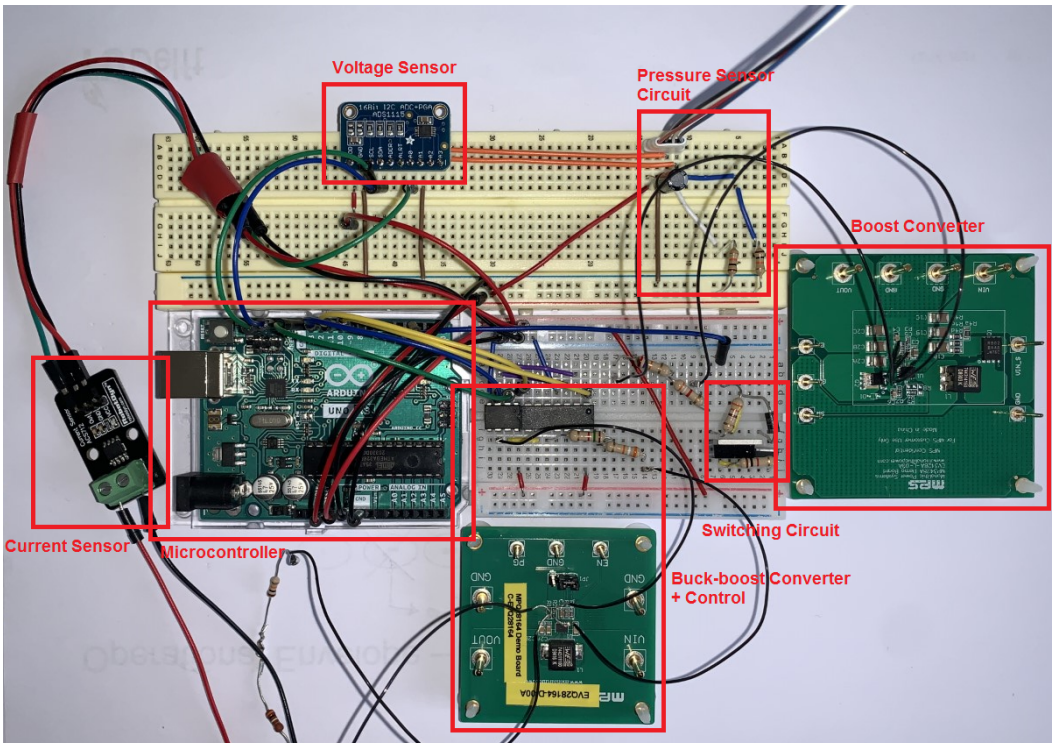

Figure 4.1: Final design of the hardware from figure 3.16

Figure 4.1 shows two different items from table 4.1. The first one is the microcontroller that is used for this project, the Arduino Uno. The figures shows the connections between the microcontroller and the additional components of the control system. The additional components are the second item from table 4.1, components from the temperature and pressure control circuit. A schematic overview of that circuit is given in figure 3.16. The current sensor, voltage sensor, buck-boost converter and its control circuit are used to control the temperature of the thruster. The pressure sensor circuit, boost converter and switching circuit control the pressure. The operational performance of these components is examined in this chapter using the devices mentioned in table 4.1. The setup for each experiment is different and is therefore not provided at the start of this chapter. A basic schematic of the connections between the components and devices is given at the start of each experiment.

Item Name	Description
Agilent 3631A DC Power Supply	The power supply is used to act as the EPS of the satellite. It supplies power to both DC-DC converters. In addition, it is also used calibrate the sensors and test their performance.
Tektronix TDS2014B Oscilloscope	The oscilloscope is used to monitor the voltage over the load in every experiment. It is connected to a laptop to conduct high resolution voltage measurements of 2500 samples.
Keithley Model 199 System DMM Scanner	The Model 199 is a autoranging, high resolution, digital multimeter. It is used in the experiments to determine resistive value of different resistances, like the like the solenoid valve and the load that replaces the heater chip.
FLIR AX-5 Thermal Camera	The AX-5 is a high quality, compact thermal camera It is used to verify the application of the temperature control circuit and to examine the thermal dynamics of the heater chip.
VLM Thruster & interface	A VLM thruster from previous projects is used to test the quality of the temperature control system. The interface is necessary to connect the heater chip with the control electronics, feed system and pressure sensor.
Solenoid Valve INKX0511400A	The solenoid valve is a 2-way, high speed valve that requires a spike voltage of 12 V and a hold voltage of 1.6 V. The valve has a equivalent series resistance of 10.6 Ω. It is used to verify the operational principle of the pressure control circuit and to determine its functional requirements.
Arduino Uno	The Arduino Uno is the MCU of the design. It is used to control the digital potentiometers and switching circuit. In addition, it will be also to collect data from the sensors.
Temperature and Pressure Control Circuit	The control circuit is given in figure 3.16. It is the main design of the project and is able to control the pressure and temperature with directions of the MCU.
Load	A load of 3.3 Ω is used to replace the vulnerable heater chip during the experiments. It is a high power cement resistor with a constant resistive value.
Wires	Wires are used to connect designed circuit to the additional equipment and components.
Laptop	The laptop is used to control the MCU (Arduino Uno), to collect data from the oscilloscope and is used to make notes of unexpected behavior and data from the power supply and multimeter.

Table 4.1: Equipment used for the conducted experiments of the thesis project

4.2. Temperature Control

Temperature is the first main control parameter of the VLM concept. The demanded chamber temperature depends on the vaporization temperature of the propellant plus a certain safety margin. The safety margin is based on the accuracy of the adjustable power supply, quality of the temperature measurements and the pressure control system. The first two variables will be assessed in this section. Starting with the output accuracy and efficiency of the adjustable power supply. The temperature measurement system will be investigated thereafter. A small safety margin is only possible with an accurate measurement system, because it should be at least larger than the maximum measurement error. That is the only way to measure a certain temperature and know that the actual temperature is higher than the required chamber temperature. A larger safety margin will also increase the maximum gap between the required, reference temperature and the actual temperature. Higher temperatures will decrease the mass flow rate and therefore the produced thrust and will increase the power lost into the environment. An accurate temperature control system will lead to a more efficient and better performing propulsion system.

4.2.1. Heater Chip Control

The amount of power fed to the heater chip is controlled by the adjustable power supply from section 3.1.2. The resistive value of two digital potentiometers regulates the output voltage of a buck-boost DC-DC converter. The power fed to the heater chip could then be determined by that controlled voltage and its current resistive value. This section will assess the actual performance of this adjustable power supply and will compare it to the theoretical performance proposed in section 3.1.2. The two main factors that define the quality of the system will be covered in the next two paragraphs.

Output Accuracy

The ability to supply the exact amount of power to the heater chip depends on the accuracy of the adjustable power supply. Section 3.1.2 already explained the theory behind the control mechanism of the adjustable power supply. This resulted in equation 3.9 and figure 3.5, providing the theoretical output voltage for a given combination of taps for both digital potentiometers. A schematic overview of the measurement setup that is used to calibrate the output voltage of the buck-boost converter is given in figure 4.2. The power is supplied by the Agilent E3631A DC power supply [2] and the voltage is measured with the Tektronix TDS2014B oscilloscope [63].

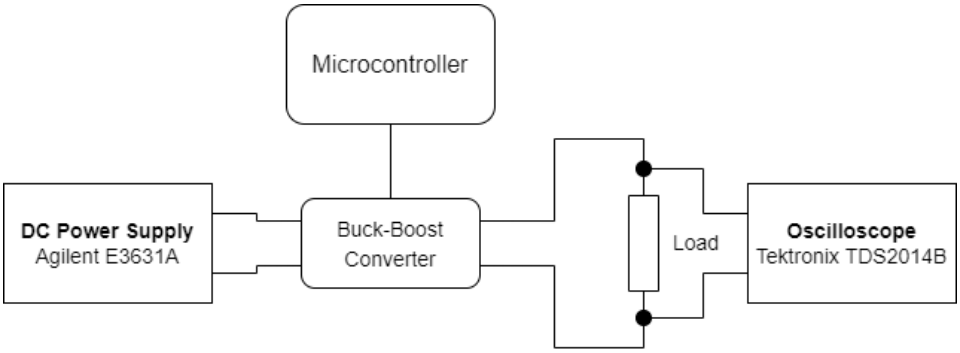

Figure 4.2: Schematic overview of the measurement setup for the calibration of the buck-boost converter

Figure 4.3 shows a comparison between the theoretical output voltage and the real output voltage. The blue dots are the conducted measurements for different digital potentiometers steps. The average difference between the theoretical output voltage and the measured output voltage data points is 24.8 mV with a maximum of 40.2 mV.

Figure 4.3 showed that the theoretical calculated output voltage approached the actual measured output voltage, but the differences are still too large. These differences could be caused by a number of small deviations in the selected components. The feedback voltage is mentioned to be typically 0.5 V [44], but could differ with a maximum of 1.5% [43]. The step size of the combination of both digital potentiometers is also a bit smaller than the theoretical value, because the total resistive range is 0.19-104.13 kΩ instead of 110 kΩ.

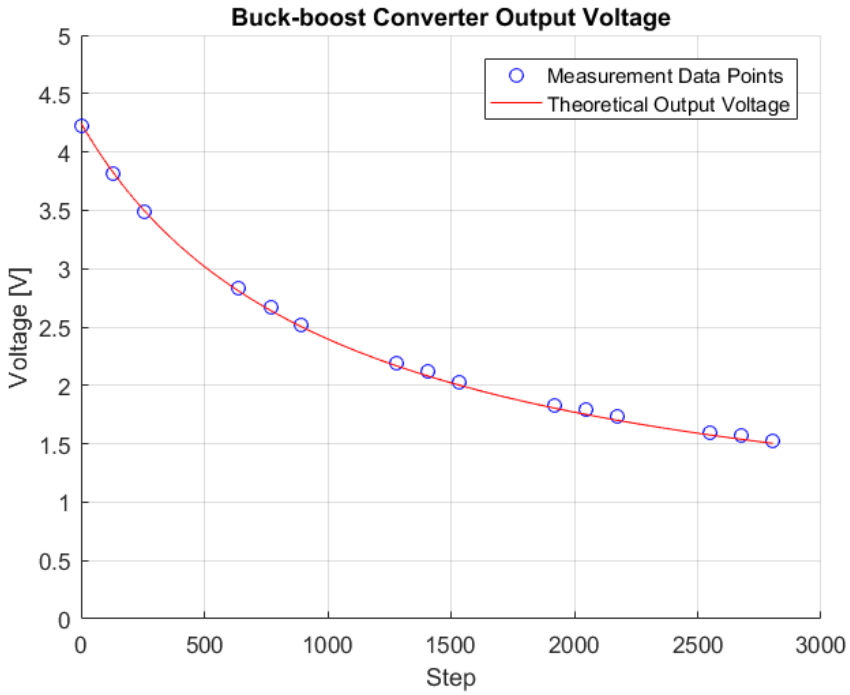

Figure 4.3: Theoretical versus measured DC-DC converter output voltage

Resulting in a resistive step size of ±37 Ω compared to the given theoretical value of ±37 Ω [41, 42]. The additionally added resistances are also not exactly equal to the proposed resistances of section 3.1.2.

Looking for the optimal combination of the above mentioned deviations is a difficult and time consuming task and is therefore out of the scope of this thesis project. An easier way to an equation with an improved accuracy is provided by the curve fitting tool of Matlab. The measured data points are used to determine the curve fitted equation 4.1.

$$V_{out,CF} = \frac{0.5082 \cdot Step + 4505}{Step + 1069} \tag{4.1}$$

The curve fitted equation has a coefficient of determination, R-squared, equal to 99.9%. Figure 4.4 shows the curve fitted line with the measured data points. The average difference between the curve fitted output voltage and the measured output voltage data points is 5.9 mV with a maximum of 13.0 mV.

The characterization of the optimal converter model for the final flight model could be further improved by adding more data points to the curve fitting tool, but these results seem to be sufficient for the current development level of the control system. Especially considering the current bread board model that is still being assembled and disassembled, requiring it to be re-calibrated before every new experiment.

The optimal converter model converts the desired output voltage into the input for both digital potentiometers. This conversion step determines the accuracy of the output, but does have an influence on the precision of the output voltage. Figure 4.5 shows the maximum output voltage difference, deviation and precision of the buck-boost converter for the entire step range. These results are obtained from five measurements for each step using the TDS2014B oscilloscope [63]. Each measurement is the average value of 2500 samples with a sampling time of 0.40 ms. Equations 2.3 and 2.4 determined the minimum and maximum output accuracy for different pressure resolutions at different OSR's. This showed that the heater chip voltage should be controllable with a accuracy in the range of 13.17 - 34.59 mV (or better) to allow for optimal usage of the selected pressure sensor. Previous results from the basic converter model already showed that the maximum deviation was within that range, but this was only obtained from a single measurement. Figure 4.5 examined the precision of the output voltage of the buck-boost converter. The results are promising

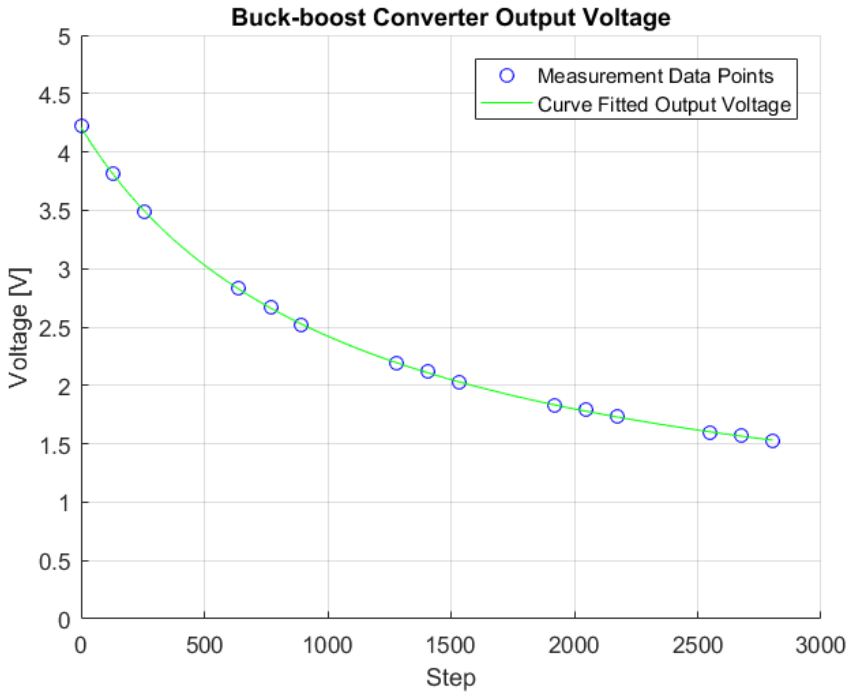

Figure 4.4: Measured versus curve fitted DC-DC converter output voltage

with a maximum deviation of 1.86 mV to the average value. The maximum output voltage is obtained with a step size of '0', which explains the better precision for smaller step values. These precision results show that biggest influence on the output performance is based on the accuracy of the converter model, with a minor impact of the precision.

A good example of the varying properties of the system is the implementation of the current sensor into the system. The ACS712 5A model adds a varying voltage drop to the voltage measured over the heater chip. The effect is shown in figure 4.6. The output voltage of the buck-boost converter does not change, but the voltage applied to the heater chip does.

The new data points with lower voltages for the same step size require an additional calibration step. The new curve fitted equation is given in 4.2. The curve fitted equation has a coefficient of determination, R-squared, equal to 99.9%.

$$V_{out,CF} = \frac{0.4771 \cdot Step + 3970}{Step + 1023} \tag{4.2}$$

The average difference between the curve fitted output voltage and the measured output voltage data points is 5.7 mV with a maximum of 19.5 mV. The resolution of the output voltage of the buck-boost converter depends on the steps of the digital potentiometers and the output range. The selected combination of digital potentiometers give the system 2806 different output levels. The maximum achievable output voltage is equal to 3877.4 mV and and the minimum output voltage is 1386.5 mV. This results in a resolution of 0.89 mV.

The implementation of the current sensor does not have a very big influence on the accuracy of the heater chip voltage, but becomes more relevant in the next paragraph. It has, unfortunately, a more significant effect on the total efficiency of the temperature control part. It should be noted that the voltage drop due to the implementation of the current sensor is not constant. It differs from 333.3 mV for the maximum output voltage (Step = 0) to 144.1 mV for the minimum output voltage (Step = 2806). The voltage drop due to the ACS712 current sensor could be caused by the internal current conductor of the Hall effect sensor. The size of the internal conductor is given the datasheet of the sensor and should be equal to 1.2 mΩ [3]. This value

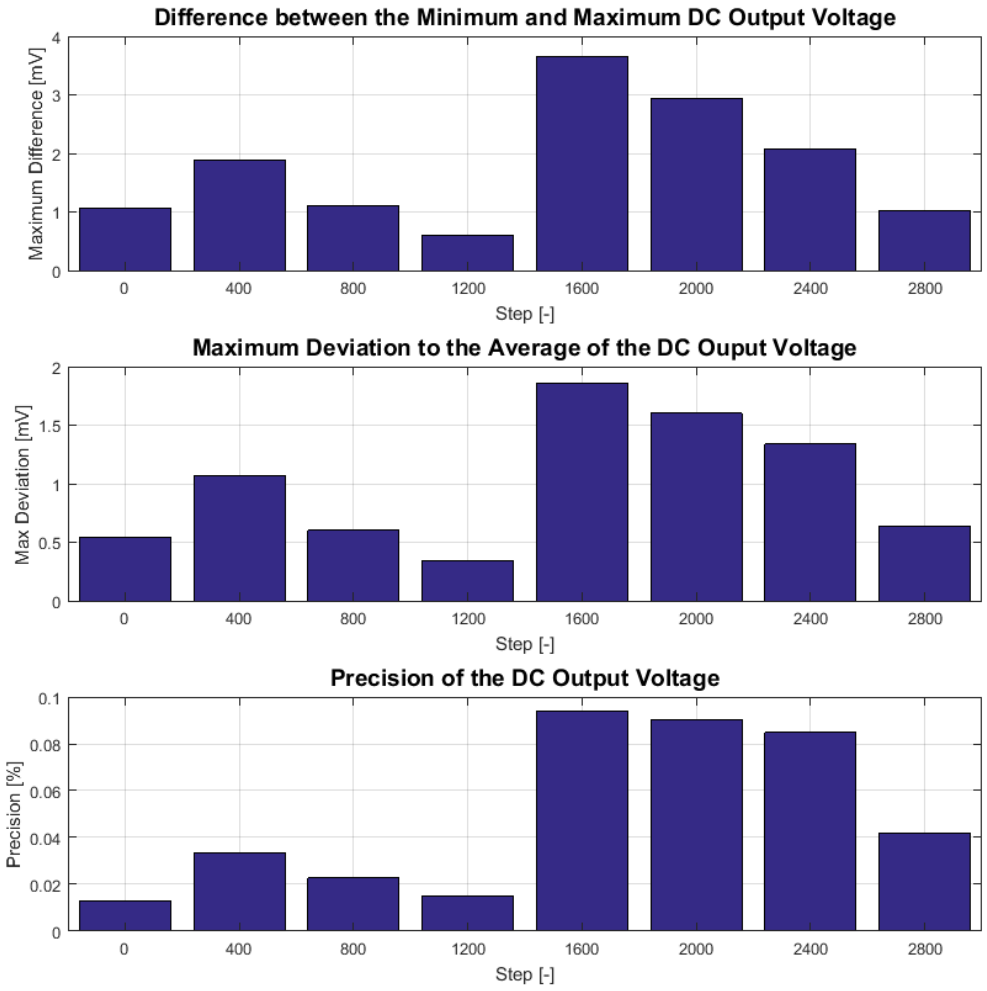

Figure 4.5: Repeatability plot of DC-DC converter output voltage

however, gives a total different voltage drop, which is determined to be approximately 1 mV in section 3.1.3.

Output Efficiency

The maximum peak power available for the micropropulsion system in a PocketQube will be consumed by three main sections: The pressure control system, the active components and the temperature control system. The valve of the pressure control system is normally closed and only requires power to be opened for a very short amount of time. The active components in the design like the microcontroller and sensors only take up to a few percent of the available peak power. The main power consuming part of the design is the heater chip. The output efficiency of the temperature control system has a large impact on the amount of power that can be supplied to the heater chip.

A schematic overview of the measurement setup that is used to determine the output efficiency of only the buck-boost converter is given in figure 4.2. The current sensor is added to the circuit to determine the total temperature control efficiency. The experimental setup of that configuration is given in figure 4.7. The power is supplied by the Agilent E3631A DC power supply [2] and the voltage is measured with the Tektronix TDS2014B oscilloscope [63].

The main factor in this process is the conversion efficiency of the DC-DC buck-boost converter, the

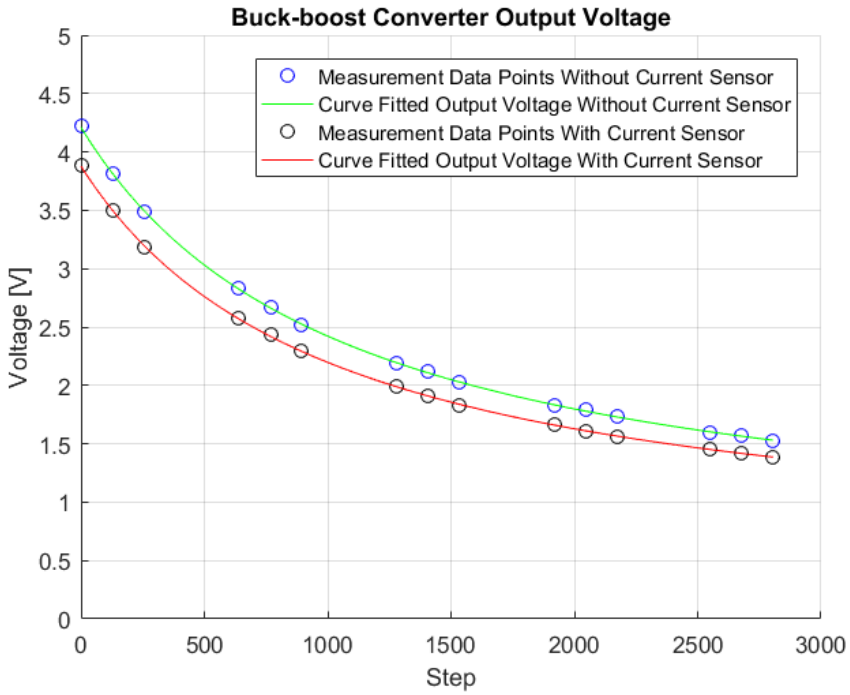

Figure 4.6: Measured versus curve fitted DC-DC converter output voltage with and without current sensor

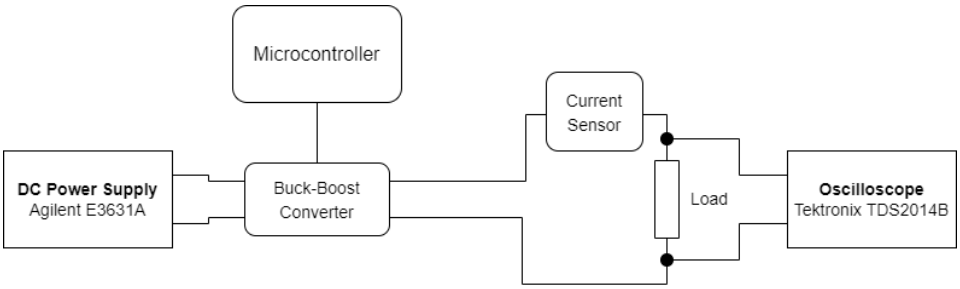

Figure 4.7: Schematic overview of the measurement setup for the efficiency of the total temperature control system

EVQ28164-D-00A [44]. The converter is presented in its datasheet with efficiencies up to 95% for optimal voltage and current values. Those values slightly differ from the estimated operational parameters of the adjustable power supply. Figures in the datasheet make it acceptable to assume that efficiencies above 90% are achievable in the estimated operational range. The insertion losses of ACS712 Hall effect current sensor also have to be considered, but should have a minor influence on the total performance of the design. Mainly due to the very low internal conductor resistance of the current sensor.

The efficiency of the adjustable power supply can be determined with the input and output power of the converter using equation 4.3.

$$\eta_{conversion} = \frac{P_{out}}{P_{in}} \cdot 100\% \tag{4.3}$$

The input power is determined using the voltage and current values of the power supply. Determination of the output power is a bit more complicated. The voltage can be measured easily, using the oscilloscope. Measuring the current is only possible by adding a current sensor in series with the load, which will affect the power supplied to the load. Therefore is chosen to determine the output power using the voltage over the load and the known resistance of the load. The load is a 3.3 Ω axial cement resistor [70], capable of handling up to 5 W of power. The exact resistive value of this resistor is measured with the Keithley Model 199 [30] and is equal to 3.417 Ω. Equation 4.4 is used to determine the output power.

$$P_{out} = \frac{V_{load}^2}{R_{load}} \tag{4.4}$$

The results of the efficiency measurements are provided in figure 4.8. These results are collected with a constant input voltage of 3.50 V and a varying input current. The conversion results of the DC-DC converter are around 90%, slightly lower than the test results from the datasheet. They are within an acceptable range of these results, considering that the manufacturer will always try to sell its product by mentioning its optimal performance. An extensive research into a better performing converter could be conducted to increase the conversion efficiency of the adjustable power supply, but that is out of the scope of this thesis project. This model shows sufficient results for this stage of the development process.

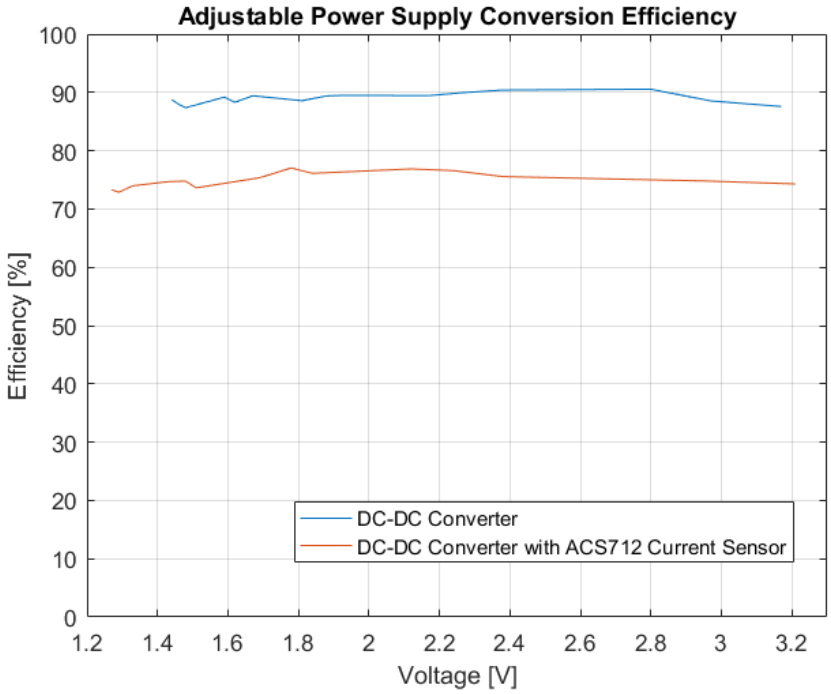

Figure 4.8: Efficiency plot of the adjustable power supply for the heater chip

A far bigger challenge is the major influence of the current sensor to the total conversion efficiency of the system. Figure 4.8 shows a relatively constant drop in efficiency of approximately 12-15% for the estimated operating range. This difference in terms of power is approximately 400 mV for 3 W input power, which is of course an unacceptable difference in provided power to the heater chip. It follows from the large voltage drop presented in the previous paragraph, which suggests that the given internal Hall effect sensor conductor resistance is not equal to the provided conductor resistance. Simple voltage division over the current sensor and the load gives a resistive value for the internal conductor of 292.81 mΩ for the maximum output voltage and 355.13 mΩ for the minimum output voltage. This removes the assumption that the internal conductor causes these losses completely, because that would give a fixed resistance for every current flowing through the sensor. Insertion losses could still cause a part of these losses, but there should also be additional explanation. The sensor could be broken or the Hall effect could have a large impact on the energy dissipation. The selected sensor is not suitable for this application in terms of efficiency. The next paragraphs will show whether it meets the expectations in terms of accuracy and precision.

4.2.2. Temperature Measurements

Temperature measurements complete the feedback loop of the temperature control system. The quality of the temperature measurements solely depends on the quality of the voltage and current sensors. This section will asses the measurement quality of both sensors. It will also investigate the impact of different sampling times and the exponential filter on the quality of the measurements. Section 3.1.1 explained the sensitivity of

the temperature measurements to minor deviations in the resistance calculations and determined the necessary temperature accuracy of 1.5% (6 °C). The sensors should be able to determine the voltage and current with an accuracy of a few millivolt and milliamps for an efficient vaporization process. Measurement deviations larger than 3.75 mV and 3.75 mA could result in temperature differences above 6 °C.

The results of both measurements are transmitted by the ADS1115 to the MCU as a 16-bit signal. The 16-bit signal has to be transformed into a voltage or current signal before it could be used to determine the temperature of the heater chip. This translation step causes, unfortunately, additional small uncertainties in the current and voltage measurements, especially when the curve fitted equation has some minor deviations to the true value. This is again difficult in a breadboard configuration, as it takes a lot of time to re-calibrate the design before each experiment. The amount of data points is therefore minimized and should be extended for the final prototype to increase the accuracy of the system.

Voltage Measurements

The voltage is measured using the 16-bit ADS1115 analog-to-digital converter [65]. The ADS1115 is configured to set its lower and upper limit to ±4.096 V. The 16-bit data value covers the entire measurement range of the converter, resulting in a theoretical resolution of 0.125 mV. A schematic overview of the measurement setup that is used to calibrate the voltage measurements of the ADS1115 is given in figure 4.9. The power is supplied by the Agilent E3631A DC power supply [2] and the voltage is measured with the Tektronix TDS2014B oscilloscope [63].

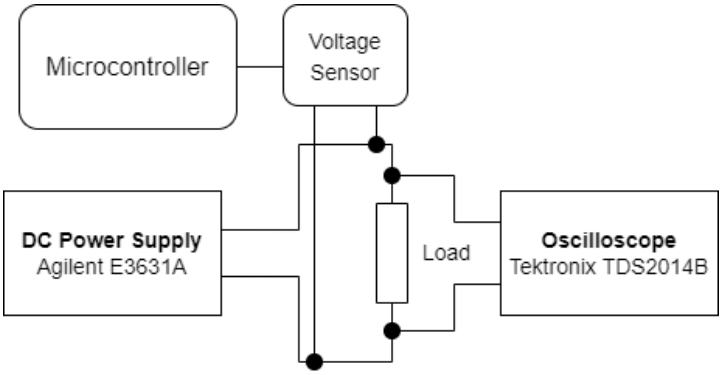

Figure 4.9: Schematic overview of the measurement setup for the calibration of the voltage measurements using the ADS1115

The curve fitting tool of Matlab is used to find the ideal translation steps. Nine data points are shown in figure 4.10 together with the curve fitted line of equation 4.5. The curve fitted equation has a coefficient of determination, R-squared, equal to 99.9%.

$$V_{heater} = Bit_{ADS1115} \cdot 0.0001248 + 0.04753 \tag{4.5}$$

Section 2.2.1 explained the pros and cons of the increasing data rate of the converter. Higher data rates decrease the conversion time and therefore also the feedback loop time of the controller, but also have a negative effect on the quality of the measurements. The impact of negative data rates will be examined using two main measurement characteristics. These two measurement characteristics are the accuracy and precision of the measurements. The accuracy is measured using the average deviation to the true value. The precision is measured using the difference between the minimum and maximum measured voltage and the maximum deviation to the average measured voltage. Each measurement consists of 100 samples with a 100 ms delay between each sample. The voltage is assumed to be steady and is supplied by the Agilent E3631A DC Power Supply [2]. The true value of output of the power supply is measured using the Tektronix TDS2014B oscilloscope [63].

Figure 4.11 shows the average deviation to the true value for eighth different voltage levels. The figure shows no clear pattern in the size of the deviations for the different SPS ratios. The deviations are, with some exemptions, comparable for each voltage level. It is therefore not possible to assign the deviations to an

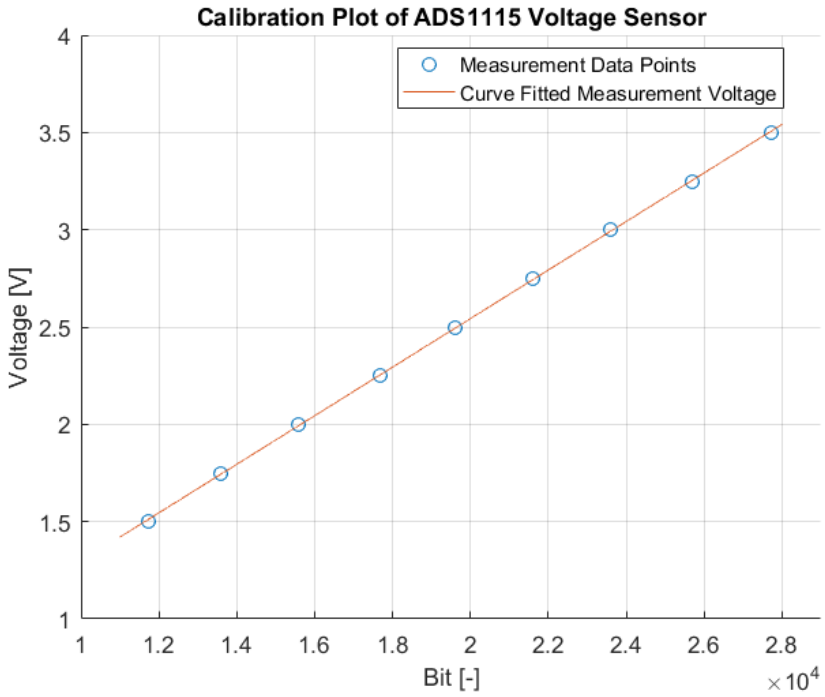

Figure 4.10: Curve fitted line for the ADS1115 voltage sensor with its measurement data points

increasing SPS ratio. The pattern of the deviations suggest that the curve fitted equation 4.5 should not be perfectly linear, but should be slightly sinusoidal or at least not completely straight. Higher order polynomials in the order of seven or eighth show a small improvement for the curve fitted line, but increase the complexity of the system. A small part of these deviations could also be assigned to the vertical DC accuracy of the oscilloscope, which is ±3% [63]. The measurements at each voltage level are conducted successively for different SPS ratios, without changing any settings on the adjustable power supply or oscilloscope. The unexpected and variable differences between the different SPS ratios can be only assigned to the measurement system itself or to the voltage ripple of the adjustable power supply. The datasheet of the Agilent E3631A DC Power Supply mentioned a maximum voltage ripple of 2 mVpp [2]. A very small part of the differences can be assigned to the output voltage ripple, but the largest part should be caused by the measurement system. These results are unacceptable for the resistance measurements, but could be (partially) solved using an extensive calibration study of the final prototype. Especially when these deviations are constant for a certain range of the measured voltage, the MCU might then be able to apply small corrections to these results. A large part of the accuracy could be therefore improved by extending the calibration study and should not have a large impact on the quality of the measurement in the final design.

The additional calibration step does not have to be very complex when the deviations to the true value could be matched with an expression from the curve fitting tool of Matlab. Then it will only require more samples at shorter interfaces and it would probably take up a bit more of computational power of the MCU. It becomes a bit more complex when the deviations are not constant, like the dashed line of figure 4.12. The example of a measured curve has different amplitudes and is not purely sinusoidal, it is of course magnified to support the example. The straight line presents the current linear expression of the basic equation for the ADS115 voltage conversion. This linear expression would still be the initial conversion step to determine in which area or range (AB, BC, CD or DB) the measured value should be. An additional expression to describe the deviation from the linear line could then be used for the exact determination of the voltage. The computational time lost for this extra step is relatively small compared to the conversion times of the analog-to-digital converter.

The impact of increasing the SPS ratio on the voltage measurements of the ADS1115 is not directly visible as a deviation to the true value. The impact becomes more relevant in figure 4.13. That figure shows three im-

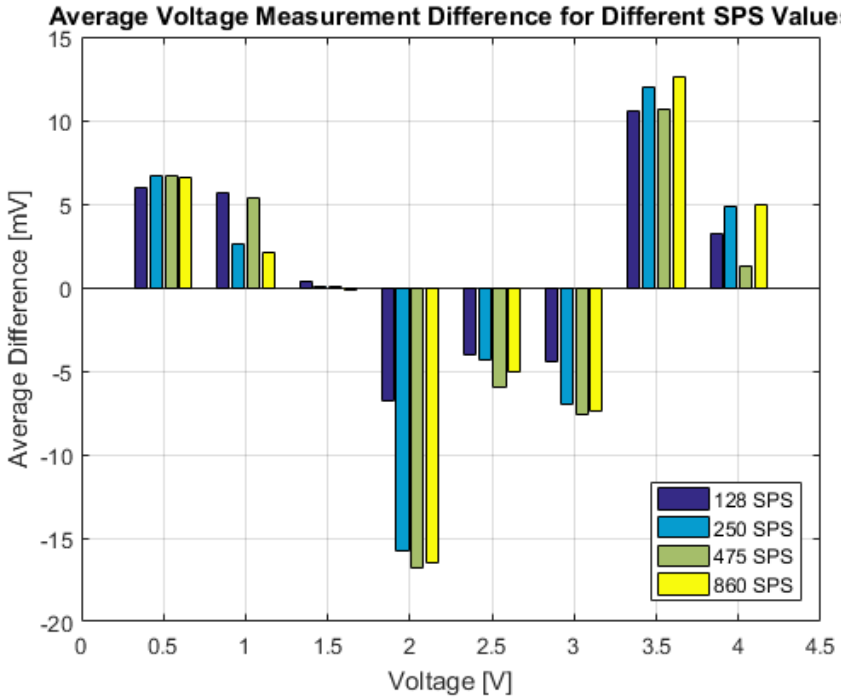

Figure 4.11: The average deviation to the true value for different SPS ratios at eighth different voltage levels

portant graph's. The top graph shows the difference between in minimum and maximum measured voltage value by the ADS1115. It shows a high level of stability for the lowest conversion time (128 SPS) and comparable, but worse, results for the faster conversion times (250, 475 and 860 SPS). Similar results are shown in the second graph of figure 4.13. This graph shows the maximum deviation to the measured average voltage at different voltage levels. There is again a relatively large difference in stability between the lowest conversion time and the faster conversion times, but also an unexpected difference between the measurements at 250 SPS and 475 SPS. The results of the measurements with a SPS ratio of 475 are more stable than the results with a SPS ratio of 250. It is difficult to explain this unexpected difference, but the amount of measurements (8 x 100 samples) suggest that its more stable to operate at a SPS ratio of 475. Some of these measurement deviations might be caused by the voltage ripple and noise of the Agilent E3631A DC Power Supply, which is at most 2 mVpp [2]. The final graph of figure 4.13 shows an increasing precision for higher voltage levels. This is of course obvious, constant deviation to the average of different voltage levels result in a smaller percentage for larger voltages. Precision levels better than 0.1% for voltage levels larger than 2 V are quite promising for the final design.

Table 4.2 summarizes the results from figure 4.13. The table clarifies the differences between the different conversion times of the ADS1115. The noticed difference between the 250 and 475 SPS ratios in figure 4.13 is supported by the averages the table, with more stable measurements results at a lower conversion time. There is a relatively large difference visible between the slowest and fastest configuration of the analog-to-digital converter. A trade-off should be made between the conversion time and measurement quality of the voltage measurements. The selection criteria will also depend on the rate of change of the temperature in the heater chip and the final requirement of the measurement accuracy. The results of the ADS analog-to-digital converter are sufficient for this application once the calibration challenges are solved, even for the fastest conversion time. A deviation smaller than ±3 mV from the true value is within the limits from section 3.1.1.

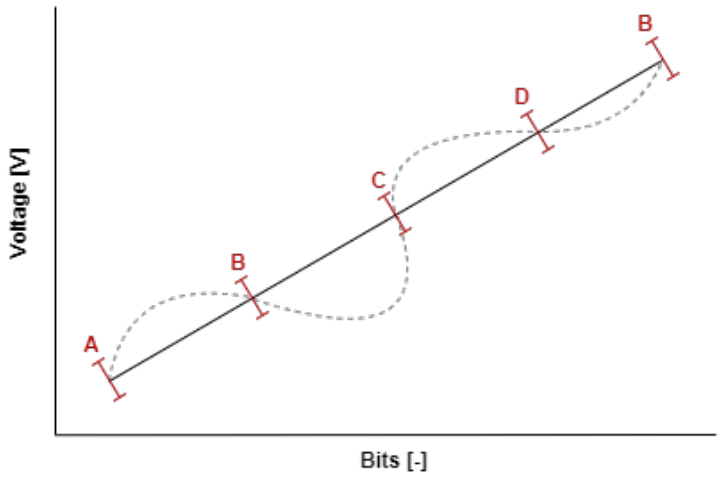

Figure 4.12: Example of inconsistent deviations to the true value, the straight line presents the current linear expression of the basic equation for the ADS115 voltage conversion

SPS	**Average Difference [mV]**	**Average Maximum Deviation [mV]**	**Average Precision** [%]
128	1.620	1.004	0.068
250	3.195	2.110	0.140
475	2.819	1.634	0.111
860	3.445	2.205	0.149

Table 4.2: Average results for different conversion times of the ADS1115 voltage measurements

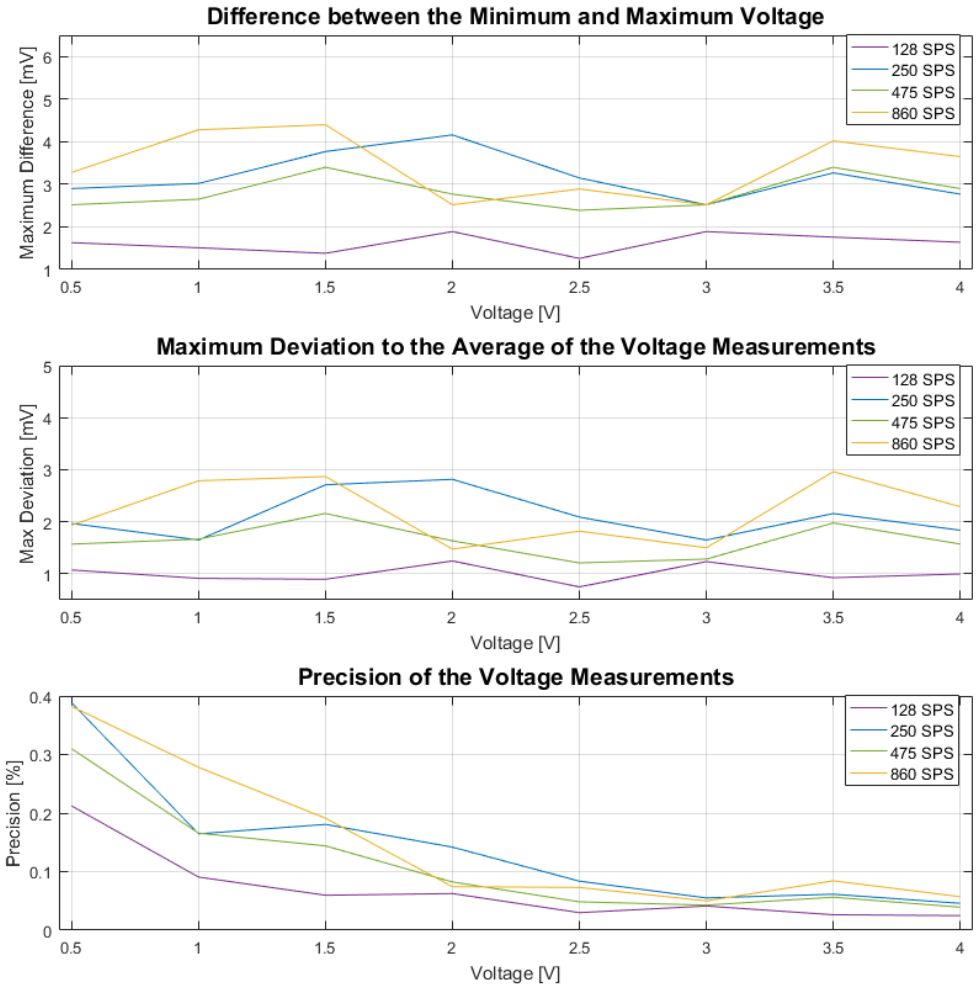

Figure 4.13: Effect of the different SPS values on the stability of the voltage measurements

Current Measurements

The current is measured with the ACS712 and ADS1115 combination. The ACS712 is a Hall effect sensor that uses the magnetic field of the current passing through the internal conductor to create an analog voltage signal. This voltage signal is converted by the analog-to-digital converter into a 16-bit digital signal. The additional conversion step with the ADS1115 is necessary because of the low analog-to-digital conversion resolution of the MCU, but also adds an additional uncertainty to the measured data. That uncertainty is similar to the results shown in the previous figures and table, which will be further increased by the measurement uncertainties of the conversion from the current to the voltage by the ACS712. A schematic overview of the measurement setup that is used to calibrate the current measurements of the ACS712 is given in figure 4.14. The power is supplied by the Agilent E3631A DC power supply [2] and the voltage is measured with the Tektronix TDS2014B oscilloscope [63]. The current through the sensor and the load is determined with the voltage over the load and the constant load resistance.

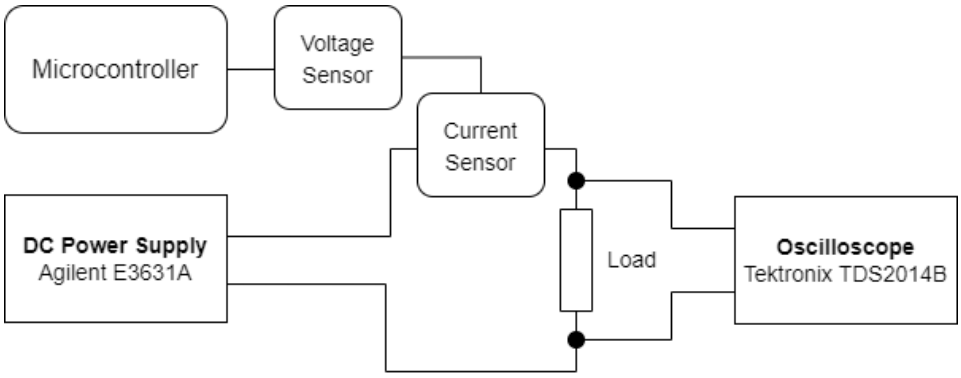

Figure 4.14: Schematic overview of the measurement setup for the calibration of the current measurements using the ACS712

Calibration of the sensor is the first step of the experimental phase of the current sensing system. The curve fitting tool of Matlab is used to find the conversion equation. Eighth data points are shown in figure **??** together with the curve fitted line of equation 4.6. The curve fitted equation has a coefficient of determination, R-squared, equal to 99.8%. The minor difference in coefficients of determination between the equations for the voltage and current sensors is also visible if we compare figure 4.10 with figure 4.15. The larger deviations to the curve fitted line in figure 4.15 could be caused by the small amount of calibration data points, but could also be a first sign of poorer stability.

$$I_{heater} = Bit_{ACS712} \cdot 0.0006678 - 13.44 \tag{4.6}$$

Figure 4.16 shows the average deviation to the true value for eighth different current levels. The figure shows a constant, increasing deviation from the true value. Indicating that the curve fitted line from the calibration is a bit too low and the slope is too small. The fastest conversion time (860 SPS) shows smaller deviations to the true value compared to slower conversion times and is less stable. The trend of increasing deviations for higher currents of 128, 250 and 475 SPS is not ideal, but is completely invisible for 860 SPS. It is therefore difficult to assign the large deviations to the true value to the insufficient calibration method for 860 SPS. This indicates that the fastest conversion time affects the stability of the measurements negatively. This average deviation for the slower conversion times (128, 250, 475 SPS) should be minimized once the hardware design is confirmed and a conversion time is selected. More data point will be required to improve the accuracy of the curve fitted line.

The presumptions of unstable current measurements from figures 4.15 and 4.16 is confirmed by figure 4.17 and by table 4.3. The top graph of figure 4.17 shows the difference between the minimum and maximum measured current for different current levels in the estimated operational range. The decreasing precision for increasing SPS ratios is generally visible in the graph and also supported by average difference from table 4.3. But there are also some unexpected outliers, like the outlier of the 128 SPS around 900 mA. These outliers plus the very large differences in measurements confirm the instability of the current measurements in this setup. This is further supported by the second and third graph of figure 4.17. Deviations of 10-15 mA will have

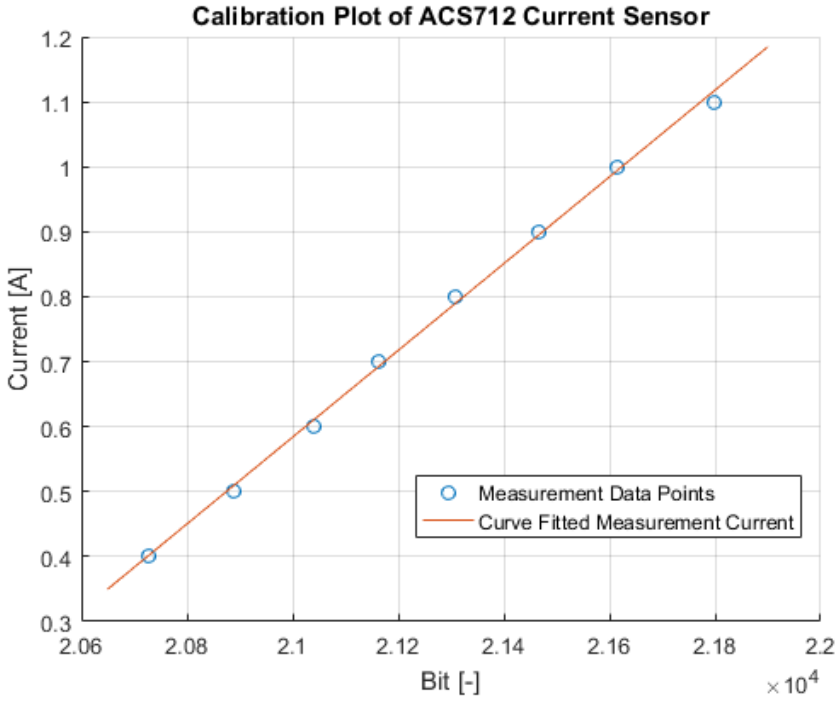

Figure 4.15: Curve fitted line for the ACS712 together with the ADS1115 current sensor with its measurement data points

a serious influence on the determination of the heater chip temperature, especially in combination with the deviations of the voltage measurements. The accuracy results of the ACS712 do not meet the measurement requirement from section 3.1.1.

The first major factor with a negative influence on the performance of the current measurements is the setup. The combination of the ACS712 and the ADS1115 is not ideal. The ACS712 has a total measurement range of -5000 mA up to 5000 mA [3]. The estimated measurement range of this system only uses a small part of that range (400 mA up to 1100 mA). The analog output voltage of the ACS712 has its center at 2500 mV for a 0 mA input. The voltage increases for higher currents and decreases for lower currents. The ADS1115 measures a voltage of 2634 mV for 400 mA and 2768 mV for 1100 mA. Which means that an increase of 700 mA results in a voltage increase of 134 mV, this is equal to 1073 bits for the ADS1115 analog-to-digital converter. The best case voltage measurements, at 128 SPS, have a precision of about 1 mV, this will increase to 2-3 mV precision for higher SPS ratios. A 1 mV deviation of the ADS1115 will result in a 5.22 mA deviation in the current measurements. The average maximum deviation from table 4.3 for a SPS ratio of 475 SPS will result in a deviation of 8.54 mA in the current measurements. This is still without the uncertainties of the ACS712. The difference in the analog output voltage of the current sensor for an increase of 700 mA is too small to be accurately measured by the analog-to-digital converter. A larger output voltage range of the current sensor would minimize the effect of the uncertainties to the analog-to-digital converter.

SPS	**Average Difference [mA]**	**Average Maximum Deviation [mA]**	**Average Precision** [%]
128	18.365	11.623	1.712
250	19.281	12.110	1.684
475	20.783	11.997	1.720
860	25.876	13.850	2.047

Table 4.3: Average results for different conversion times of the ACS712 current measurements

The datasheet of the sensor is a bit unclear about the true performance of the sensor at different operating conditions [3]. The datasheet states that the total output error at 25 °C and 5 A is ±1.5%. In addition, there is a graph that shows a decreasing accuracy for smaller input currents, but a larger accuracy for measure-

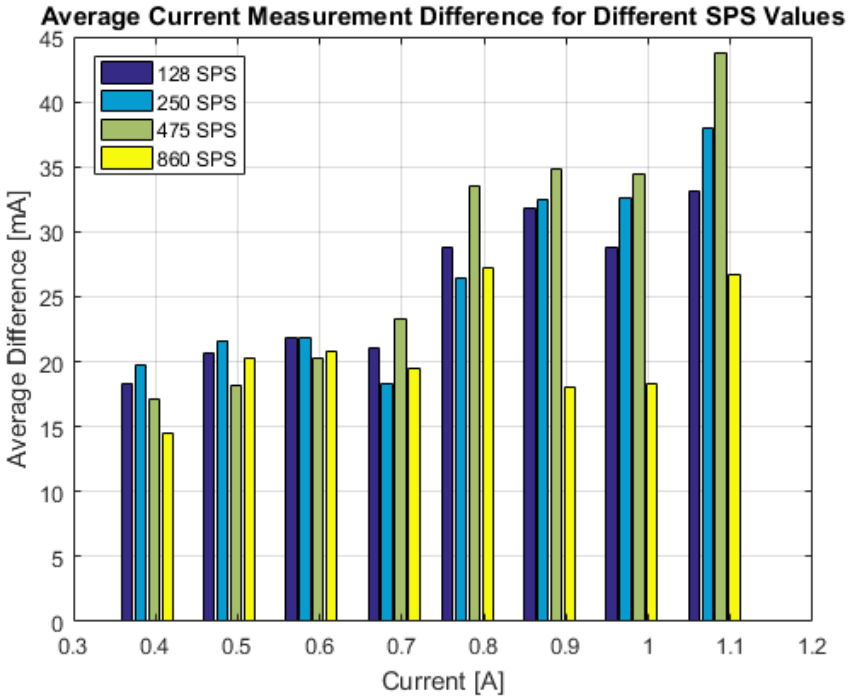

Figure 4.16: The average deviation to the true value for different SPS ratios at eighth different current levels

ments conducted at temperatures different than 25 °C. The graph is visible in figure 4.18 and does not show any numbers or data, so it only gives an indication of the estimated accuracy of the ACS712. The decreasing accuracy for higher current levels is also not visible in the measurement data, these results show a constant deviation to the true value over the entire measurement range (400 - 1100 mA). A very rough estimation based on analyzing figure 4.18 would give a total output error somewhere around 1.5%. The output error in combination with precision of the ADS1115 explains the poor performance of the current measurements.

The current sensing system of this project have to be replaced with a sensor that is able to communicate directly with the MCU. The INA219 [64] with a I2C interface might be suitable to solve the both the accuracy and efficiency problems of the ACS712. Its shunt resistance can be selected arbitrary, in order of 0.1 mΩ, reducing the insertion losses of the current sensor. This replacement will also improve the accuracy of the current measurements, due to the current sensing error of the INA219 of only 0.3 %. The minimum and maximum measurement error will be 1.2 mA (at 400mA) and 3.3 mA (at 1100 mA) respectively. A combination of the INA216 [66] with the ADS1115 [65] in an ideal configuration might also be a solution to the current measurement accuracy problem. But the additional conversion step of the analog-to-digital converter is only useful when the analog output of the current sensor is comparable with the input range of the converter. The gain error of the INA216 is equal to approximately 0.2%. A small improvement compared to the INA219, but the combination with the ADS1115 will also have a negative impact on the measurement performance.

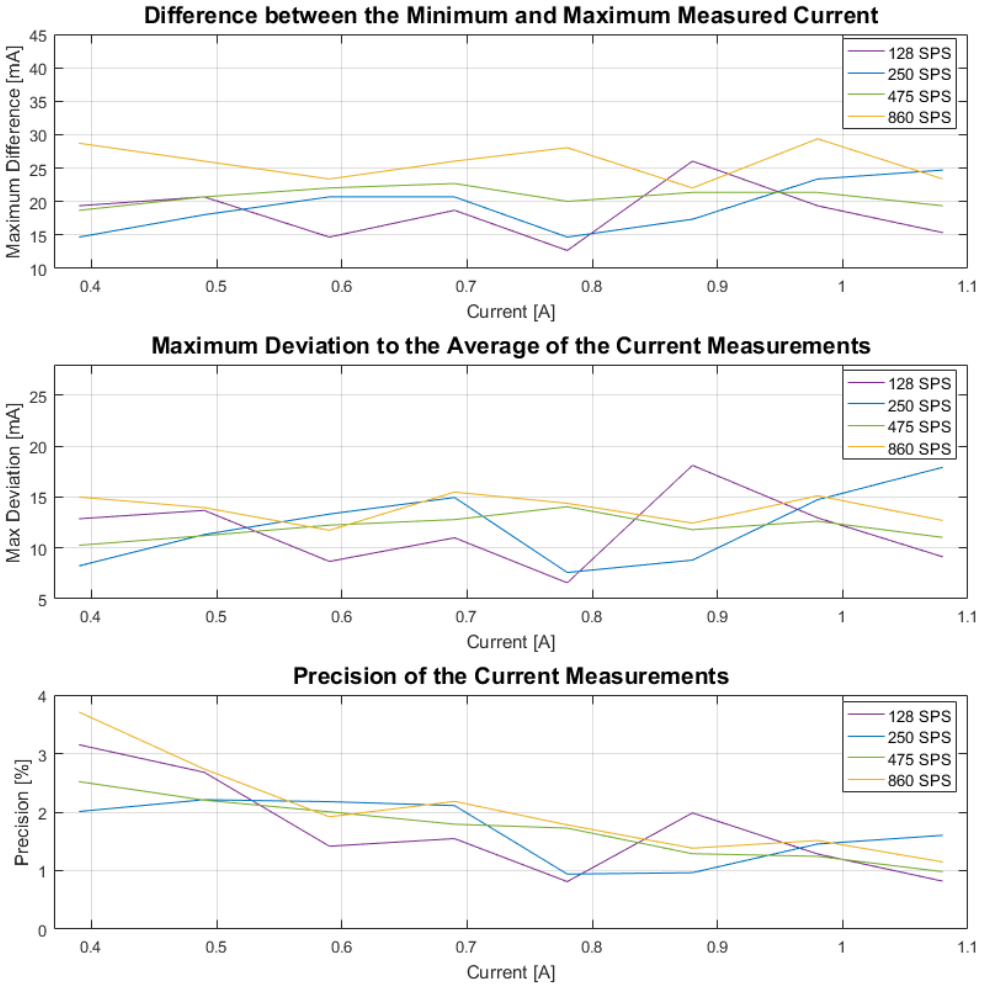

Figure 4.17: Effect of the different SPS values on the stability of the current measurements

Resistance Measurements

A schematic overview of the measurement setup that is used to examine the quality of the resistance measurements of the ADS1115 and the ACS712 is given in figure 4.19. The power is supplied by the Agilent E3631A DC power supply [2] and the voltage is measured with the Tektronix TDS2014B oscilloscope [63].

The resistance is determined with the voltage and current measurements using Ohm's law given by equation 4.7.

$$Resistance = \frac{Voltage}{Current} \tag{4.7}$$

Previous results given in figures 4.13 and 4.17 showed that especially the current measurements are not very stable, with deviations to the average measured value in the range of 10-15 mA. The stability of the voltage measurements is in the order of 1-3 mV. Equation 4.8 gives a worst-case example of the possible deviations in the resistance measurements with a large power applied to the load. A maximum deviation of 75 mΩ could follow from the instability of the voltage and current measurements. This would result in a maximum temperature difference of 20.25 °C using the 0.27 °C per 1 mΩ, obtained in section 3.1.1. A very large difference with the determined required accuracy of 6 °C from section 3.1.1.

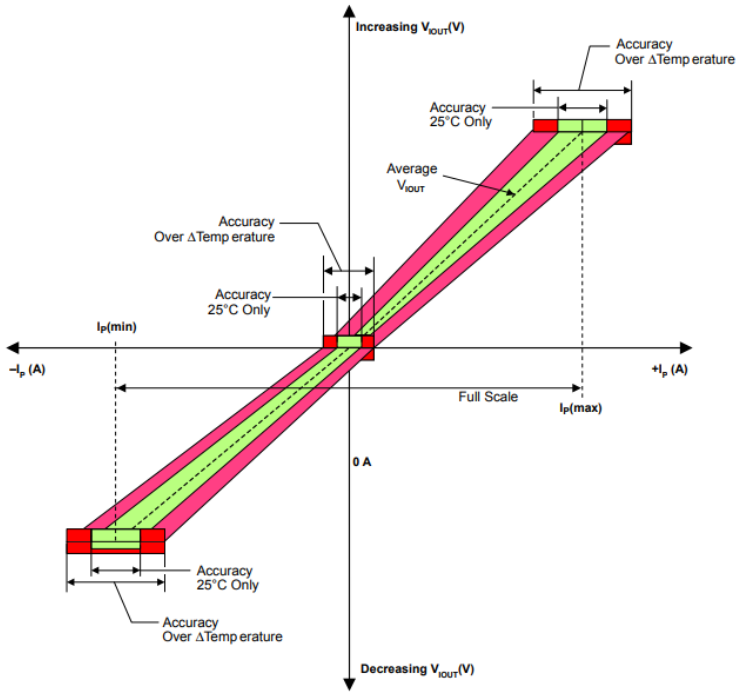

Figure 4.18: Full range measurement performance of the ACS712 given by its datasheet [3]

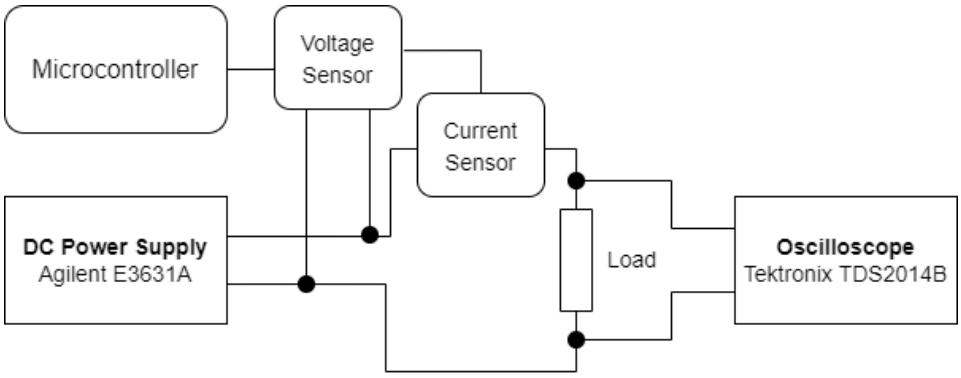

Figure 4.19: Schematic overview of the measurement setup for the quality of the resistance measurements using the ADS1115 and the ACS712

$$
\begin{aligned}
R_{low} &= \frac{2.997}{0.815} = 3.677\Omega \\
R &= \frac{3.000}{0.800} = 3.750\Omega \\
R_{high} &= \frac{3.003}{0.785} = 3.825\Omega
\end{aligned}
\tag{4.8}
$$

The stability of the voltage and current measurements is more or less equal over the complete measurement range. The stability of the resistance measurements is, however, affected differently for varying conditions at the load. An constant error is relatively larger when the measured value is smaller. This is supported by the bottom graphs of figures 4.13 and 4.17. Equation 4.9 provides an example of the predicted performance with a small applied power to the load. The resulting error to resistive value is more than twice as large (204 mΩ) compared to the previous example. This would result in a maximum temperature difference of 55.08 °C.

$$
\begin{aligned}
R_{low} &= \frac{0.997}{0.301} = 3.312\Omega \\
R &= \frac{1.000}{0.286} = 3.497\Omega \\
R_{high} &= \frac{1.003}{0.271} = 3.701\Omega
\end{aligned} \tag{4.9}
$$

The actual resistance stability measurement results are given in figure 4.20. The figure shows the results from 100 samples with a 100 ms delay at each of the seven voltage levels of the load. These measurements are conducted using a stable output from the DC power supply (Agilent E3631A [2]). The used load has a stable resistance of 3.417 Ω. The large instability of the measurements is therefore almost completely caused by the voltage and current sensors. These results follow the predictions made in this section. The measurement performance increases for higher voltage and current levels at the load and show especially poor results for voltage levels smaller than 2 V.

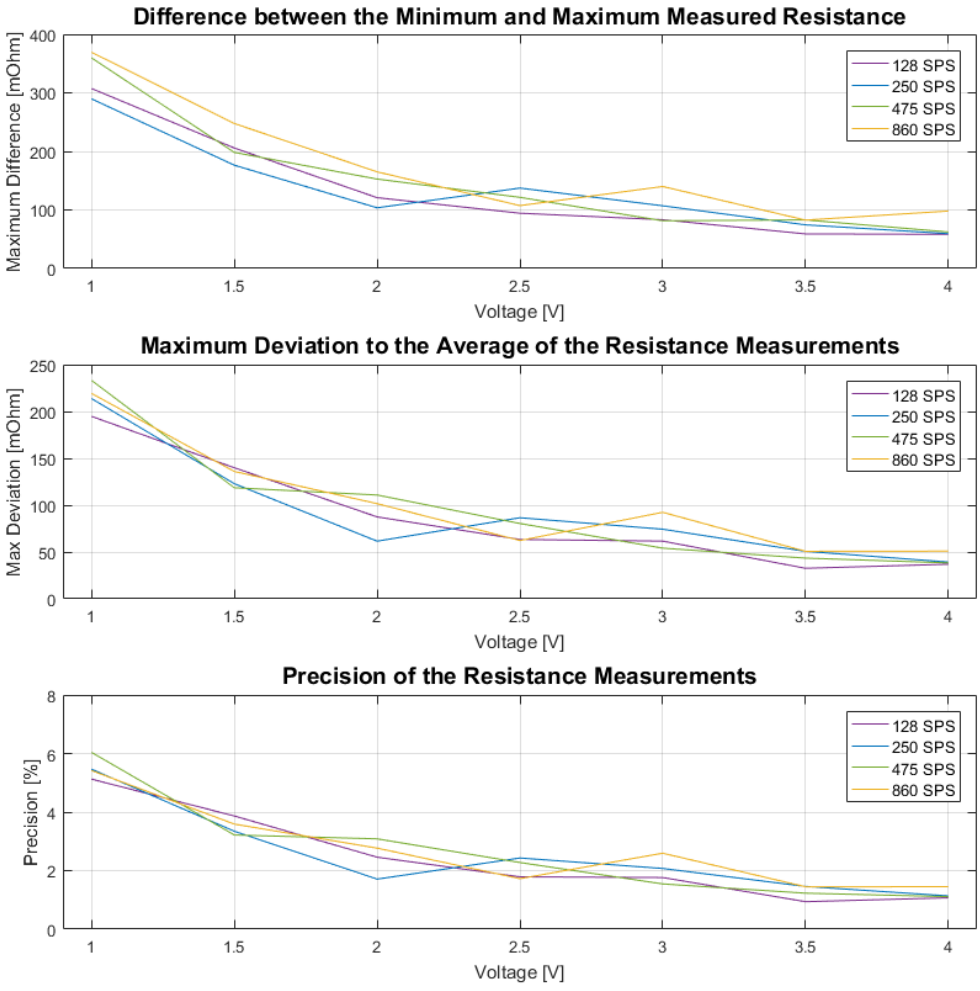

Figure 4.20: Effect of the different SPS values on the stability of the resistance measurements

The large difference between minimum and maximum determined resistance is caused by the noise of both sensors and the amplification of the noise from the current sensor by the analog-to-digital converter. Replacing the current sensor with a sensor that can directly communicate with the MCU or a sensor with a

smaller operational range will improve the measurement performance of this system. Another possibility is a smoothing filter that removes the large noise spikes sensed in the resistance measurements. An exponential filter has been implemented to improve the performance of this measurement system. The first order exponential filter is given in equation 2.2. The filter determines the weight of the new measurement relative to the previous result. A large filter coefficient results in a large weight for the newest measurement, while a small filter coefficient results in large weight for the previous result.

The performance of the resistance measurements with a first order exponential filter is given in figure 4.21. These measurements are conducted at a constant voltage and current level of 3 V and 0.88 A respectively. The average maximum deviation at 3 V of the four SPS rates before the filter is equal to 70.61 mΩ. The second graph of figure 4.21 shows that this result is improved by the filter, even with a very small influence of the previous value at larger filter coefficients. The improvement is, however, not sufficient to accurately control the temperature of the heater chip. There are only two filter coefficients, 0.1 and 0.2, that ensure that the maximum deviation at 3 V is smaller than 20 mΩ and therefore acceptable considering the determined accuracy of 22 mΩ. Reducing the applied power to the load will further decrease the performance of the measurements, as is shown in figure 4.20. It is therefore safe to assume that this combination of sensors is not sufficient to accurately measure the temperature in the heater chip. Especially because of the possible additional negative impact of accuracy deviations and instability of the buck-boost converter.

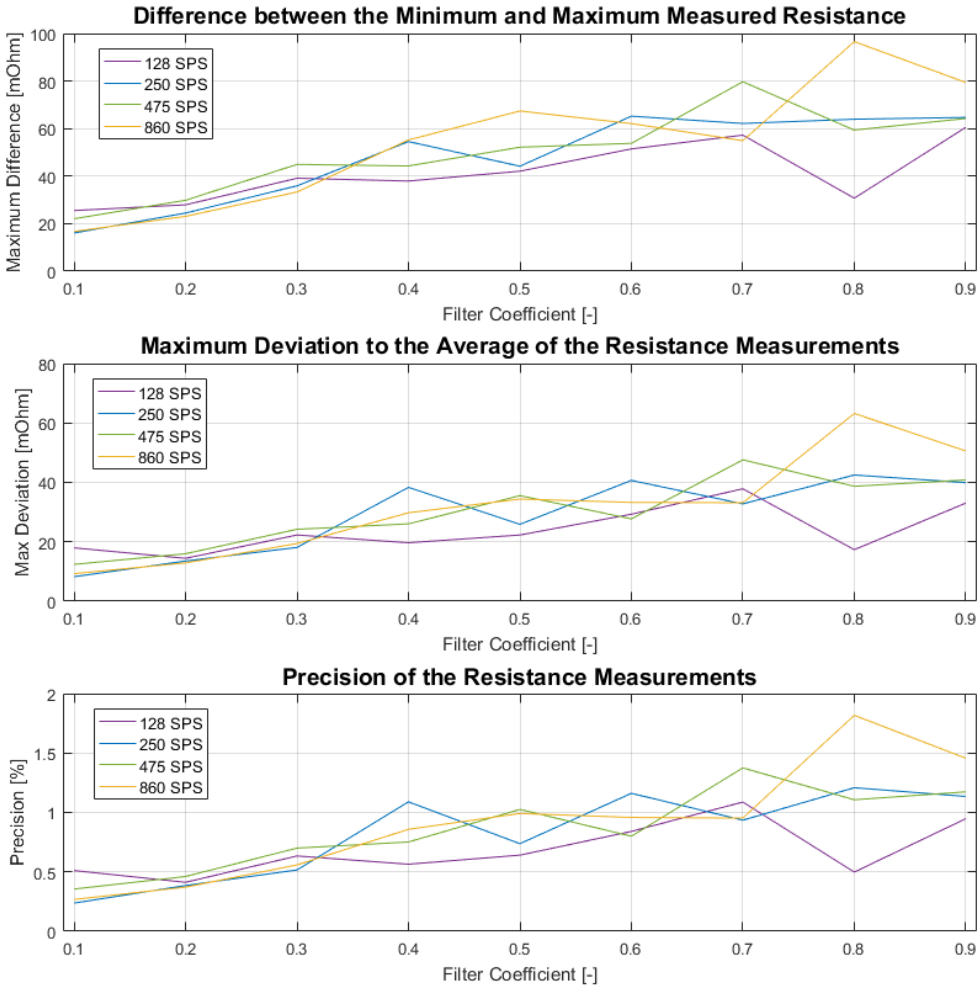

Figure 4.21: Effect of the first order exponential filter on the stability of the resistance measurements

Complete Temperature System Measurements

The previous paragraph investigated the maximum achievable precision of the combination of sensors with an exponential filter. These results do not seem to be sufficient for this application due to the major error at especially lower power levels. The other two mentioned characteristics that might have an influence on the measurement performance are the accuracy and the instability of the buck-boost converter. An ideal calibration of both sensors requires a lot of extra data and time to study its imperfections, it is therefore out of the scope of this thesis project. This is definitely so due to the conclusion that the sensor combination is not sufficient. It is, nevertheless, possible to determine the effect of the buck-boost converter on the quality of the resistance measurements.

A schematic overview of the measurement setup that is used to examine the effect of the buck-boost converter on the resistance measurements of the ADS1115 and the ACS712 is given in figure 4.22. The power is supplied by the Agilent E3631A DC power supply [2] and the voltage is measured with the Tektronix TDS2014B oscilloscope [63].

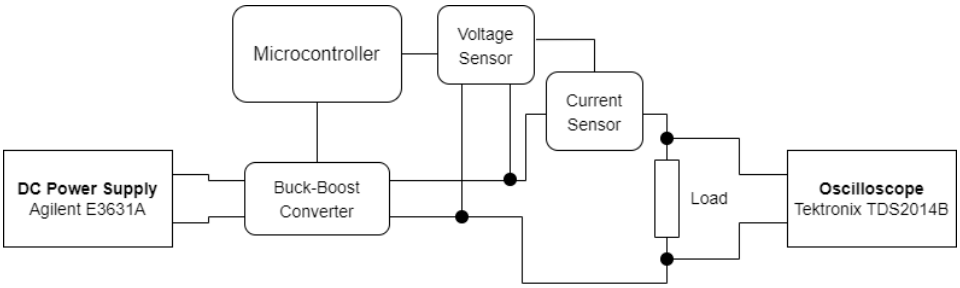

Figure 4.22: Schematic overview of the measurement setup for the effect of the buck-boost converter on the resistance measurements using the ADS1115 and the ACS712

Figure 4.23 show the performance of the resistance measurements with the power supplied by the buck-boost converter. The measurement range of this figure is smaller due to de operational range of the buck-boost converter. These graphs show that the effect of a possible unstable output of the converter can be neglected. The performance is comparable with the performance of figure 4.20. The precision of both figures stays below 5% at a voltage level of 1.5 V and is also between 1-2% at a voltage level of 3.5 V.

Although the previous results showed that the designed temperature measurement system is incapable of accurately measuring the temperature of the heater chip, it might be valuable to examine the effect on the temperature control loop. The temperature control loop is presented in section 2.2.1. The loop has a start-up sequence to initiate the temperature measurements and a PID control loop. A final calibration step with a total assembled system is necessary to improve the accuracy of the measurements. The data points and curve fitted lines of both sensors are given in figure 4.24. The curve fitted equations of both sensors are given in equation 4.10.

$$\begin{aligned} V_{heater} &= Bit_{ADS1115} \cdot 0.0001248 + 0.04518 \\ I_{heater} &= Bit_{ACS712} \cdot 0.0006513 - 13.07 \end{aligned} \tag{4.10}$$

Table 4.4 shows the resistance measurement results after the final calibration. The measurements are obtained with a SPS rate of 860 and a filter coefficient of 0.2. The maximum SPS rate is selected due to large reduction of conversion time and minimal difference in precision. The table supports the conclusions made after previous results, with improved precision for higher voltage levels. The accuracy also slightly improves for higher voltage levels. The large difference between the average resistance measurement at 1.5 V and the other voltage levels highlights poor measurement performance at lower voltage levels. The accuracy at every level should be improved in a future control system, but it is less important than the precision. A constant deviation to the true value could be covered by the MCU during the temperature calibration step. The rate of change of resistance is important to determine change in temperature after that calibration step.

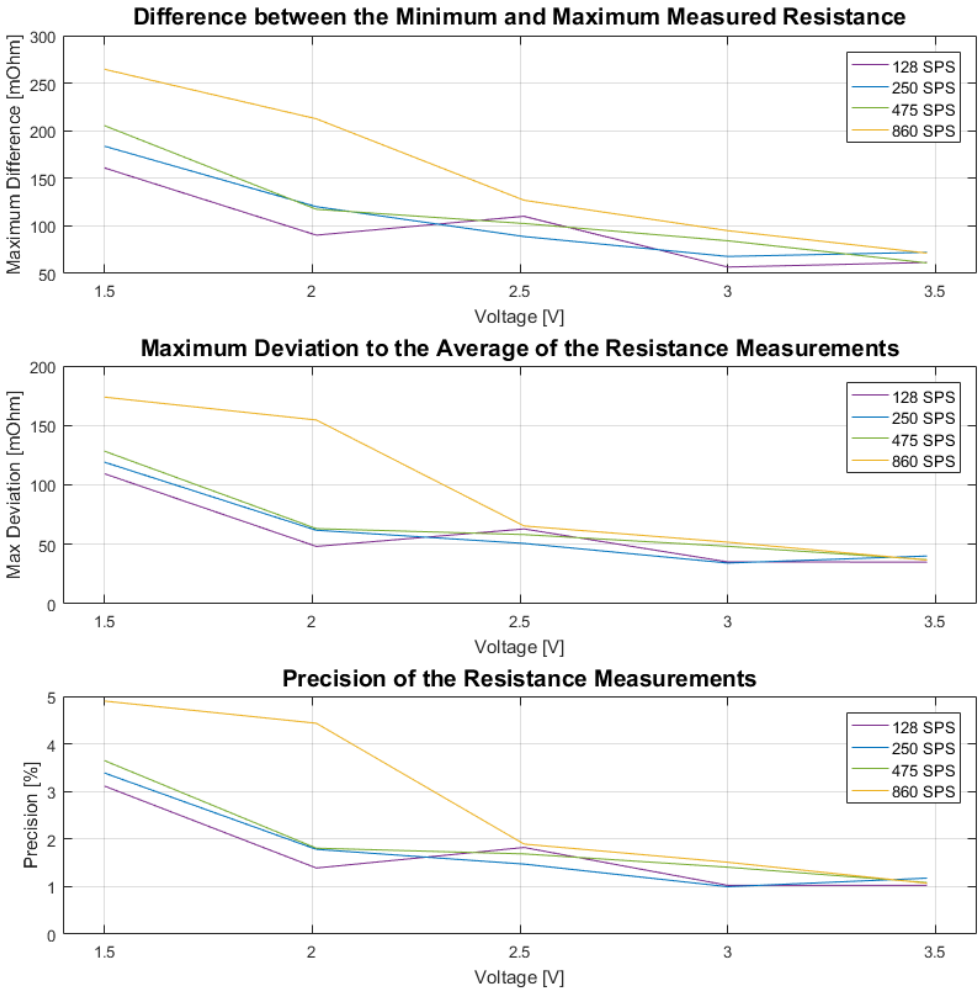

Figure 4.23: Effect of the different SPS values and the instability of the buck-boost converter output on the stability of the resistance measurements

The load is replaced with a VLM prototype with a resistance of 4081.15 Ω. A thermal camera is used to monitor the temperature of the thruster without collecting any data. Mainly to verify that the temperature of the thruster is rising during the experiment. The reference temperature of the experiment is 50 °C. A low reference temperature is chosen to protect the heater chip of the sensor without a coolant flow. Previous work experienced that the heater is destroyed quite easily due to overheating [23]. The results of the PID controller experiment are given in figure 4.25. The figures presents the measured temperature and PID output voltage over time. The voltage determines the amount of power supplied to the heater chip. It is determined by the current measured resistance and the power output of the PID controller.

The figure shows that the PID output voltage counteracts the measured temperature. The voltage rises when the temperature drops, this is especially visible during the first 4000 ms. The temperature measurements are not correct with a deviation of about 10-15 °C to the value of the thermal sensor. The system detects that the temperature is rising after 1500 ms. The PID controller counteracts that behavior by slowly decreasing the amount of power supplied to the heater chip. This continues until approximately 4000 ms. The temperature starts to approach its reference value according to the measurement system, so the controller drops its voltage to the minimum value. This has a large negative impact on the reliability of the measurements, with a growing deviation to the thermal camera measurements up to 40-50 °C. The tipping point

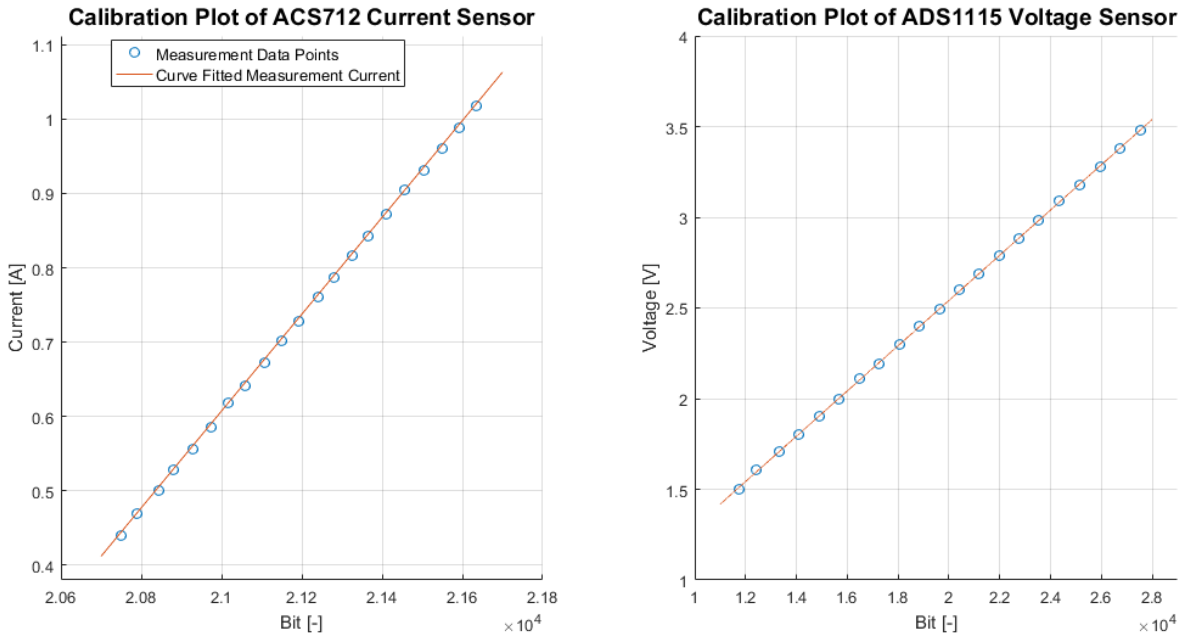

Figure 4.24: Final calibration of voltage and current sensors

Resistance	**3.417** Ω	(Keithley Model	199 [30])		
Voltage	**Average Resistance**	**Accuracy** [mΩ]	**Accuracy** [%]	**Precision** [mΩ]	**Precision** [%]
1.5	3340.16	76.84	2.25	41.71	1.25
2	3391.27	25.72	0.75	22.70	0.67
2.5	3391.42	25.58	0.75	17.40	0.51
3.0	3397.15	19.85	0.58	16.09	0.47
3.5	3396.47	20.53	0.60	9.83	0.29

Table 4.4: Final resistance measurement results with a SPS rate of 860 and filter coefficient of 0.2

at 4000 ms summarizes the main problem of this measurement system. The measurement performance at lower voltage levels is not sufficient for this application.

Temperature Dynamics Heater Chip

The temperature measurements of figure 4.25 do not have a lot of overlap with the measurements of the thermal camera. They sensed a temperature increment after 2000 ms, but at a slower pace compared to the actual temperature increment and with a large deviation. A first impression of the temperature dynamics of the heater chip was a bit unexpected and very slow compared to the dynamics of the control system. These findings can not be caused by a delay between both measurement systems. The sampling time of the thermal camera is a bit slower than the sampling time of the measurement system, 12 ms [19] versus 5.57 ms, but this difference should not be visible so clearly. An additional experiment determined the period of time necessary to increase the heater chip temperature from 30 °C to 50 °C. A schematic overview of the measurement setup that is used to investigate the temperature dynamics of the heater chip is given in figure 4.26. The power is supplied by the Agilent E3631A DC power supply [2] and the temperature is measured with the FILR AX-5 thermal camera. An example of the thermal image is given in figure 4.27. The view of the camera is perpendicular to the nozzle exit.

The DC power supply applied a constant voltage of 4.0 V to the heater chip. This resulted in a starting power of 3.18 W. The power supplied to the heater chip slowly decreased over time due to the increasing resistance and fixed voltage value, to approximately 3.11 W. The amount of power supplied to the heater chip seems to be a good estimation of the available heating power in the final design. The time is measured with a stop watch. It took the heater chip about 43 s to increase the temperature with 20 °C.

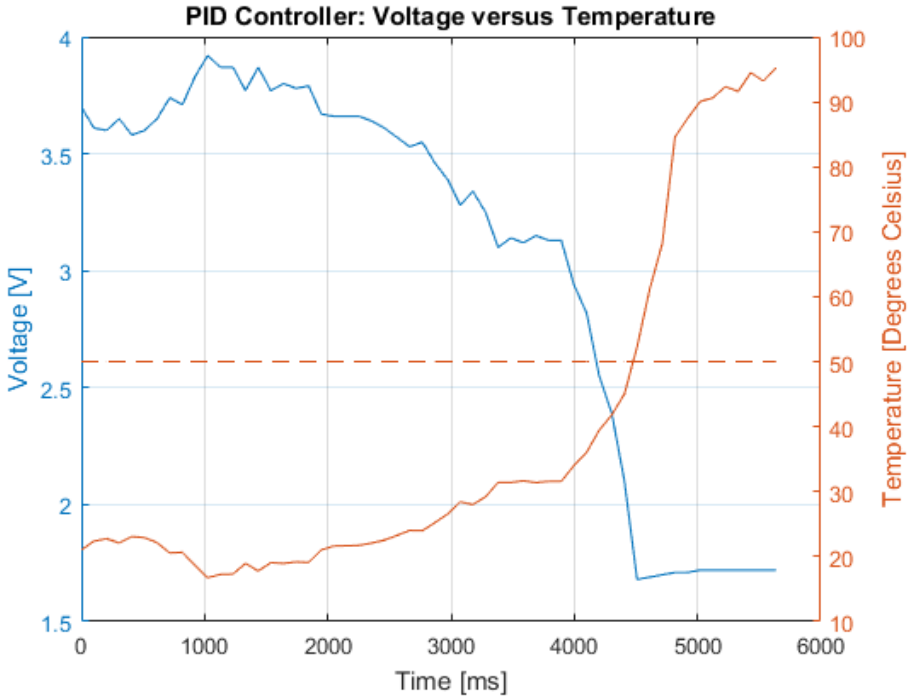

Figure 4.25: Effect of the different SPS values and the instability of the buck-boost converter output on the stability of the resistance measurements

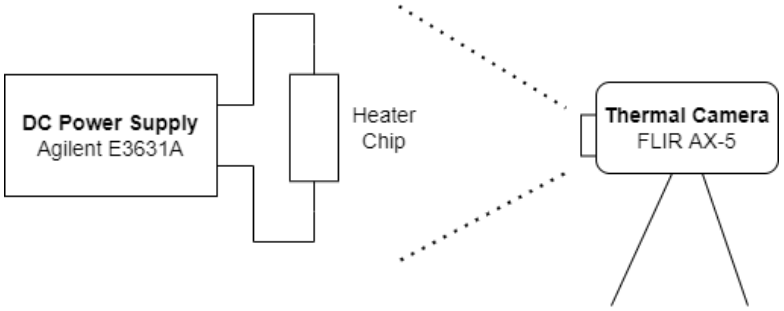

Figure 4.26: Schematic overview of the measurement setup for the temperature dynamics of the heater chip

The first 10-15 °C from the starting point went relatively fast compared to the final 5-10 °C. The same accounts for the cooling down after the power is disconnected from the heater chip. With a relatively rapid decrease for the first 10-15 °C and a very slow decrease of temperature after 10-15 °C. Although the heating and cooling speed was relatively fast in the first period after a change of power, it still seems to be very slow compared to the dynamics of the control system. This chapter examined the possibility to decrease the sampling time to increase the performance of the temperature control system. The decay in measurement quality seemed to be acceptable compared to the profit in sampling time, but those assumptions are made without considering the dynamics of the heater chip.

A very short sampling time is always valuable for a control system. It will recognize deviations to the reference value faster and is therefore also able to react faster. But when the temperature changes at a rate in the order of seconds per degrees Celsius, it might be a waste of computational power to determine the temperature almost 200 times in that same period. The dynamics of the digital potentiometers and buck-boost converter should be taken into account too. If their ability to change the output voltage is not faster than 100 or 200 ms, it does not seem to be useful to run the PID algorithm every 5.57 ms. That will only keep the buck-boost converter in a transition period and could affect the stability of its output voltage. The change of

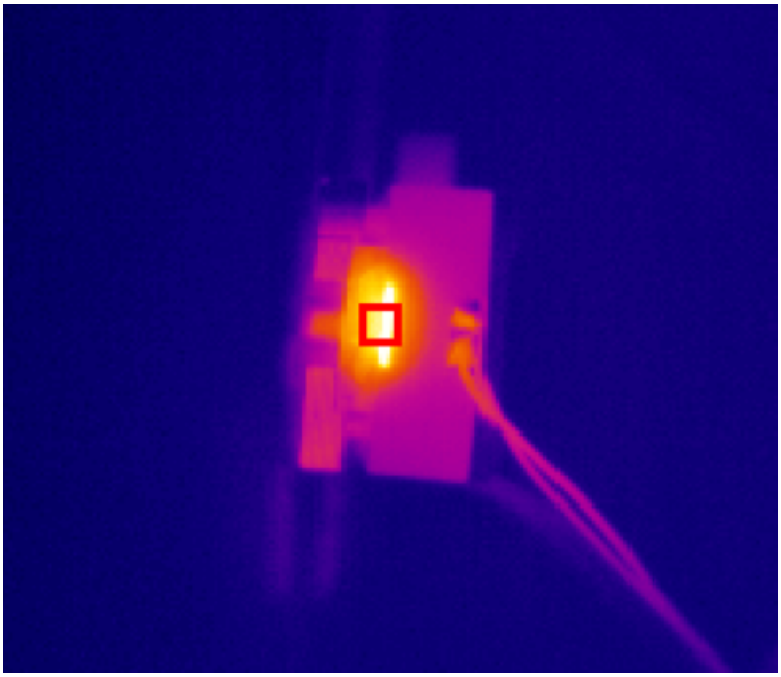

Figure 4.27: Flir AX-5 thermal camera image

voltage is of course important for the speed of the converter. Minor steps from the PID algorithm are easier to achieve in a short period of time than large voltage steps. Meaning that the PID controller should not be to aggressive to ensure that the voltage steps are also smaller, but not to small to make the system to slow to react on different mass flow rates.

An additional study into the behavior of this control system should be conducted to find a balance between these considerations. The dynamics of the pressure in the chamber are much faster with a rise time of only 0.350 ms. The demand for a shorter control loop for the chamber pressure is therefore much larger than a shorter control loop for the temperature. This could make it a waste of time to measure a negligible temperature difference in every loop, while the fluctuations in pressure are much more significant. These assumption would change the design of the combined control loop from section 2.2.3 in to a pressure main loop and a side path, once every couple of pressure loops, to control the temperature. An example of such a different functional flow diagram is given in figure 4.28. The main control loop now consists of two separate loops. The control system moves to the temperature control loop once the check parameter reaches 'X', that stands for the amount of pressure loops before the system enters the temperature control loop. This is just an example that might be beneficial for the performance of the pressure control, while it has a negligible effect on the accuracy of the temperature controller.

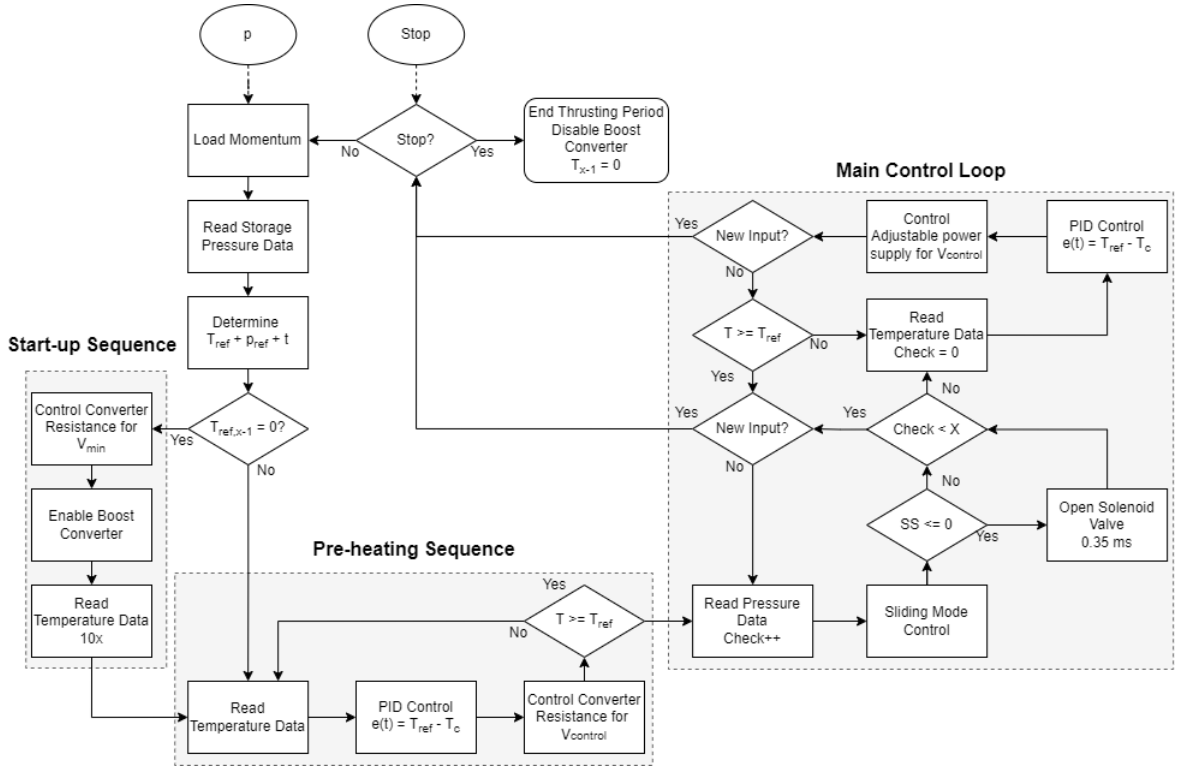

Figure 4.28: Functional flow diagram to control the thrusting of the VLM propulsion system

4.3. Pressure Control

The second main control parameter of this control system is the pressure in the chamber. There is a direct relation between the chamber pressure, chamber temperature and performance of the propulsion system. Accurate control of the pressure is essential for an efficient and stable system. An activation of the solenoid valve will increase the pressure in the chamber. The pressure will slowly decrease until the valve is activated again, resulting in an average chamber pressure. The ability to accurately control the pressure in the chamber has a direct influence on the efficiency of the system. It will allow for smaller safety margins, which will increase the mass flow rate and therefore thrust of the propulsion system. Exceeding the maximum chamber pressure could result in an incomplete vaporization process, which could result in a very poor performance or even a frozen nozzle. This section will examine the performance of the solenoid valve circuit.

4.3.1. Solenoid Valve Control

The solenoid valve is controlled by a combination of a DC-DC boost converter and a switching circuit, the details are given in section 3.2. The output of the boost converter is controlled by a combination of two resistances connected to the feedback pin of the IC. The output of the boost converter is connected and disconnected by a PMOS transistor. The PMOS connects the boost converter to the solenoid valve once its gate voltage is connected to the ground by a NPN transistor, which is controlled by the MCU. This section will examine the performance of the boost converter, the switching circuit and their effect on the solenoid valve. An electrical representation of the solenoid valve is given in figure 4.29.

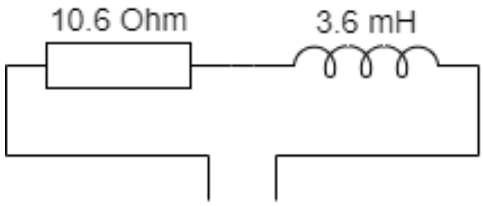

Figure 4.29: Electrical representation of the INKX0511400A solenoid valve [33]

A schematic overview of the measurement setup that is used to examine the electrical behavior of the solenoid valve and the switching circuit is given in figure 4.30. The power is supplied by the Agilent E3631A DC power supply [2] and the voltage is measured with the Tektronix TDS2014B oscilloscope [63]. The data collected by the Tektronix oscilloscope is used to examine the behavior of the spike voltage on the solenoid valve.

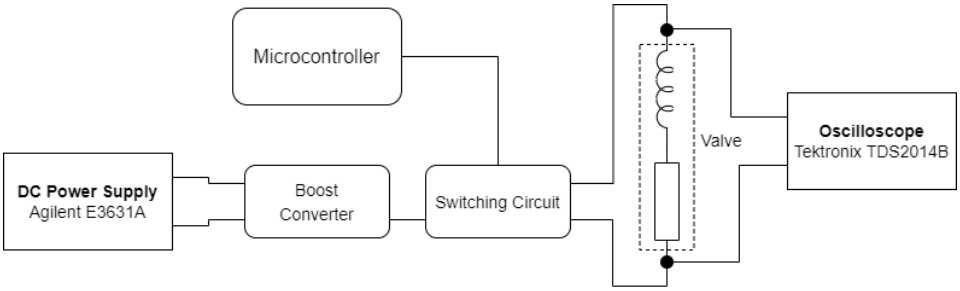

Figure 4.30: Schematic overview of the measurement setup for the solenoid valve and switching circuit

Section 3.2 proposed a resistance combination of 300 kΩ (R1) and 31 kΩ (R2) at the feedback pin. The used resistance R2 is not exactly equal to 31 kΩ, it has a measured resistance of 31.39 kΩ (Keithley Model 199 [30]). This should give a theoretical output voltage of 12.93 V. Figure 4.31 shows that behavior of the spike voltage for the solenoid valve. The MCU activates the switching circuit and the de-activates it after the minimum spike period of 350 μs. This is repeated without any other computations to acquire the signal from figure 4.31.

The red line is the necessary 12 V spike voltage level to keep the valve opened for the complete spike duration. The graph shows that there is a short period of time during the spike with a voltage level slightly below the red line. Additional experiments with a fluid flow should examine whether this would disturb the

activation of the solenoid valve, but that is out of the scope of this thesis project. Increasing the output voltage of the boost converter would also solve this problem, but that would also increase the amount of power dissipated in the valve. Lowering the voltage of R2 slightly below 30 kΩ is probably sufficient. It was unfortunately not possible to change the resistance and repeat the experiment, because of a malfunctioning solenoid valve. The duration of each spike slightly differs and is a bit longer than the delay between both HIGH/LOW operation for the analog control pin, each spike took respectively 392 μs, 397 μs and 391 μs. The longer spike times are at the expense of shorter down times, suggesting that the valve will not directly close after changing the voltage level of the analog output pin. The delay between the HIGH/LOW operation could be shorter to ensure an opening time of 350 μs.

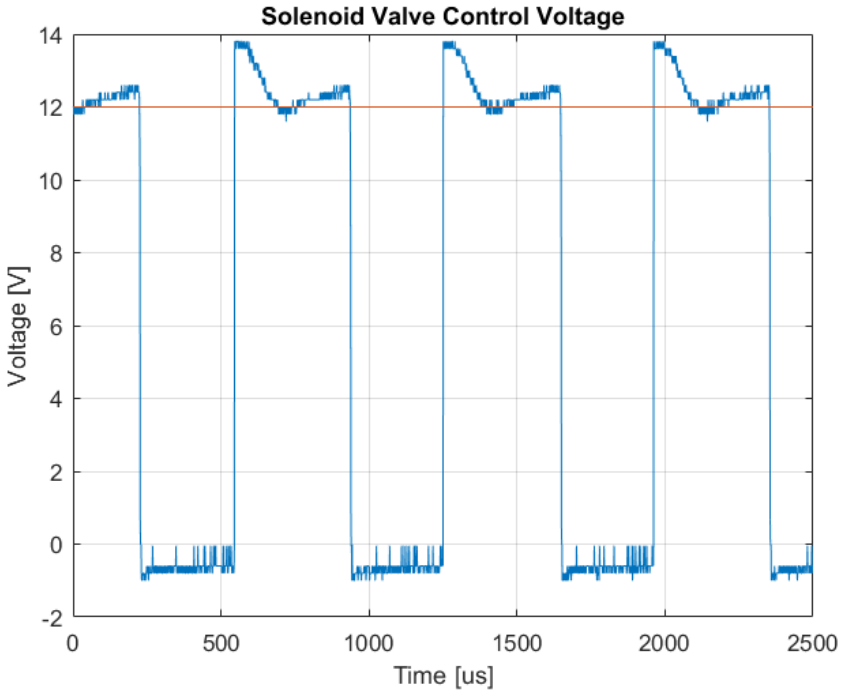

Figure 4.31: Solenoid valve control voltage over time

It is difficult to distract the power supplied by the DC power supply due to the fast dynamics of the system. The required input power of the spike could be determined from the efficiency of the converter and the dissipated power of the solenoid valve. The average efficiency of the boost converter is tested to be 81.89% for the operational range of the spike circuit. The exact resistance of the solenoid valve is measured to be 10.60 Ω. The power dissipated by the solenoid valve can be calculated with equation 4.4, the power over time is given in figure 4.32. These results show that it is not possible to open the valve using 4 W power available for the micropropulsion system without an additional energy storage system. The amount of energy dissipated by the solenoid valve for a single spike is equal to 0.89 μWh and 1.08 μWh when the conversion losses are taken into account. The battery of the PocketQube cannot deliver more than 0.44 μWh during that same period. It will take approximately 970 μs to acquire enough energy to open the solenoid valve. Although the spike times of the example experiment of figure 4.32 are a bit longer than the assumed 350 μs, the required energy for a single spike is still smaller than estimated spike energy (1.85 μWh) of section 3.4.1. This is mainly caused by the lower average spike power, 14.70 W measured versus 16.14 W assumed. The final output voltage of the boost converter should be slightly larger, to keep the voltage over the valve above 12 V. A larger voltage will increase the energy dissipated during a single spike, but the spike time can also be a bit shorter. It is therefore assumed that these results give a good approximation of the final spike energy requirement of the solenoid valve.

Ref. [55] concluded from pressure experiments that the rise time of the pressure is much faster than the decay time of the pressure. The time that the valve should allow propellant to flow to the chamber could be

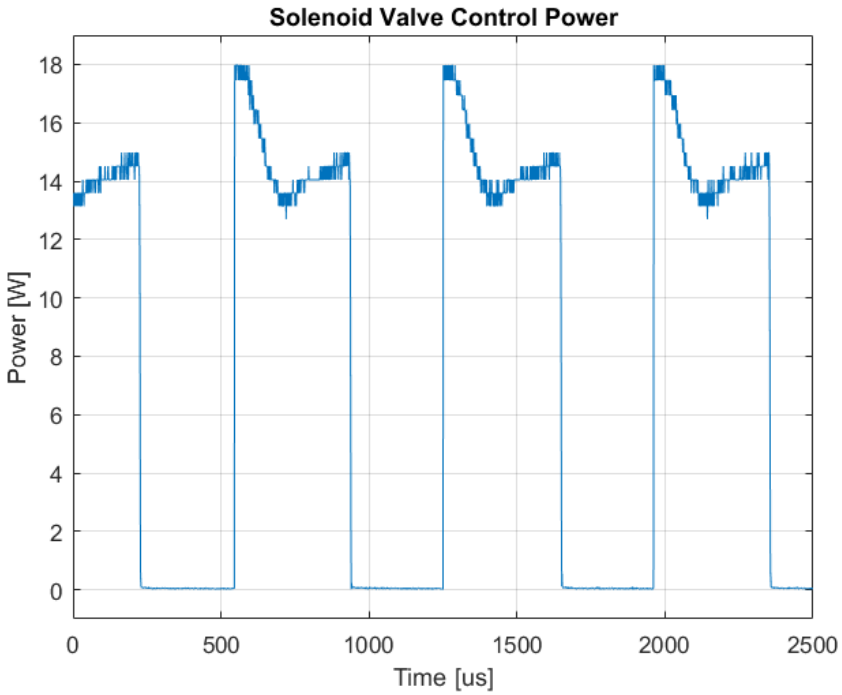

Figure 4.32: Solenoid valve control power over time

therefore much shorter than the time that it should be closed. Exact rates are unfortunately not provided, but the project used a sampling period of 40 ms. The minimum time between two spikes is then equal to the sampling time of 40 ms. It will take approximately 2.43% of the available energy between two spikes to charge an additional storage device or the battery of the satellite. These numbers do not consider the charge and discharge losses of the storage device. This seems to be an acceptable part of the supplied power to the micropropulsion system, but it will increase for smaller sample times up to almost 20%. Adding another factor to the trade-off for the ideal sampling time of the pressure control loop. Future research should be conducted to find an optimal storage device or whether it is possible to use the battery of the satellite for the pressure control system.

4.4. Conclusion

This section summarizes the content of the experimental part of this project. The experiments are mainly focused on the electrical behavior and performance of the control electronics. The configuration of these electronics is given in section 3.4. A list of equipment with their usage is provided at the start of the chapter. The main equipment used during this project is the Agilent 3631A DC power supply and the Tektronix TDS2014B oscilloscope.

The theoretical model of the output of the buck-boost converter has been validated by 15 data points over the entire operational range. The theoretical model approaches the actual output, but the differences due to a few uncertainties are still too large for this application. An additional calibration step using the curve fitting tool of Matlab has been performed to increase the output accuracy. The average accuracy of the model is equal to 5.9 mV with maximum of 13.0 mV. The precision results from a repeatability experiment have a much smaller influence on the final output performance, with a maximum deviation of 1.86 mV to the average output. These results combined meet the requirements that followed from the resolution of the pressure measurements. Except for the case of the highest pressure resolution, which requires an output accuracy of 13.17 mV. An additional, extensive calibration step might decrease the maximum deviation with a few millivolt to meet the requirements from the pressure resolution completely. Implementation of the current sensor (ACS712) to the circuit, resulted in an average voltage drop of approximately 250 mV. A new curve fitted model with similar accuracy characteristics and a resolution of 0.89 mV have been proposed to regulate the amount of power supplied to the heater chip. The implementation of the current sensor also has a large effect on the output efficiency. The total efficiency decreases from about 90% to 75-78%. The selected current sensor is therefore unsuitable in terms of efficiency.

The quality of the temperature measurements depend on the performance of the voltage and current sensors. The results from the voltage measurements seem to be within the acceptable range, with an average deviation in order of a few mV and a precision of approximately 0.1%. This can not be said about the current measurements, with average maximum deviations of 11-14 mA and a precision of about 1.75%. Only a small part of these large differences are caused by the inaccuracy of the ACS712. The largest part is a result of a bad combination of sensors. The analog voltage signal from the ACS712 is converted to a digital signal by the ADS1115 with a very small voltage range of 134 mV for a current range of 400 - 1100 mA. A 1 mV deviation in the ADC conversion will result in a 5.22 mA deviation in the current measurements. The few mV deviation in the voltage measurements cause a very large deviation in the current measurements, especially at lower conversion times. It is also possible that a part of these deviations is caused by the voltage ripple of the power supply. The maximum voltage ripple is 2 mVpp. It is difficult to determine how large the precise effect of the voltage ripple is on the measurement performance, but also safe to assume that the actual performance is slightly better than the results of this chapter.

These deviations also also have a large impact on the resistance measurements. The measured maximum deviations are in the order of a few hundred mΩ for less applied power and about 50 mΩ when more power is applied to the load. The large deviations for lower power levels is caused by the constant deviations in voltage and current and smaller measurement values. Suggesting that it will be more challenging to determine the heater chip temperature when less power is applied. The large deviations are removed from the measurements using an exponential filter. The filter has a positive effect on the measurement quality with some acceptable results (5-6 °C) in ideal conditions, but this will not be sufficient for this application. Even tough a small part of the measurement deviations could be assigned to the voltage ripple of the power supply, the differences are still too large to approach the given requirements. The current sensor has to be replaced by for example the INA219 in a future design to increase the measurement results to an acceptable level.

A simple experiment showed that the temperature dynamics of the heater chip are very slow compared to the dynamics of the control system. It took approximately 43 s to increase the temperature of the heater chip from 30 °C to 50 °C with an average input power of 3.15 W. The heating and cooling speed was relatively fast in the first period after a change of power in room conditions, but still seems to be slow compared to the dynamics of the control system. A very short sampling time is always valuable for a control system. But when the temperature changes at a rate in the order of seconds per degrees Celsius, it might be a waste of computational power to determine the temperature almost 200 times in that same period. The demand for a faster control loop for the chamber pressure is larger than a faster control loop for the temperature. These

findings could change the design of the combined control loop from section 2.2.3 in to a pressure main loop and a side path, once every couple of pressure loops, to control the temperature.

Finally, the solenoid valve control circuit has been tested. The experiments showed that the theoretical boost converter output voltage of 12.93 V was not sufficient to ensure that the spike voltage stayed above the boundary of 12 V. The output voltage of the boost converter should be increased by a smaller resistance R2 to the feedback pin. The efficiency of the boost converter for spike conditions was 81.89%. Calculations showed that it will take approximately 970 μs of the total peak power to collect enough energy for a single spike. This is, divided over the complete time of the measurement delay, about 2.43% of the peak power. The percentage of power necessary to charge an additional storage device will increase almost 20% for the shortest control loop. This part of the peak power will be at the expense of the available heating power. Another important factor for the discussion about the optimal duration of the control loop. Additional research should be conducted to determine whether the battery of the satellite is able to supply the required peak power or to find the ideal storage device for this application.

5

Conclusion

This chapter intends to draw conclusions on the work presented in this report. The findings and results of this project will be combined in this chapter to create a clear and complete picture of the work. Recommendations will be shortly mentioned to provide the right connection with the results and will be explained in section 6. This report presented the hardware and software design of a potential control system for the VLM concept. The final section presented the experiments that are conducted to verify the performance of the selected hardware. The goal of this project was:

The general objective of this Master thesis project is to control a ground prototype of the Vaporizing Liquid Micro-resistojet by selecting an efficient control strategy and by designing the additional control electronics, considering the limitations based on the requirements of PocketQubes.

Three main research questions were formulated to realize the goal of the project. These research questions will be repeated and answered in this section together with some important additional findings.

1. What is an efficient control strategy to regulate pressure versus power in the Vaporizing Liquid Microthruster designed for the Delfi PocketQube?

The control strategy depends on a few important factors. The first is an analytical model to estimate the potential orbital performance of the propulsion system. Different complex models are proposed in literature that are often based on experiments. A complete model should combine the basic IRT assumptions with the boiling instabilities, nozzle performance and a thermal model of the propulsion system. This report presented a very basic analytical model that could be used to make a first estimation of the performance. An comprehensive model is out of the scope of this project. The power versus pressure relationship is experimentally determined by Ref. [23]. This relation is the initial step to the main control parameters. The pressure that follows is the first main control parameter. That pressure is thereafter used to determine the second main control parameter: temperature.

Three different functional flow diagrams have been proposed in this report. The first two are solely designed for the experimental phase of the project, to verify the performance of the temperature and pressure control systems separately. The final functional flow diagram could be used to control a propulsive operation. The diagram has two different versions due to the uncertainties of the temperature dynamics of the heater chip. The response to a different applied power is relatively slow compared to the temperature control loop. This suggests that it might be possible to take temperature measurements out of the main control loop into a side path that could be used after a certain amount of pressure loops. The final important factor of the control strategy are the selected control mechanisms to regulate the temperature and pressure in the chamber. A PID controller is proposed to be used to control the temperature in the chamber. The pressure could be controlled by the hybrid sliding mode controller from Ref. [55]. The SMC controller activates the solenoid valve to open the valve for the minimum spike time. The control parameters of the controllers mainly depend on the measurement delays and the dynamics of the heater chip and chamber. The measurement delays could

be reduced by decreasing the conversion times of the sensors.

2. What is the ideal configuration of sensors, actuators and additional electrical components to support the selected control strategy?

The control strategy has two main control parameters: temperature and pressure. The temperature can be controlled with the heater chip without additional sensors in or near the chamber. The heater chip converts electrical energy into thermal energy for the vaporization process. The resistance of the heater chip is made of Molybdenum, a temperature sensitive material that will be used to determine the temperature in the chamber. The heater chip power is controlled by a DC-DC buck-boost converter (EVQ28164-D-00A). The output voltage of the converter depends on two digital potentiometers, with resistive values of 10k (MCP4162-103E) and 100k (MCP4162-104E), connected to the feedback pin of the converter. The adjustable power supply has a resolution of 0.89 mV and an average efficiency of 90%. The temperature measurement system needs the resistive value of the heater chip to determine the temperature in the chamber. The ADS1115 analog-to-digital converter is used to determine the voltage over the heater chip with an average precision of 0.1%. The current is measured by a combination of the ACS712 Hall effect sensor and the ADS1115. The ACS712 converts the current into a voltage signal for the analog-to-digital converter. This additional conversion step causes major deviations in the measurements with an average precision of 1.75%. The resistance measurements are therefore very unreliable with deviations up to a few hundred mΩ, especially when the power applied to the heater chip is small. These results do not even approach the proposed requirement of 6 °C (22 mΩ). The measurement system is only able to meet that requirement in nearly optimal conditions, using an exponential filter with a very small filter coefficient. The current sensor also reduces the efficiency of the adjustable power supply with approximately 12-15%. The sensor should be replaced in future work by for example the INA219 to improve the performance of the temperature control system and meet the proposed requirements.

The selected solenoid valve (INKX0511400A) requires a minimum spike voltage of 12 V. That voltage is supplied by a boost converter (EVQ3428A-L-00A) with a required output voltage of at least 13 V. The boost converter has an efficiency of 81.89% for the operational conditions. The ON/OFF cycle of the solenoid valve is controlled by a basic switching circuit. An NPN-transistor (MJE15032G) controlled by the MCU pulls the gate of a PMOS transistor (AOI21357) to the ground to close the switch and to allow the current flow from the boost converter to the solenoid valve. A diode (1N4005) is connected in parallel with the solenoid valve to protect the transistor from the inductive voltage spike. Noticeable is the amount of energy necessary to activate the solenoid valve. It requires approximately 1.08 μWh (including conversion losses), this is compared to the available energy in that same period (0.44 μWh) quite large. This does not have to be a big problem when the period between two spikes is sufficiently large. It might be possible for the on-board satellite battery to supply the large amount of power required for the spike. Otherwise it is necessary to develop a dedicated storage system to store the required spike energy. The microcontroller selected for this project is the Arduino Uno. It is based on the ATMEGA328P and is ideal for current phase of the project due to its accessibility for testing in breadboard configurations.

3. What are the potential challenges in meeting the requirements of the propulsion system for a PocketQube?

A number of major challenges have been discovered during the experimental phase of this project. One could divide them into a few categories. The first category is the ability to supply sufficient power to the heater chip and solenoid valve. The power distribution system of the design is assumed to be stable and efficient, but the energy requirements of the solenoid valve create a difficult challenge. The required peak power and energy for a single spike exceeds the available peak power and energy for the micropropulsion system. Additional research should be conducted to determine an efficient solution to this storage problem.

The second category is the ability to collect accurate measurement data without affecting the conversion efficiency. This solely accounts for the current measurements of the heater chip. The sensor have be to placed in series with the heater chip, but can not dissipate to much energy. In addition, there is the proposed requirement of a maximum accuracy of 6 °C (22 mΩ), which becomes especially challenging when less power is applied to the heater chip. The voltage measurement accuracy is assumed to be sufficient, but the current measurement accuracy needs to be improved.

The final category is the control strategy with a major trade-off for the optimal sampling time of the control loop. That also includes the possibility to create two separate loops, one for the pressure and one for the temperature. A very fast sampling time for the temperature loop might be useless because of the slow dynamics of the buck-boost converter and heater chip. In addition, it also has a negative effect on the quality of the measurements. Yet it is also possible that a faster system is necessary for the final prototype in nearly operational conditions. The response time of the solenoid valve control circuit is sufficient and will not affect the sampling time of the loop, but the amount of energy dissipated in the valve could be important. A shorter sampling time decreases the transient period between two possible spikes. The amount of energy for a single spike needs to be collected and stored in a shorter period of time when the transient time between two spikes is smaller. That same amount of energy could be very valuable for the vaporization process. It could increase the maximum chamber temperature and therefore the maximum chamber pressure. Larger chamber pressures increase the thrusting performance of the system, but also need a shorter transient time between two spikes. Finishing the trade-off between different control parameters of the propulsion system. This circle of consequences have to be examined in future projects and will be included in the recommendation chapter (6) of this thesis.

The main goal of this Master thesis project is partly achieved. A control strategy and system have been proposed, but didn't operate as expected. Additional work is necessary to improve the electronics and test the proposed control strategy.

6

Recommendations

This Master thesis project is the first step to an efficient control system for the VLM concept of the Delft University of Technology. The project created a lot of opportunities for potential future projects:

- The biggest challenge is already shortly mentioned in the previous chapter. It is an opportunity to investigate the effect of the different control parameters on the performance of control system. The trade-off between sampling time, measurement accuracy, system dynamics and power usage, of both temperature and pressure, could lead to very interesting discoveries. An optimal balance between these parameters is essential to make it suitable for missions in miniaturized spacecraft like the Delfi-PQ.
- The current sensing system of this project have to be replaced with a sensor that is able to communicate directly with the MCU. The additional conversion step of the analog-to-digital converter is only useful when the analog output of the current sensor is equal to the input range of the converter. The noise to the conversion of the current to voltage signal should be minimal too. A combination of the INA216 [66] with the ADS1115 [65] or a single implementation with the INA219 [64] with a I2C interface might be suitable to solve the both the accuracy and efficiency problems of the ACS712.
- The power requirements of the solenoid valve exceed the maximum peak power of the micropropulsion system. One could investigate whether this is the only available solenoid valve for this application. It is also interesting to examine the energy storage options that fit within the requirements of a PocketQube. The on-board battery of the satellite might be the easiest solution to the storage problem, but it should be investigated whether it meets all the following requirements. A storage system need to have enough space for at least a single spike. In addition, it might also be challenging to find a device that is capable of providing those amounts of power in a very short period of time. A final requirement of the storage device is its efficiency, the amount of power dissipated by the device should be minimal. A dedicated storage system for solely the solenoid valve could also be a possibility.
- The experiments of the project focused on the performance of the temperature control system and the control circuit of the solenoid valve. The work examined the effect of smaller conversion speeds on the measurement quality of the voltage and current sensor. These results could be used in the trade-off from the first point of this section. Similar steps need to be taken to examine the effect of different conversion times on the performance of the pressure measurements. A setup have to be made with a known pressure value to determine the accuracy and precision of the MS5837 sensor series.

A

Appendix

A.1. Main Code

```
#include <SPI.h>
#include <Wire.h>
#include <ADS1X15.h>
#include <MS5837.h>
#include <PID_v2.h>

ADS1115 ADS(0x48);      // Construct an ads1115
MS5837 ms5837;       // Construct a ms5837

// Initialize the PID controller for the heater chip
double Kp = 0.069381, Ki = 0.023004*0.006, Kd = 0.003058*0.006;
double SetPoint, Input, Output;
PID myPID(&Input,&Output,&SetPoint,Kp,Ki,Kd,DIRECT);

// Declare output pins
const int CS10K = 10; const int CS100K = 9; const int SpikeandHold = 2;

// Declare Global Variables
  // Resistance variables
  float ResistanceZero = 5.45;       // Measured heater chip resistance at T0
  float alfa = 0.0011993;        // Temperature coefficient heater chip
  float TempZero = 30;       // Starting point temperature (T0)

  // Control parameters
  float OutputVoltage;
  float Resistance, CurrentResistance, CurrentResistanceStart;
  float StoragePressure, ChamberPressure, ChamberPressureSetPoint;
  float StorageTemp, ChamberTemp, ChamberTempSetPoint;
  float LastErrorSMC, LastDerivativeErrorSMC, LastErrorPID, LastDerivativeErrorPID;
  unsigned long PreviousTimeSMC, PreviousTimePID;
  int NA; int NB;      // Steps for 10k (NA) and 100k (NB)

  // Assign starting state and initiate check sequence
  int state = 1, check = 1;

void setup() {
  Serial.begin(9600);
  Wire.begin();
```

```
  pinMode(CS10K,OUTPUT);
  pinMode(CS100K,OUTPUT);
  pinMode(SpikeandHold, OUTPUT);
  SPI.begin();

  myPID.SetOutputLimits(0.5, 3.8);
  myPID.SetMode(AUTOMATIC);
  myPID.SetSampleTime(1);

  digitalWrite(SpikeandHold, LOW);      // Ensure that the valve is closed at t = 0

  // Temperature sensor setup ADS1115
  ADS.setGain(1);      // Sets the upper limit to +/- 4.096V (1 bit = 0.125mv)
  ADS.begin();
  ADS.setMode(1);       // Select operational mode: single (1) or continuous (0)
  ADS.setDataRate(7);       // Set data rate sensor: 4=128 SPS (default) to 7=860 SPS
}

void loop() {

//   Temperature Control
  switch (state) {
    // Setup State -> Receive required performance and determine
    // resistance for given temperature
    case 1:

      SerialRead();
      Resistance = alfa*ResistanceZero*(ChamberTempSetPoint-TempZero)+ResistanceZero;

    break;

    // Start-up sequence temperature control, apply power and
    // determine current resistance
    case 2:

      OutputVoltage = 2.5;
      DigitalPotControl(OutputVoltage);
      delay(1000);
      HeaterChipSensorStart();
      state = 3;

    break;

    // Temperature control state + check if set point is changed
    case 3:

      PIDControl(Resistance);

      if (Serial.available() > 0) {
      state = 1;        // Go back to state 1 and read new temperature requirement
      check = 2;        // Prevent that the system goes back to the start-up state (2)
      }
    }


// Pressure Control
```

```
  switch (state){
    // Setup State -> Receive Required Performance
    case 1:

      SerialRead();
      ChamberPressureSetPoint = ChamberTempSetPoint; // Temp due to single SerialRead func

    break;

    // Run sliding mode control algorithm
    case 2:

      SlidingModeControl(ChamberPressureSetPoint);

      if (Serial.available() > 0) {
      state = 1;        // Go back to state 1 and read new pressure requirement
      }

    break;
  }
```

A.2. Start-up Sequence Temperature Measurements

```
int HeaterChipSensorStart() {
  // Input Local Variables
  float SumCurrent = 0;
  float SumVoltage = 0;
  float HeaterChipCurrent;
  float HeaterChipVoltage;
  float CurrentStart;
  float VoltageStart;

  // Read Data from ADS1115 (10x to get average value)
  for  (int i = 1; i < 11; i++){
  HeaterChipCurrent = ADS.readADC_Differential_0_1()*0.0006513-13.07;
  HeaterChipVoltage = ADS.readADC_Differential_2_3()*0.0001248+0.04518;

  SumCurrent = SumCurrent + HeaterChipCurrent;
  SumVoltage = SumVoltage + HeaterChipVoltage;
  CurrentStart = SumCurrent/10;
  VoltageStart = SumVoltage/10;
  delay(10);
  }
  CurrentResistanceStart = VoltageStart/CurrentStart;

  return;
}
```

A.3. Temperature PID Controller

```
int PIDControl(float Resistance){
  HeaterChipSensor();       // Run heater chip sensor function
  Input = ChamberTemp;
  SetPoint = ChamberTempSetPoint;

  myPID.Compute();
```

```
  // Determine output voltage using power output PID + current heater chip resistance
  OutputVoltage = sqrt(Output*CurrentResistance);
  DigitalPotControl(OutputVoltage);     // Run digital potentiometers control function
}
```

A.4. Temperature Measurements

```
int HeaterChipSensor() {
  // Input Local Variables
  float w = 0.2;        // Weight factor exponential filter
  float R;

  // Read Data from ADS1115
  HeaterChipCurrent = ADS.readADC_Differential_0_1()*0.0006513-13.07;
  HeaterChipVoltage = ADS.readADC_Differential_2_3()*0.0001248+0.04518;
  R = HeaterChipVoltage/HeaterChipCurrent;

  // Apply exponential filter to measurement results
  // (first start value from starting sequence)
  CurrentResistance = w*R + (1-w)*CurrentResistanceStart;
  CurrentResistanceStart = CurrentResistance;

  ChamberTemp = (CurrentResistance-ResistanceZero)/(ResistanceZero*alfa)+TempZero;

  return;

}
```

A.5. Digital Potentiometers Control

```
int DigitalPotControl(float OutputVoltage){
  // Curve fitted coefficients
  float a = 0.4771;
  float b = 3970;
  float c = 1023;

  // Determine input bits for digital potentiometers
  float X = (b-OutputVoltage*c)/(OutputVoltage-a);
  int N = round(X);
  if (N < 0){
    NA = 0;
    NB = 0;
  }
  else if(N > 2804){
    NA = 255;
    NB = 255;
  }
  else if(N > 1500 && N < 2805){ //2599
    NB = 255;
    NA = N-NB*10;
  }
  else{
    NB = 10*floor(N/100);
    NA = N-NB*10;
  }

  // SPI communication with digital potentiometers
```

```
  digitalWrite(CS100K, HIGH);
  digitalWrite(CS10K, LOW);
  SPI.transfer(0);
  SPI.transfer(NA);
  digitalWrite(CS10K, HIGH);
  digitalWrite(CS100K, LOW);
  SPI.transfer(0);
  SPI.transfer(NB);
  digitalWrite(CS100K, HIGH);
}
```

A.6. Sliding Mode Pressure Control

```
int SlidingModeControl(float ChamberPressureSetPoint){
  float CurrentTimeA = micros();         // Start timer
  float ElapsedTime = CurrentTimeA - PreviousTimeSMC; // Determine elapsed time since last SMC run
  float P = 1000;

  // Run inlet pressure function for chamber pressure
  InletPressure();

  // Determine error values
  float ErrorA = ChamberPressure - ChamberPressureSetPoint;
  float DerivativeError = (ErrorA - LastErrorSMC)/(ElapsedTime/100000);
  float SecondDerivativeError = (DerivativeError - LastDerivativeErrorSMC)/(ElapsedTime/100000);

  float OmegaSMC = SecondDerivativeError + 2*P*DerivativeError + P*P*ErrorA;

  // Open solenoid valve for minimum spike time
  if (OmegaSMC <= 0){
    Serial.println("Spike");
    digitalWrite(SpikeandHold, HIGH);
    delayMicroseconds(350);
    digitalWrite(SpikeandHold, LOW);
  }

  LastErrorSMC = ErrorA;
  LastDerivativeErrorSMC = DerivativeError;
  PreviousTimeSMC = CurrentTimeA;
}
```

A.7. Inlet Pressure

```
int InletPressure() {
  // Read Data from MS5837-02BA
  ms5837.init();
  ms5837.setModel(MS5837::MS5837_02BA);
  ms5837.setFluidDensity(997);       // kg/m^3 (freshwater)
  ms5837.read();

  ChamberPressure = ms5837.pressure();       // Inlet Pressure in mbar
  ChamberTemp = ms5837.temperature();      // Inlet Temperature in degrees Celsius

  return ChamberPressure;
}
```

A.8. Tank Pressure

```
int TankPressure(){
  // Read Data from MS5837-07BA
  ms5837.init();
  ms5837.setModel(MS5837::MS5837_07BA);
  ms5837.setFluidDensity(997);       // kg/m^3 (freshwater)
  ms5837.read();

  StoragePressure = ms5837.pressure();       // Storage Pressure in mbar
  StorageTemp = ms5837.temperature();      // Storage Temperature in degrees Celsius

  return StoragePressure;
}
```

A.9. Serial Read Arduino

```
int SerialRead(){
  static byte ndx = 0;
  char endMarker = '\n';
  char rc;
  const byte numChars = 32;
  char receivedChars[numChars]; // an array to store the received data

  while (Serial.available() > 0 && state == 1) {
  rc = Serial.read();

  if (rc != endMarker) {
  receivedChars[ndx] = rc;
  ndx++;
  if (ndx >= numChars) {
  ndx = numChars - 1;
  }
  }

  else {
  receivedChars[ndx] = '\0'; // terminate the string
  ndx = 0;
  state = 2;
  ChamberTempSetPoint = atof(receivedChars);
  }
  }

  // Check if start-up sequence is required
  if (check == 2){
    state = 3;
  }

}
```

Bibliography

[1] N2yo real time satellite tracking, delfi-pq. https://www.n2yo.com/satellite/?s=51074. Accessed: 2022-02-02.

[2] *Programmable DC Power Supplies*. Agilent Technologies, 4 2013.

[3] *Fully Integrated, Hall Effect-Based Linear Current Sensor with 2.1 kVRMS Voltage Isolation and a Low-Resistance Current Conductor*. Allegro MicroSystems, Inc., 2006. Rev.: 7.

[4] *12-Bit Capacitance-to-Digital Converter*. Analog Devices, 05 2008. Rev. A.

[5] *Arduino Uno REV3*. Arduino, 8 2017. Rev.: 3.

[6] Jun ASAKAWA, Hiroyuki KOIZUMI, Keita NISHII, Naoki TAKEDA, Masaya MUROHARA, Ryu FUNASE, and Kimiya KOMURASAKI. Fundamental ground experiment of a water resistojet propulsion system: Aquarius installed on a 6u cubesat: Equuleus. *Transactions of the Japan Society for Aeronautical and Space Sciences, Aerospace Technology Japan*, 16(5):427–431, 2018. ISSN 1884-0485.

[7] *Atmel ATmega640/V-1280/V-1281/V-2560/V-2561/V*. Atmel, 2 2014. Atmel-2549Q-AVR-ATmega640/V-1280/V-1281/V-2560/V-2561/V-Datasheet$_0$2/2014.

[8] *SAM3X / SAM3A Series*. Atmel, 3 2015. Atmel-11057C-ATARM-SAM3X-SAM3A-Datasheet$_2$3 − Mar − 15.

[9] *8-bit AVR Microcontroller with 32K Bytes In-System Programmable Flash*. Atmel Corporation, 1 2015. Rev.: 7810D–AVR–01/15.

[10] *THE ATTITUDE CONTROL VARIANT OF THE ARM PRODUCT LINE*. Aurora Propulsion Technologies, 2020.

[11] Robert L Bayt. Analysis, fabrication and testing of a mems-based micropropulsion system. Technical report, Aerospace Computational Design Laboratory, Dept. of Aeronautics . . . , 1999.

[12] J. Bouwmeester, E. K. A. Gill, S. Speretta, and M. S. Uludag. A new approach on the physical architecture of cubesats pocket qubes. *JBIS - Journal of the British Interplanetary Society*, 71(7):239–249, 2018. URL https://www.scopus.com/inward/record.uri?eid=2-s2.0-85060660799&partnerID=40&md5=c87934e2bba8e1ca697dae1c281120f2.

[13] J Bouwmeester, S Radu, MS Uludag, N Chronas, S Speretta, A Menicucci, and EKA Gill. Utility and constraints of pocketqubes. *CEAS Space Journal*, pages 1–14, 2020. ISSN 1868-2502. doi: 10.1007/s12567-020-00300-0. URL https://doi.org/10.1007/s12567-020-00300-0.

[14] J.W. Cen and J.L. Xu. Performance evaluation and flow visualization of a mems based vaporizing liquid microthruster. *Acta Astronautica*, 67(3):468–482, 2010. ISSN 0094-5765. doi: https://doi.org/10.1016/j.actaastro.2010.04.009. URL https://www.sciencedirect.com/science/article/pii/S0094576510001268.

[15] J.W. Cen and J.L. Xu. Performance evaluation and flow visualization of a mems based vaporizing liquid microthruster. *Acta Astronautica*, 67(3):468–482, 2010. ISSN 0094-5765. doi: https://doi.org/10.1016/j.actaastro.2010.04.009. URL https://www.sciencedirect.com/science/article/pii/S0094576510001268.

[16] A. Cervone, B. Zandbergen, D. C. Guerrieri, M. De Athayde Costa e Silva, I. Krusharev, and H. van Zeijl. Green micro-resistojet research at delft university of technology: new options for cubesat propulsion. *CEAS Space Journal*, 9(1):111–125, 2017. doi: 10.1007/s12567-016-0135-3. URL https://www.scopus.com/inward/record.uri?eid=2-s2.0-85013231735&doi=10.1007%2fs12567-016-0135-3&partnerID=40&md5=8f83eaa5da6be9e3a36967069bae0385https://link.springer.com/content/pdf/10.1007/s12567-016-0135-3.pdf.

[17] *Tuning Rules for PI and PID*. ControlSoft Inc., 2009-2013. URL http://www.controlsoftinc.com/mailing/message87-ds501.pdf.

[18] M. G. De Giorgi and D. Fontanarosa. A novel quasi-one-dimensional model for performance estimation of a vaporizing liquid microthruster. *Aerospace Science and Technology*, 84:1020–1034, 2019. ISSN 1270-9638. doi: 10.1016/j.ast.2018.11.039. URL https://dx.doi.org/10.1016/j.ast.2018.11.039.

[19] *User's manual, FLIR Ax5 series*. FLIR, 8 2016. Rev.: 1.

[20] Donato Fontanarosa, Luca Francioso, Maria Grazia De Giorgi, C De Pascali, Antonio Ficarella, and Maria Rosaria Vetrano. Flow regime characterization of a mems-based vaporizing liquid microthruster. *AC 2020 PROCEEDINGS*, pages 1–10, 2020. URL https://doi.org/10.3390/app11198954.

[21] Donato Fontanarosa, Chiara De Pascali, Maria Grazia De Giorgi, P. Siciliano, Antonio Ficarella, and Luca Francioso. Fabrication and embedded sensors characterization of a micromachined water-propellant vaporizing liquid microthruster. *Applied Thermal Engineering*, 188:116625, 2021. ISSN 1359-4311. doi: https://doi.org/10.1016/j.applthermaleng.2021.116625. URL https://www.sciencedirect.com/science/article/pii/S1359431121000818.

[22] Wiesław Frącz, Grzegorz Janowski, and Grażyna Ryzińska. Selected aspects of manufacturing and strength evaluation of porous composites based on numerical simulations. *Scientific Letters of Rzeszow University of Technology - Mechanics*, page 31–43, 2017. ISSN 0209-2689. doi: 10.7862/rm.2017.03.

[23] Samuele Gelmi. Ae4s07 micropropulsion project. Technical report, Delft University of Technology, may 2019.

[24] E.N. Gilbert. Increased information rate by oversampling. *IEEE Transactions on Information Theory*, 39(6): 1973–1976, 1993. doi: 10.1109/18.265506.

[25] D. C. Guerrieri, M. A. C. Silva, A. Cervone, and E. Gill. Selection and characterization of green propellants for micro-resistojets. *Journal of Heat Transfer*, 139(10), 2017. doi: 10.1115/1.4036619. URL https://www.scopus.com/inward/record.uri?eid=2-s2.0-85020707711&doi=10.1115%2f1.4036619&partnerID=40&md5=92af6cf2718c7dd937d0e62926704d8f.

[26] D. C. Guerrieri, M. A. C. Silva, H. Van Zeijl, A. Cervone, and E. Gill. Fabrication and characterization of low pressure micro-resistojets with integrated heater and temperature measurement. *Journal of Micromechanics and Microengineering*, 27(12), 2017. doi: 10.1088/1361-6439/aa90fb. URL https://www.scopus.com/inward/record.uri?eid=2-s2.0-85036466123&doi=10.1088%2f1361-6439%2faa90fb&partnerID=40&md5=73bee96242847c2a33293165cec6658d.

[27] Ramesh T. Haris. P.A. Numerical simulation of superheated steam flow in a micronozzle. *Applied Mechanics and Materials*, 592-594:1677–1681, 2014. doi: 10.4028/www.scientific.net. URL https://dx.doi.org/10.4028/www.scientific.net.

[28] Desmond J Higham and Nicholas J Higham. *MATLAB guide*. SIAM, 2016.

[29] K. Karthikeyan, S.K. Chou, L.E. Khoong, Y.M. Tan, C.W. Lu, and W.M. Yang. Low temperature co-fired ceramic vaporizing liquid microthruster for microspacecraft applications. *Applied Energy*, 97:577–583, 2012. ISSN 0306-2619. doi: https://doi.org/10.1016/j.apenergy.2011.11.078. URL https://www.sciencedirect.com/science/article/pii/S0306261911007847. Energy Solutions for a Sustainable World - Proceedings of the Third International Conference on Applied Energy, May 16-18, 2011 - Perugia, Italy.

[30] *System DMM Scanner*. Keithley, 7 1987. Rev.: 4.

[31] Hiroyuki Koizumi, Jun Asakawa, Yuichi Nakagawa, Keita Nishii, Yoshinori Takao, Masakatsu Nakano, and Ryu Funase. Assessment of micropropulsion system unifying water ion thrusters and water resistojet thrusters. *Journal of Spacecraft and Rockets*, 56(5):1400–1408, 2019. doi: 10.2514/1.A34407. URL https://arc.aiaa.org/doi/abs/10.2514/1.A34407.

[32] Pok-Wang Kwan, Xun Huang, and Xin Zhang. Design and testing of a microelectromechanical-system-based high heat flux vaporizing liquid microthruster. *Acta Astronautica*, 170:719–734, 2020. ISSN 00945765. doi: 10.1016/j.actaastro.2020.01.017.

[33] *Electro-Fluidic Systems Handbook, p. 60*. The Lee Company, 2017. Rev.: 9th edition.

[34] *Electro-Fluidic Systems Handbook, p. S36 (285)*. The Lee Company, 2017. Rev.: 9th edition.

[35] B. Liu, X. Li, J. Yang, and G. Gao. Recent advances in mems-based microthrusters. *Micromachines*, 10, 2019. ISSN 2072-666X. doi: 10.3390/mi10120818. URL https://doi.org/10.3390/mi10120818.

[36] Bendong Liu, Xinrui Li, Xu Yang, Jiahui Yang, Yuezong Wang, Desheng Li, and Guohua Gao. A new vaporizing liquid microthruster with planar induction heating. *Sensors and Actuators A: Physical*, 308:112010, 2020. ISSN 0924-4247. doi: https://doi.org/10.1016/j.sna.2020.112010. URL http://www.sciencedirect.com/science/article/pii/S0924424719307009https://www.sciencedirect.com/science/article/abs/pii/S0924424719307009?via%3Dihub.

[37] Bob Marshall. Analog switch frees stuck i (sub 2) c bus. *EDN*, 48(14):108–108, 2003.

[38] D. K. Maurya, S. Das, and S. K. Lahiri. An analytical model of a silicon mems vaporizing liquid microthruster and some experimental studies. *Sensors and Actuators A: Physical*, 122(1):159–166, 2005. ISSN 0924-4247. doi: 10.1016/j.sna.2005.04.020. URL https://dx.doi.org/10.1016/j.sna.2005.04.020.

[39] *MAX31865 RTD-to-Digital Converter*. Maxim Integrated Products, Inc., 10 2012. Rev. 07/2015.

[40] *High-Efficiency Buck-Boost Regulator with 5A Switches*. Maxim Integrated Products, Inc., 6 2017. Rev. 07/2020.

[41] *7/8-Bit Single/Dual SPI Digital POT with Non-Volatile Memory*. Microchip Technology Inc., 8 2007. Rev. B.

[42] *7/8-Bit Single/Dual SPI Digital POT with Non-Volatile Memory*. Microchip Technology Inc., 8 2007. Rev. B.

[43] *High-Efficiency, Single-Inductor, Buck-Boost Converter with 4.2A Switches*. Monolithic Power Systems, Inc., 11 2018. Rev. 1.0.

[44] *High Efficiency Single Inductor Buck-Boost DC-DC Converter Evaluation Board*. Monolithic Power Systems, Inc., 8 2019. Rev. 1.0.

[45] *19A, 600kHz 20V Wide Input Synchronous Boost Converter EV Board*. Monolithic Power Systems, Inc., 9 2019. Rev.: 1.0.

[46] *NI 9211 Datasheet*. National Instruments, 12 2015.

[47] Keita Nishii, Jun Asakawa, Kosei Kikuchi, Mariko Akiyama, Qihang Wang, Masaya Murohara, Yasuho Ataka, Hiroyuki Koizumi, Ryu Funase, and Kimiya Komurasaki. Flight model development and ground demonstration of water resistojet propulsion system for cubesats. *TRANSACTIONS OF THE JAPAN SOCIETY FOR AERONAUTICAL AND SPACE SCIENCES*, 63(4):141–150, 2020. ISSN 0549-3811. doi: 10.2322/tjsass.63.141. URL https://dx.doi.org/10.2322/tjsass.63.141.

[48] V. Pallichadath. Propulsion Subsystem Requirements for the Delfi-PQ Satellites. Technical report, Delft University of Technology, 05 2017.

[49] V. Pallichadath, L. Turmaine, A. Melaika, S. Gelmi, M. V. Ramisa, D. Rijlaarsdam, M. A. C. Silva, D. C. Guerrieri, M. S. Uludag, B. Zandbergen, and A. Cervone. In-orbit micro-propulsion demonstrator for pico-satellite applications. *Acta Astronautica*, 165:414–423, 2019. doi: 10.1016/j.actaastro.2019.09.004. URL https://www.scopus.com/inward/record.uri?eid=2-s2.0-85072989198&doi=10.1016%2fj.actaastro.2019.09.004&partnerID=40&md5=d0d4a3a3d45e0d49362f94f588019fe5https://www.sciencedirect.com/science/article/abs/pii/S0094576519312536?via%3Dihub.

[50] Vidhya Pallichadath, S. Radu, M. A. C. Silva, D. C. Guerrieri, M. S. Uludag, D. Maxence, B. Zandbergen, and A. Cervone. Integration and miniaturization challenges in the design of micro-propulsion systems for picosatellite platforms. URL http://resolver.tudelft.nl/uuid:62945704-eed6-440a-a017-0c62668e0669.

[51] M. A. C. Silva, D. C. Guerrieri, and A. Cervone. State space modeling of fluid flow for thrust control in mems-based micropropulsion. 2016. URL http://resolver.tudelft.nl/uuid:7770bb65-393a-4f84-99a7-ace3f857d68e.

[52] Marsil A. C. Silva, Daduí C. Guerrieri, Henk Van Zeijl, Angelo Cervone, and Eberhard Gill. Vaporizing liquid microthrusters with integrated heaters and temperature measurement. *Sensors and Actuators A: Physical*, 265:261–274, 2017. ISSN 0924-4247. doi: 10.1016/j.sna.2017.07.032. URL https://dx.doi.org/10.1016/j.sna.2017.07.032.

[53] Marsil A. C. Silva, Daduí C. Guerrieri, Angelo Cervone, and Eberhard Gill. A review of mems micropropulsion technologies for cubesats and pocketqubes. *Acta Astronautica*, 143:234–243, 2018. ISSN 0094-5765. doi: 10.1016/j.actaastro.2017.11.049. URL https://dx.doi.org/10.1016/j.actaastro.2017.11.049.

[54] Marsil A. C. Silva, Stefano Silvestrini, Dadui C. Guerrieri, Angelo Cervone, and Eberhard Gill. A comprehensive model for control of vaporizing liquid microthrusters. *IEEE Transactions on Control Systems Technology*, 27 (6):2606–2613, 2019. ISSN 1063-6536. doi: 10.1109/tcst.2018.2865789. URL https://dx.doi.org/10.1109/TCST.2018.2865789.

[55] S. Silvestrini. Closed-loop thrust magnitude control system for nano- and pico-satellite applications. Delft University of Technology. URL http://resolver.tudelft.nl/uuid:a75bf468-2244-46d6-a905-5d52f865ab81.

[56] S Silvestrini, MAC Silva, and A Cervone. Closed-loop thrust control for micropropulsion systems. In *International Astronautical Congress*, 2017. URL http://www.iafastro.org/events/iac/iac-2017/.

[57] Ewelina Sobierska, Rudi Kulenovic, and Rainer Mertz. Heat transfer mechanism and flow pattern during flow boiling of water in a vertical narrow channel—experimental results. *International Journal of Thermal Sciences*, 46(11):1172–1181, 2007. ISSN 1290-0729. doi: https://doi.org/10.1016/j.ijthermalsci.2007.06.011. URL https://www.sciencedirect.com/science/article/pii/S1290072907001470. Nano, Micro and Mini Channels.

[58] *Miniature Altimeter and Diving Module*. TE Connectivity, 08 2017.

[59] *Miniature 30 bar Module*. TE Connectivity, 08 2017.

[60] *Gel-filled, ultra-compact, water resistant digital pressure and temperature sensor*. TE Connectivity, 12 2019. Rev. A8.

[61] *Ultra-small, gel filled dual range pressure sensor, with stainless steel cap*. TE Connectivity, 12 2019. Rev. A.

[62] *Ultra-small, gel-filled, pressure sensor with stainless steel cap*. TE Connectivity, 12 2019. Rev. C2.

[63] *Digital Storage Oscilloscopes*. Tektronix, 10 2009.

[64] *Zerø-Drift, Bidirectional Current/Power Monitor With I2C Interface*. Texas Instruments, 8 2008. Rev.: 2015.

[65] *ADS111x Ultra-Small, Low-Power, I2C-Compatible, 860-SPS, 16-Bit ADCs with Internal Reference, Oscillator, and Programmable Comparator*. Texas Instruments, 5 2009. Rev.: 01/2018.

[66] *Small Size, Low-Power, Unidirectional, CURRENT SHUNT MONITOR*. Texas Instruments, 6 2010. Rev.: 2011.

[67] *SimpleLink™ Mixed-Signal Microcontrollers*. Texas Instruments, 3 2015. Rev. 06/2019.

[68] Cristiano Bigonha Tibiriçá, Douglas Martins Rocha, Ilvandro Luiz Souza Sueth, Gustavo Bochio, Gerson Koiti Kurosawa Shimizu, Marcel Cavallini Barbosa, and Sabrina dos Santos Ferreira. A complete set of simple and optimized correlations for microchannel flow boiling and two-phase flow applications. *Applied Thermal Engineering*, 126:774–795, 2017. ISSN 1359-4311. doi: https://doi.org/10.1016/j.applthermaleng.2017.07.161. URL https://www.sciencedirect.com/science/article/pii/S1359431117323141.

[69] L. A. Turmaine. *A technology demonstration payload for micro-resistojet thrusters on Delfi-PQ*. Thesis, 2018. URL http://resolver.tudelft.nl/uuid:7c3b57e1-f82d-49cc-83dd-de86b7e067fa.

[70] *CEMENT RESISTORS, High Power, Axial Lead*. YAGEO, 8 2021. Rev.: V.0.

[71] Yi Zhang, Guanmin Zhang, Aiqun Zhang, Yinhan Jin, Ruirui Ru, and Maocheng Tian. Frosting phenomenon and frost-free technology of outdoor air heat exchanger for an air-source heat pump system in china: An analysis and review. *Energies*, 11(10):2642, 2018. ISSN 1996-1073. doi: 10.3390/en11102642. URL https://dx.doi.org/10.3390/en11102642.